Ultra-fast dynamics in atoms and molecules during photoionization: from attoseconds to femtoseconds

Månsson, Erik

2014

Ultra-fast dynamics in atoms and molecules during photoionization: from attoseconds to femtoseconds

Doctoral thesis

2014

Erik P. Månsson
Division of Synchrotron Radiation Research
Department of Physics
Lund University

Front cover illustrations:

(top)	Do not look into laser beam with remaining eye!
(waves)	Mono-energetic components of a photoelectron wave packet.
(bottom left)	Dalitz plot for energy correlation between atomic fragments of a carbon dioxide molecule.
(bottom right)	Iso-density surfaces for the three-dimensional momentum distribution of a photoelectron, from helium ionized by high harmonics.

Lund, April 2014

ISBN: 978-91-7473-953-4 (print)
ISB(N+1): 978-91-7473-954-1 (PDF)

Printed in Sweden by Media-Tryck, Lund University

Abstract

Treating the correlated behaviour of multiple particles is challenging for both theory and experiment. This thesis reports on a variety of experimental investigations aiming to advance the understanding of fundamental processes in atoms and molecules: double ionization, isomerization and dissociation. The emphasis lies on ultra-fast processes, where multiple electrons interact or nuclei move so rapidly that coupling between electronic and nuclear dynamics can not be neglected.

Pulses of light from a synchrotron or laser were used to excite or directly ionize molecules or atoms in the gas phase. The momenta (norms or vectors) of the resulting charged fragments were measured in coincidence using different types of time-of-flight spectrometers. Two papers report on the optimization of momentum imaging spectrometers, one for ions and one adaptable electron–ion hybrid.

Direct double ionization was studied in the time domain for the first time, using a pump–probe method with attosecond pulses and electron interferometry (RABBIT). Theoretical development in combination with a coincident measurement of the photoelectron pair from xenon revealed a 500 as group delay, with respect to propagation in a plain Coulomb potential. Electron correlation was also investigated in single ionization, via the angular distribution of a photoelectron. It was shown that the delay of an electron emitted from C_{60} can be altered by 100 as depending on whether the photon energy lies below or above the resonance frequency of a collective electron oscillation (plasmon).

Soft x-rays were used to core-excite molecules to specific orbitals. The subsequent autoionization and dissociation steps were traced by analysing the momentum vectors of multiple ionic fragments. For carbon dioxide, ultra-fast bending initiated by the Renner–Teller effect could bring the two oxygen nuclei together as O_2^+ before dissociation. For few-femtosecond proton migration in water, the kinetic energy release was found to be correlated with the bond angle. Laser-based pump–probe experiments were made on the femtosecond time scale for singly ionized acetylene, $C_2H_2^+$. Isomerization and dissociation dynamics with time scales of 50–500 fs were observed and analysed.

Populärvetenskaplig sammanfattning

Att en elektrisk urladdning ger upphov till ljus syns varje gång blixten slår ner. Den omvända processen, att ljus kan skapa en elektrisk urladdning, upptäcktes av Hertz 1887 som en parentes i utvecklingen av radiomottagare. Undersökningar av detta fenomen visade att elektroner bara kunde frigöras av ljus som hade tillräckligt hög frekvens (ultraviolett). Förklaringen av detta, där ljus betraktas som partiklar (fotoner) och frekvens översätts till energi, bidrog till kvantmekanikens tillkomst. Ökas fotonenergin får den frisläppta elektronen högre fart, vilken kan mätas med så kallade spektrometrar. Senare kom elektronspektroskopi att användas som en metod för att identifiera och studera material. En kombinerad mätning av ljusets frekvens och elektronens fart berättar hur mycket energi som krävdes för att avlägsna elektronen, alltså vilka energinivåer materialet har. Energinivåerna är troligen den viktigaste delen av den kvantmekaniska beskrivningen av material – de bestämmer vilka ämnen som finns och vilka reaktioner som kan ske.

Vad som händer *under* en kemisk reaktion är svårare att mäta, eftersom det i allmänhet går fort och molekylernas tillstånd hela tiden förändras. Under 1980-talet utvecklades metoder för att med korta laserpulser följa förloppet i reaktioner som initieras av ljus. De tidiga experimenten, liksom de som presenteras i denna avhandling, gäller enstaka molekyler i vakuum. Eftersom de då inte påverkas av någon särskild omgivning kan vi lära oss något om grundläggande, universella processer inom en molekyl snarare än hur den interagerar med en viss kombination av omgivande ämnen. I gränsdragningen mellan kemi och fysik kan man säga att detta forskningsfält fokuserar på att fördjupa förståelsen för de allra enklaste kemiska processerna i hopp om att det på sikt kommer till nytta även för att förstå eller designa större system. De typer av processer som studeras i den här avhandlingen är:

- jonisation – då elektroner frigörs från en atom eller molekyl,
- deformation – då molekylen ändrar form genom att atomkärnor flyttar sig och
- dissociation – då en molekyl delas genom att bindningar mellan atomer bryts.

Lasertekniken för att följa förloppet i reaktioner bygger på att en första puls av laserljus ger molekylen ett energitillskott som gör den instabil och sätter atomerna i rörelse. En andra ljuspuls används sedan för att få reda på till exempel vilka atomer som rör sig och hur lång tid det tar innan en bindning är helt bruten. Denna typ av mätning presenteras i slutet av avhandlingen för acetylen, en av de minsta organiska molekylerna med två kolatomer och två väteatomer. En annan metod kan studera samma processer med bara en ljuspuls genom att använda så hög fotonenergi (mjukröntgenljus från en synkrotron) att flera elektroner frigörs och molekylen går i flera positivt laddade bitar. Då kan mätningar av bitarnas massa, fart och riktning tillsammans ge en beskrivning av förloppet – vilka bindningar bryts, i vilken ordning och var hamnar de kvarvarande elektronerna? Den här metoden används för att studera en snabb böjning av koldioxid och vatten i artiklarna **III**–**IV**. I alla tre artiklarna om molekylär deformation händer det att atomer från olika ändar av molekylen närmar sig varandra och utgör ett av fragmenten. Detta kan ses som en prototyp för den typiska kemiska reaktionen, där bindningar både bryts och skapas för att omfördela atomer mellan de ämnen som reagerar.

Alla metoder i den här avhandlingen handlar om att mäta elektriskt laddade partiklar (elektroner och joner), vilka kan styras till detektorer med hjälp av elektriska och magnetiska fält. Artiklarna **V**–**VI** handlar om att designa de elektriska fälten i spektrometrar för att mäta elektroners och/eller joners hastighet med bra upplösning. Experimenten utförs i vakuum för att undvika påverkan från omgivningen, dels i processen som studeras och dels på partiklarnas väg till detektorn.

Samspelet mellan atomkärnor och elektroner är avgörande för alla kemiska reaktioner liksom för processer inom en molekyl. Elektronerna har mindre än en tusendel av atomkärnornas massa och rör sig därför mycket snabbare. Med traditionella lasrar går det inte att göra ljuspulserna kortare än en femtosekund (en biljarddels sekund), vilket är tiden för en svängning hos violett ljus. Det är, som beskrivits ovan, tillräckligt kort för att mäta hur atomkärnorna rör sig i kemiska reaktioner men räcker inte för att få information om elektronernas rörelse. Ännu kortare pulser, där varaktigheten mäts i attosekunder (triljondelar av en sekund), går att skapa som övertoner av ljuset från en tillräckligt ljusstark laser. Förhållandet mellan 100 attosekunder och en sekund är som förhållandet mellan en sekund och 300 miljoner år (tiden sedan reptiler uppstod). Den inblick i vad som händer på elektronernas tidsskala som kan ges av experiment med sådana ljuspulser är alltså väldigt exotisk.

De senaste fem åren har olika metoder som använder attosekundpulser utvecklats för att få inblick i själva jonisationsprocessen och mäta antingen *när* under en laserpuls som en elektron lämnar sin atom eller *hur lång tid* det tar för den att avlägsna sig, vilket beror på den attraktiva kraften mellan atom och elektron. För nästan alla grundämnen blir det elektroner kvar i atomen och det är då inte möjligt att beskriva deras beteende exakt. Det går att göra bra approximationer och beräkningar ändå, vilket används i all simulering av grundläggande kemi, men förståelsen för system med flera elektroner behöver förbättras och nya fenomen upptäcks fortfarande. Processer där atomkärnornas rörelse sker särskilt snabbt eller som kräver samverkan mellan flera elektroner studeras experimentellt i denna avhandling.

Den mest grundläggande fler-elektronprocessen är direkt dubbeljonisation, där absorptionen av *en* foton leder till att *två* elektroner kastas ut ur atomen. I artikel **I** lyckas vi för första gången studera denna process med attosekundpulser. Vi visar att det går att mäta fördröjningar i tiden det tar för elektronparet att lämna atomen (omkring 500 attosekunder). Eftersom sådana fördröjningar beror på samverkan mellan flera elektroner och inte har kunnat mätas förut är det intressant att jämföra dem med förutsägelser från beräkningar, vilket också görs i artikeln. Det finns två olika beskrivningar för hur energi överförs mellan elektronerna i direkt dubbeljonisation, vilka leder till något olika förutsägelser om fördörjningen. Resultatet vi fick ligger ungefär mitt emellan och kan inte utesluta någon av mekanismerna. Med förbättrad precision vore det i princip möjligt att avgöra hur mycket de olika mekanismerna bidrar eller utesluta någon av dem genom den här typen av experiment. Artikel **II** demonstrerar även ett indirekt sätt att studera elektronfördröjning vid fenomen där väldigt många elektroner är inblandade – här i en fotbollsformad molekyl bestående av 60 kolatomer.

Summary of papers

This thesis is based on the following publications and manuscripts, which will be referred to by their Roman numerals.

Paper I:
Double ionization probed on the attosecond time scale

Erik P. Månsson, Diego Guénot, Cord L. Arnold, David Kroon, Susan Kasper, J. Marcus Dahlström, Eva Lindroth, Anatoli S. Kheifets, Anne L'Huillier, Stacey L. Sorensen and Mathieu Gisselbrecht
Nature Physics, **10**, 207–211 (2014) DOI: 10.1038/nphys2880

Access to many–particle dynamics in real time is important for understanding processes induced by electron correlation in atomic, molecular or more complex systems. Direct double ionization constitutes the most fundamental example of such a process. We report the first measurement of electron time-delays in direct double ionization, made possible by combining attosecond light pulses, electron wave packet interferometry and coincident electron detection. An analysis of the electron pair spectrum reveals that non-sequential sidebands are formed for direct one-photon double ionization of xenon. With photon energies around 40 eV, the measurement for the Xe^{2+} $^1D_2$ final state is consistent with a Wigner-like group delay of 500 as.

I participated in the experiment, made software for the detection and analysis, performed the spectral analysis, made the figures and participated in the writing of the manuscript.

Paper II:
Plasmon resonance effect on C_{60} photoelectron angular distribution

T. Barillot, C. Cauchy, P-A. Hervieux, M. Gisselbrecht, S. E. Canton, P. Johnsson, J. Laksman, E. P. Månsson, M. Dahlström, E. Suraud, M. P. Dinh, P. Wopperer, K. Hansen, V. Loriot, C. Bordas, S. Sorensen and F. Lépine
Submitted.

A giant surface plasmon resonance is excited in C_{60} during photoionization at 20 eV photon energy. The effect of the plasmon field on the photoelectron's angular distribution is investigated as function of photon energy via two-dimensional momentum imaging. When the photon energy is scanned across the resonance the angular distribution becomes more isotropic at the resonance. We explain this as a change of up to 100 as in the photoelectron emission time due to acceleration or deceleration by the plasmon's electrical field. Such an effect should be general for all autoionizing surface plasmons and in principle measurable also with attosecond light pulses.

I participated in the experiment and commented on three versions of the manuscript.

Paper III:
Role of the Renner–Teller effect after core hole excitation in the dissociation dynamics of carbon dioxide dication

J. Laksman, E. P. Månsson, C. Grunewald, A. Sankari, M. Gisselbrecht, D. Céolin and S. L. Sorensen

The Journal of Chemical Physics, **136**, 104303 (2012). DOI: 10.1063/1.3692293.

Resonant excitation of CO_2 by 290 eV photons leads to double autoionization, where the Auger lifetime of the initial O 1s or C 1s hole is 3.5–6 fs. To what extent the nuclei in the molecule have moved before the ionization occurs and whether the bonds are broken simultaneously or sequentially is reflected in the 3D momentum distribution of the fragments. We report on the kinetics of several such processes, particularly the change of molecular symmetry from linear to bent before the Auger decay, via the Renner–Teller effect. Electronic and nuclear dynamics occur on similar time scales in this case, which invalidates the Born–Oppenheimer approximation. The signature of this event is an O_2^+ fragment detected in coincidence with C^+ – a complete folding of the molecule from the initial linear (OCO) geometry before dissociation.

I participated in the experiment, made the detection software and participated in the writing of the manuscript.

Paper IV:
Rapid bond rearrangement in core-excited molecular water

Joakim Laksman, Erik P. Månsson, Anna Sankari, Denis Céolin, Mathieu Gisselbrecht and Stacey L. Sorensen

Physical Chemistry Chemical Physics, **15**, 19322 (2013). DOI: 10.1039/c3cp52625a.

This study is similar to Paper **III** except that water is bent already in the ground state. The small mass of hydrogen lets bending and bond rearrangement occur quickly. It also allows up to 60 eV of total kinetic energy for the fragments. We report on the simultaneous breaking of both bonds as well as the alternative bond-rearrangement into H_2^+ in coincidence with O^+. Upon O 1s excitation to either of the lowest unoccupied molecular orbitals the rearrangement is enabled by a symmetric bending vibration and completed well before the molecule rotates appreciably. It does not occur if the photon energy is high enough to directly ionize the molecule.

I participated in the experiment, made the detection software and participated in the writing of the manuscript.

Paper V:
Development and characterization of a multiple-coincidence ion-momentum imaging spectrometer

J. Laksman, D. Céolin, E. P. Månsson, S. L. Sorensen, and M. Gisselbrecht
Review of Scientific Instruments, **84**, 123113 (2013). DOI: 10.1063/1.4853435.

The design of a 3D momentum-imaging spectrometer for ions is presented. The effects of an extended ionization volume are simulated and it is shown that Wiley–McLaren focusing of the time-of-flight is in no conflict with radial focusing of the detector image. The analysis of energy and angle is demonstrated for carbon monoxide. Using core-excited C_{60} and its ^{13}C-isotope distribution, mass resolution beyond 720 u is demonstrated. We also obtain information about life-times and energy release in its autoionization and multi-step fragmentation by evaporation of carbon dimers.

I participated in experiments, made the detection software, made the simulations for Fig. 3 and participated in the writing of the manuscript.

Paper VI:
Multi-purpose momentum imaging spectrometer with three field-regions

Erik P. Månsson, Stacey L. Sorensen, Cord L. Arnold, David Kroon, Diego Guénot, Thomas Fordell, Franck Lépine, Per Johnsson, Anne L'Huillier and Mathieu Gisselbrecht
To be submitted to Review of Scientific Instruments.

The compromises necessary for 3D momentum imaging of electrons and ions in the same spectrometer are investigated analytically and by simulations. By selecting the acceleration or deceleration in a second region and having an adjustable lens curvature, the spectrometer design can be adapted to diverse applications and source properties without breaking the vacuum. Using light in the infrared or extreme ultraviolet and a molecular beam for the sample delivery, we demonstrate three very different applications: 1) mass resolution of Xe^+ isotopes, 2) momenta of N^+ from the dissociation of N_2^+ and 3) electron momenta from acetone or acetylene distinguished by the ion mass in coincidence.

I analysed the spectrometer design analytically and numerically, built it together with M. Gisselbrecht, performed the experiments and wrote most of the manuscript.

Contents

Common abbreviations, symbols and terms

1 as	10^{-18} s, an attosecond
1 fs	10^{-15} s, a femtosecond
1 ps	10^{-12} s, a picosecond
1 ns	10^{-9} s, a nanosecond
cation	Ion with charge +1 (in units of the elementary charge)
dication	ion with charge +2
DI	Double ionization
E_n, E_{I}	Atomic/ionic energy with respect to neutral ground state
ϵ	Kinetic energy
ε_{r}	Relative permittivity
IR	Infrared light
MBES	Magnetic Bottle Electron Spectrometer
RABBIT	Reconstruction of Attosecond Beating By Interference of Two-photon transitions (a method involving photoelectron interferometry)
SI	Single ionization
t	Time, for instance time-of-flight
τ	Time delay in interferometry, for electrons or light
XUV	Extreme ultraviolet light: 10–124 eV, wavelength 10–124 nm
$X \propto Y$	X is proportional to Y
$X \sim Y$	X is of the same order of magnitude as Y
X^*	An excited electronic configuration of the atom or molecule X

Chapter 1

Introduction

Photoionization is a fundamental process but also a powerful tool for understanding the electronic structure of matter and dynamics within atoms and molecules. Hertz' discovery of the photoelectric effect in 1887 and Einstein's explanation using a quantum of light (a photon) in 1905 [1–3] contributed to the development of quantum mechanics and the wave–particle duality [4] that underpins modern physics and chemistry. In the language of this thesis, concerning isolated molecules or atoms in vacuum, the photoelectric effect corresponds to one-photon single ionization. Double ionization by one photon is even more interesting, because it involves multiple interacting bodies and requires quantum mechanical correlation between electrons (or even nuclei) to be explained.

Electronic relaxation has been a key concept, studied in atoms by electron spectroscopy since the discovery of the Auger effect [5–7] to direct double ionization [8, 9]. More recently, few-femtosecond laser pulses have been used to access Auger decay in the time domain [10]. Complex relaxation mechanisms involving the delocalization of electrons between atoms or even molecules (in a cluster or at a surface) are actively being examined using the tunable x-rays from synchrotrons [11–13]. Development of spectrometer technology has allowed the coincident study of a correlated electron pair emitted in double ionization [8, 14, 15]. One-photon double ionization of the helium atom, the most fundamental three-body system, has been studied in great depth [9, 16].

The combination of advanced light sources and spectrometers is utilized in the present work to study dynamics on the quantum-mechanical level in matter. In atoms, we use attosecond pulses and a probing laser pulse to study direct double ionization and delays in the time it takes for the electrons to leave the atom. In molecules, the electronic relaxation itself can be used as an indicator of the time scale for nuclear motion [17, 18]. In that case we excite an inner-shell electron with soft x-rays and in the core-excited state the molecule can deform and dissociate in various ways, with different localizations of charge between the fragments. We use spectrometers that can measure the kinetic energy and angular distribution of multiple ions or electrons coming from one original molecule. The design and optimization of such spectrometers for different applications is another part of the work presented here.

This thesis emphasizes the temporal perspective: What are the time scales for dif-

ferent processes, in what order do they take place and how can we study them? The processes studied here are "ultra-fast", meaning that they occur within a picosecond or faster than molecular rotation, which necessitates specialized tools for the measurements. Chapter 2 covers the basic processes and experimental approaches. Advanced light sources and method details are presented in chapter 3 and the spectrometers in chapter 4. Chapter 5 presents the specific ultra-fast processes that have been studied and describes the results. A concise summary of the papers and my contributions was given on page vii.

Attosecond science

The field of attosecond science, where dynamics in atoms and molecules can be studied on its natural time scale, is just over a decade old. Actually, the necessary laser technology was available earlier [19, 20] but to conclude that attosecond pulses were produced [21] and use this light in applications has required many new methods to be developed [22, 23]. Naturally, the early applications concerned a single electron from an atom [10] – only in recent years has attosecond science in molecules been realized [24].

Since an intense femtosecond laser is used to produce attosecond pules, studies of attosecond dynamics directly within the intense laser pulse were for a long time the dominant approach [25]. This strong-field regime is quite far from the traditional description of stationary states of matter in atomic physics and spectroscopy, but correlation involving the ejected electrons and their re-scattering off the ion could be examined [26, 27]. After my time as doctoral student started in 2009, free-electron lasers at high photon energies have become operational and allowed few-photon double ionization processes to be studied at various intensities [28, 29]. With the attosecond pulses, several pump–probe and interferometry methods were developed around this time and a route to applications concerning electron correlation in atoms was found by measuring delays of the electrons emitted in one-photon single ionization [30–32].

Combining attosecond pulses from 1 kHz laser systems with the coincident detection of multiple particles remains challenging despite a decade of world-wide efforts. A key result in this thesis (Paper **I**) is the interferometry on a two-electron wave packet to determine delays in one-photon direct double ionization. To my knowledge, this is the first application of coincidence methods for attosecond science in the extreme ultraviolet. The current development of laser systems with higher repetition rate is driven much by the wish to access the dynamics of correlated particles. A commentary on the state-of-the art and outlooks for attosecond science was recently given in Ref. [25].

Chapter 2

Light–matter dynamics

2.1 Ultra-fast processes

Photoabsorption and photoionization

Excitation or ionization of matter due to the absorption of light are fundamental processes described by quantum mechanics [33–35]. The absorption of a photon can directly ionize the sample, which is known in solids as the photoelectric effect [1]. The fact that the kinetic energy of the electron, $\epsilon = \hbar\omega - E_\mathrm{I}$ depends on the photon energy $\hbar\omega$ (angular frequency ω and the reduced Planck constant $\hbar$) rather than the flux or intensity[1] of light was discovered by Lenard in 1902 and explained by Einstein in 1905 [2] (reviewed in [3]). In the original context of metallic surfaces the quantity E_I is the work function while for gaseous samples it is the ionization energy. By spectrometry of the photon and the electron, E_I can be deduced and provide information about the sample.

For the interpretation of photoelectron spectra, Koopman's theorem [35], is a good starting point: If all other electrons are unaffected, E_I equals the binding energy of the removed electron. In reality, electron orbitals in an ionic state are slightly different than in the neutral due to multi-electron effects such as correlation and screening. Thus $E_\mathrm{I} = E_\mathrm{final} - E_\mathrm{initial}$ more precisely represents the change in internal energy between the initial atomic and final ionic state. With $E_\mathrm{initial} = 0$ as reference level throughout this work, E_I is simply the energy of the ion. The interaction with light is usually described by a single-particle dipole operator, acting on individual electron coordinates, and correlated electron motion is treated within the initial and final states [33]. While the binding energy concept gives an understanding of the main lines of a photoelectron spectrum with ions in one-hole final states, the ion may undergo an internal relaxation to states which have additional holes, by interaction among its electrons. In *shake-up* an electron in the ion is raised to a normally unoccupied orbital [36], exciting the ion and reducing the observed kinetic energy of the photoelectron to so-called satellite lines in the spectrum. In *shake-off* another electron is set free, resulting in double ionization [37, pp. 1543–1547]. Intuitively,

[1] With high-intensity laser light, multi-photon absorption or even a classical wave treatment can be relevant. A perturbative one- or two-photon treatment is sufficient for the studies reported here.

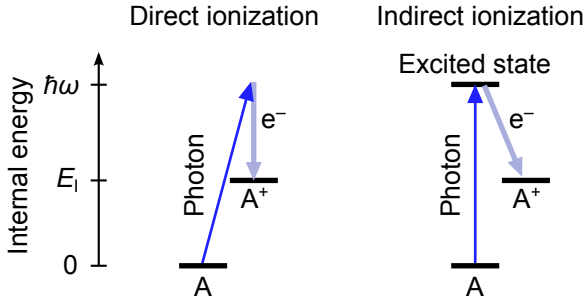

Figure 2.1: **Direct and indirect ionization.** The absorption of a photon (upwards arrow, γ) can either directly ionize the sample ($A + \gamma \rightarrow A^+ + e^-$) or excite the sample to an excited state ($A + \gamma \rightarrow A^*$). The excited state eventually relaxes to a lower internal energy, and emits the excess energy an electron (fluorescence is not studied here). The horizontal lines represent states of the atom/ion, referring to the internal energy axis. For the direct process one follows both the photon and electron (e^-) arrows directly to the ionic state, without a well-defined intermediate state. For the indirect process already the photon arrow leads to a discrete atomic state, which later autoionizes.

these kinds of energy transfer must occur very quickly, on the attosecond time scale, before the photoelectron has left the atom.

Figure 2.1 illustrates that there are both direct and indirect routes to ionization. Direct single ionization is the photoelectric effect, where the dipole operator directly couples the initial state to a final state with one free electron. The upwards arrow in the figure represents the photon energy absorbed, and the length of the downwards arrow represents the kinetic energy of the photoelectron: $\epsilon = \hbar\omega - E_\mathrm{I}$. For indirect ionization the photoabsorption (upwards arrow) instead leads to a highly excited neutral state, above the ionization threshold. It may then decay by autoionization, i.e. a transition to the final state with one free electron and a reduced internal energy of the ion. The operator for autoionization is the Coulomb interaction among the bound electrons, proportional to $\sum_{i<j} 1/r_{i,j}$ where $r_{i,j} = |\vec{r_j} - \vec{r_i}|$ is the difference between coordinates for electrons labelled i and j [33]. In the Auger effect a hole in an inner orbital is filled by the autoionization transition. As shown in the figure, electrons of the same kinetic energy are produced by direct and indirect processes but the indirect contribution will only be observed when the photon energy is resonant with an available state. It may then dominate or interference with the direct path [38]. The excited state before the autoionization may be ionic rather than neutral, if prepared by a previous ionization stage. In this case the result is indirect double ionization. Interaction between photoelectron and secondary electron in the continuum can be neglected if the lifetime of the excited state is several femtoseconds and the photoelectron energy not too low [39].

When absorption of one photon leads to double ionization, directly or indirectly, energy conservation implies

$$\epsilon_1 + \epsilon_2 = \hbar\omega + E_{\text{initial}} - E_{\text{final}} = \hbar\omega - E_{\text{I}} \tag{2.1}$$

where ϵ_1 and ϵ_2 are the kinetic energies of the two electrons set free. $E_{\text{initial}} = 0$ is still the neutral ground state energy while $E_{\text{I}} = E_{\text{final}}$ is generalized to the energy of the final doubly charged ion. Knowing the photon energy and measuring both electron energies provides information about both the excited intermediate state (if indirect) and the doubly charged final state, thus the entire double ionization process of an atom [14]. In molecules, dissociation can lead to substantial kinetic energy of also the ionic fragments which would prevent the identification of E_{I} with static states. To study molecular dynamics the energies of the ions must be measured, ideally both electron and ion momenta in 3D [40–42]. In the present work double ionization has been studied by measuring either the electrons or the ions, but Paper **VI** also demonstrates coincident electron–ion analysis with a newly constructed spectrometer.

Nuclear dynamics in molecules

In addition to the electronic state, a molecule has nuclei that contribute to the total energy and to the complexity of the system. An exact molecular wavefunction, $\Psi(\vec{R}_1, \vec{R}_2, \ldots, \vec{r}_1, \vec{r}_2, \ldots, t)$, has coordinates for each constituent nucleus ($\vec{R}_i$), electron ($\vec{r}_j$) and the time (t). For any practical calculation, the wavefunction is factorized into $\Psi = \Psi_{\text{n}}\Psi_{\text{e}}$ with Ψ_{n} having the nuclear coordinates and Ψ_{e} the electronic – an approach called the *Born–Oppenheimer* approximation [35]. The internal energy of the molecule is thereby separated into electronic energy (a configuration of molecular orbitals, for a particular nuclear geometry) and vibrational energy (the motion of nuclei). This approximation is justified when the nuclei move much more slowly than electrons: electrons on the attosecond time scale and nuclear vibration on the femtosecond time scale, essentially because atomic masses are a few thousand times as large as the electron mass. As will be discussed later, the nuclei sometimes move quite fast and it is interesting to study processes where electronic and nuclear motion can not be separated.

If the total electronic energy is plotted as function of nuclear coordinates, a potential energy curve or landscape (hypersurface) appears. Figure 2.2 illustrates this with the bond length between O and CO in CO_2. The slope of the curve represents the net Coulomb force acting between the O and CO parts of the molecule. A binding molecular orbital has a minimum in the potential energy, and quantized vibrational states localized within the well (indicated by horizontal lines). The $^5\Sigma^-$ state of the dication (doubly charged ion) is repulsive and dissociates rapidly, while the predissociative $^3\Sigma_{\text{g}}^-$ has vibrational states with some lifetime before dissociation. During dissociation, the initial excess in potential energy is converted to kinetic energy of the fragments as the bond length expands. This is indicated by a dotted total-energy line from one of the vibrational levels in $^3\Sigma_{\text{g}}^-$ to braces for kinetic energy sharing on the right side. Excitation to different curves, or points on curves, can determine what deformation (isomerization, proton migration) or bond breakage the molecule

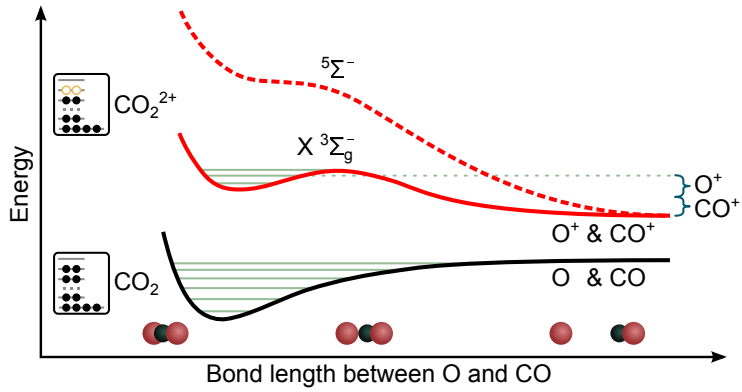

Figure 2.2: **Potential energy curves and their relation to dissociation.** A few potential energy curves for the CO_2 molecule and its dication are sketched [43] (not to scale) along the coordinate where one O–CO bond is extended and eventually broken. The configuration of electronic orbitals, illustrated in the boxes, show that the dication ground state is considered. Nuclear motion adds kinetic energy on top of the potential energy curve and quantized, bound vibrational states are shown as thin lines. The CO_2^{2+} $^3\Sigma_g^-$ state has vibrational levels that are unstable. They may dissociate by internal conversion to a dissociative state or in principle by tunnelling through a barrier along the dotted line. Dissociation releases kinetic energy to the fragments, as indicated by braces on the right side.

is driven towards. In this thesis, processes that lead to ionic fragments are studied by measuring their final momentum vectors. If multiple fragments are charged and dissociation along all coordinates occurs simultaneously, it is called *concerted*.

If bending or dissociation of the molecule only takes a few femtoseconds, the Born–Oppenheimer approximation may not hold and coupling between vibrational and electronic degrees of freedom becomes important [2]. The light mass of a proton compared to other atoms means that proton migration in hydrocarbons (50 fs [45, 46]), and the bending or Coulomb explosion of water are candidates for this. We also study the case where an electronic excitation of carbon dioxide breaks the linear symmetry (the *Renner–Teller effect*, section 5.2.1) and bends the molecule although the Auger lifetime of the excited state is only 6 fs.

[2] Theoretically, the inclusion of nuclear motion in the electron part of the Hamiltonian (and thus in Ψ_e) has recently been discussed as a way to represent the exact wavefunction [44].

2.2 Approaches to retrieve time-information

In quantum mechanics, the outcome of an experiment is described by the eigenvalue of an operator. It is often claimed that there are no time operators in quantum mechanics and the simple question of whether one can measure the arrival time of a particle to a detector is subject to debate [47]. Obviously such measurements are made anyway on the macroscopic level. A resolution put forward by Hilgevoord is to realize that not even the global, spatial coordinates are operators. The distinction between the coordinate system's x-axis and the dynamical variable x_j for the particle labelled j is often forgotten, because the operator for particle position is particularly simple and generic ($\hat{\mathbf{x}}_j = x_j$) [48, 49]. An operator for time measurement is better named a clock operator – describing an observable for a specific system with a known time evolution. An every-day example is the wall clock, where the angle or position measurement of the hour hand is easily related to the time coordinate (modulo half a day). The interferometric technique presented at the end of this chapter is quite similarly based on the cyclic oscillation of intensity and yields time information about an electron, modulo half the laser period. Hilgevoord also argues that non-cyclic clocks are valid in quantum mechanics [48]. After this clarification I still think one can say that temporal information is obtained indirectly: by measuring a clock observable (angle, position, intensity) and knowing how the clock works.

A somewhat different way to relate a measurement of intensity to a time interval is found in spectroscopy of excited states of matter. The uncertainty principle, or more specifically the Lorentzian distribution [33, 50], relates the natural spectral width to the lifetime. The (femtosecond) lifetimes of core-excited states have been studied extensively using this principle in high-resolution x-ray absorption spectroscopy [7]. To determine the mechanisms of the decay requires other techniques – electron spectrometry in the Auger case. In molecules this has enabled the core-hole clock method, where dissociation before or after the Auger decay give spectrally distinct signatures as the photon energy of a synchrotron light source is scanned [7, 17]. Angular information of dissociation products or photoelectrons can provide additional information about the processes and time scales, as will be described in the next section.

The advent of ultra-short laser pulses led to methods working directly in the time domain by scanning the delay between a pump and a probe pulse. Currently, free-electron lasers are bringing femtosecond pump–probe techniques to the x-ray regime [28, 29]. The recent development of attosecond light sources has opened the possibility to probe the even faster dynamics of electrons [25]. In Lund, both synchrotron light from the MAX IV laboratory and word-class attosecond light sources at the Lund Laser Centre are available.

In the following, the two approaches used in this thesis are presented. Studies of the angular information were mainly done with synchrotron-based spectroscopy of core-excited molecules. Attosecond pump–probe studies are reported for electrons from a doubly valence-ionized atom.

2.3 Angular distribution

A formalism for describing the angular distribution of particles emitted in photoionization has been developed particularly by Zare and S. Yang [51, 52] in the dipole approximation. A recent review [53, sec. 2.5] that includes multi-photon processes also points out the earlier and more general work of C. N. Yang [54]. For spherically symmetric samples, such as atoms, the photoelectron angular distribution is given by the amplitude and phase of partial waves. A change in the phase of a wavefunction can also be interpreted as a time delay, and this connection will be established below – unifying the measurement approaches used within this thesis.

2.3.1 Molecular dissociation

A resonant transition in a molecule, i.e. between two states of well-defined symmetry, is most likely to occur if the transition dipole moment is aligned with the polarization vector of the exciting radiation ($\vec{\mathcal{E}}$). Within this thesis, absorption occurs by one linearly polarized photon. Because it has the dipole operator $\vec{\mathcal{E}} \cdot \vec{r} \propto \cos\theta'$, where $\vec{r}$ holds the coordinates of an electron and θ' is an angle from the polarization vector (to the electron, or in a molecule to the transition dipole moment), one-photon ionization cannot give an angular distribution more aligned than $\cos^2\theta'$ [33, 51, 53]. This alignment is essentially a selectivity in the absorption, shown by the blue curves in the polar plots of Fig. 2.3. What we observe in a measurement is the direction in which dissociation fragments (or photoelectrons) are emitted, shown by green filled

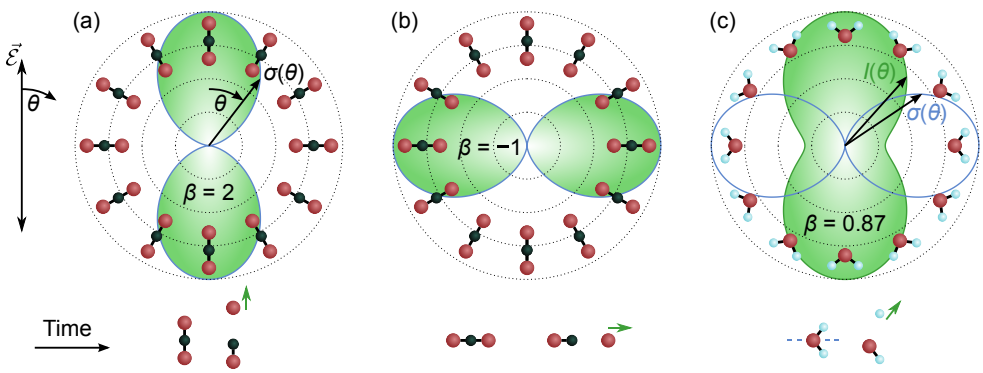

Figure 2.3: **Angular distribution of molecular fragments.** The orientation of a linear CO_2 molecule (a–b) is fully characterized by the angle θ from the polarization $\vec{\mathcal{E}}$, while an angle γ (not shown) around the molecular axis also matters for the bent H_2O molecule (c). The absorption cross section $\sigma(\theta, \gamma)$ mainly selects molecules of a particular orientation, indicated below each polar plot. Rapid dissociation gives the angular distribution $I(\theta)$ which is identical to $\sigma(\theta)$ in case of on-axis dissociation for (a) $\Sigma \to \Sigma$ and (b) $\Sigma \to \Pi$ transitions but (c) rotated and smeared for emission at an angle after a $A_1 \to B_2$ transition.

curves in the figure for various angles, θ, from the polarization vector. Generally, the angular distribution of a fragment is parameterized by the one-photon anisotropy parameter β via the expression $I(\theta) \propto 1 + (3\cos^2\theta - 1)\beta/2$.[1] For an Auger electron, the anisotropy parameter is sometimes factorized into $\beta = \mathcal{A}_{20}\alpha_2$ where $\mathcal{A}_{20}$ represents the alignment of the excited ion (distribution of angular momentum quantum numbers) and α_2 represents the electron emission (interference between partial waves) [33, sec. 3.5][56]. We can analogously discuss two factors that determine the molecular β-parameter [52]: Photoexcitaion introduces anisotropy and dissociation preserves or erodes it. It is fully preserved in a rapid dissociation along the transition dipole moment (the axial recoil approximation [51]) while emission at other bond angles or after rotation erodes the anisotropy towards $\beta \to 0$.

In the case of a linear molecule, maximum alignment is achieved for a parallel transition ($\Sigma \to \Sigma$) where molecules having the axis along the polarization are most likely absorb, shown to yield $\beta = 2$ in Fig. 2.3(a). A perpendicular ($\Sigma \to \Pi$) transition in (b) aligns the molecular axis in the plane perpendicular to the polarization and corresponds to $\beta = -1$. In molecules without linear symmetry, fragments can be emitted at angles neither parallel nor perpendicular to the transition dipole moment (or molecular axis) and give intermediate β-values. In (c) a perpendicular alignment ($A_1 \to B_2$) of the water molecule's symmetry axis is shown. If a proton is emitted in the molecular plane along its bond, at 52° from the symmetry axis, it leads to the displayed (shaded green, $\beta \approx 0.87$) distribution which is nearly parallel to the polarization again[2]. Since the water molecule is not linear, the absorption cross section's dependence on rotation around the molecular axis has also been considered.

Experimentally, the angular distribution will fit the predicted β-value (e.g. Fig. 2.3) if the dissociation occurs promptly, known as the axial recoil approximation. Any rotation or change in the molecular geometry between absorption and fragment ejection will result in an erosion of the alignment. Thus the magnitude of the experimental $|\beta|$ is an indicator of the dissociation time scale [52, 57]. By preparing a short-lived core-excited state (Auger lifetime < 10 fs), with a hole localized to a specific atom, the final charges of the fragment can sometimes inform on which bonds were broken early or late [58]. If momentum vectors of multiple fragments are measured, their correlation (in energy and/or direction) gives more specific information, often visualized in Newton diagrams [59, 60] and Dalitz plots (section 5.2.1).

2.3.2 Scattering phase

While the same general theory for angular distribution applies to ionization of atoms, it is here feasible to analytically relate β to transition matrix elements for the photoelectron [33, 61, 62]. For ionization from a p-subshell, the s ($l = 0$) and d ($l = 2$) partial waves of the photoelectron interfere and their relative magnitudes and phases determine β as function of energy. The reasons for energy-dependence of the phase and the time delay interpretation are found by examining the wavefunction of an

[1] With multiple (parallel) photons, higher-order Legendre polynomials of $\cos\theta$ are used [53, 55].

[2] Emission of the fragment at an angle χ from the transition dipole moment gives $\beta = 3\cos^2\chi - 1$ [52]. The proton bond in water is at $\chi = 90° - 104.45°/2$ for the perpendicular transition.

outgoing photoelectron with azimuthal quantum number l and magnetic quantum number m.

The wavefunction for a photoelectron is theoretically derived using the reverse of a formulation for electron scattering, with both incoming and outgoing waves being part of the solution [33, ch. 7]. To identify a time delay in the propagation away from the atom, only the outgoing wave is considered. Close to the atom, a basis set of spherical waves is necessary (involving l and m) but asymptotically far away, where the kinetic energy is ϵ, the solution has the form of a planar wave. If the momentum vector is measured in an experiment, the plane wave with a specified direction serves as the final state onto which the full wavefunction is projected. Relations between spherical and planar functions and normalization factors can be ignored to concentrate on the phase factor in the final state [63, 64]

$$\Psi_{\vec{k},l}(\vec{r},t) \propto \exp\left(i\Big[\vec{k}\cdot\vec{r} - \frac{\epsilon t}{\hbar} + \frac{Z_{\text{ion}}}{|\vec{k}|a_0}\ln(2\vec{k}\cdot\vec{r}) + \eta_l(\epsilon) - \frac{l\pi}{2}\Big]\right), \tag{2.2}$$

where a_0 is the Bohr radius and $\vec{k} = \vec{p}/\hbar$ is the wave vector, proportional to the electron momentum $\vec{p}$ and giving the kinetic energy $\epsilon = k^2\hbar^2/2m_{\text{e}}$. In the total phase, $\vec{k}\cdot\vec{r} - \epsilon t/\hbar$ gives the trivial phase for the oscillation of the outgoing wave and $l\pi/2$ results from a "centrifugal barrier" dependent on the orbital angular momentum. The term containing the charge, Z_{ion}, of the resulting ion[3] is due to an attractive Coulomb potential (hydrogen-like case) while all non-Coulombic effects due to screening and correlation (still in a central field approximation) are represented by the *scattering phase* $\eta_l(\epsilon)$. Thus η_l is associated with more advanced models for the atomic potential and through the interference of different partial waves (l, m) it affects the observable angular distribution.

In measurements with attosecond pulses of light, the atomic potential and thus the scattering phase can be linked to the propagation time of the photoelectron during its departure from the ion. Figure 2.4 illustrates that as a photoelectron leaves the atomic potential, it gains potential energy and loses kinetic energy. A potential that rises earlier (solid curve) causes a delay with respect to a more slowly rising potential (dashed curve), because of the earlier speed reduction. This classical argument can be applied to the wavefunction by invoking the semiclassical Wentzel–Kramers–Brillouin (WKB) approximation [64, 65] for one spatial dimension, x. The attractive atomic potential, $V(x) < 0$, determines the local kinetic energy, $p_{\text{local}}^2/(2m_{\text{e}}) = \epsilon - V(x)$ where m_{e} is the electron mass. The WKB wavefunction is written

$$\Psi_{\epsilon}^{\text{WKB}}(x,t) \propto \exp\big(i\big[W(x) - \epsilon t\big]/\hbar\big), \quad W(x) = \int_0^x \sqrt{2m_{\text{e}}[\epsilon - V(x')]}\,\mathrm{d}x', \tag{2.3}$$

where $W(x)$ is called Hamilton's characteristic function. The absolute phase of the wavefunction is not meaningful and the purpose here is to find the phase difference, $\eta = (W - W_{\text{Coul}})/\hbar$, between propagation in the atomic potential and a Coulomb potential. In a strict sense, the Coulomb potential is defined for three-dimensional

[3] Only integer charges are used here. Short-range, non-Coulomb effects appear in $\eta_l(\epsilon)$.

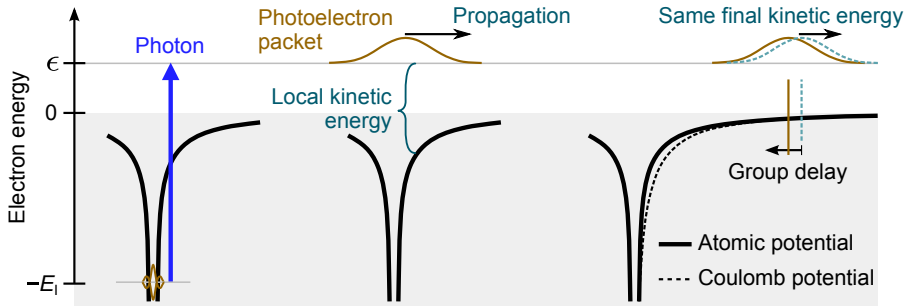

Figure 2.4: **The delay caused by leaving a potential well, in a classical picture.** Snapshots are shown for a photoelectron "packet" of limited duration, emitted by absorbing a short pulse of light. As it propagates away from the ion, its local kinetic energy decreases while the potential energy increases. A potential (solid) that is less attractive than the Coulomb potential (dashed) leads to a group delay. Note that the curve representing the photoelectron packet does not refer to the energy axis.

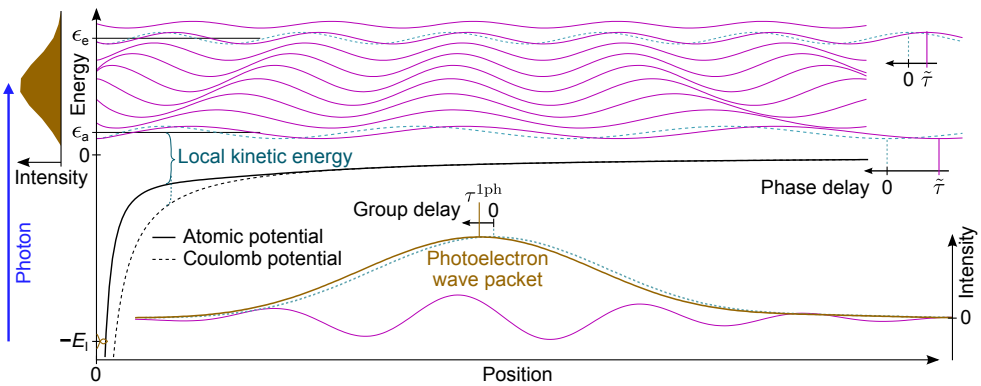

Figure 2.5: **The delay caused by leaving a potential well, for wavefunctions.** The energy width of an ultra-short light pulse leads to a superposition of photoelectron waves at different energies, ϵ, with the spectral intensity indicated to the left. In space (and time) this corresponds to a photoelectron wave packet, shown in the bottom part after some time of propagation (compare Fig. 2.4). The arbitrary potential shown (solid) is less attractive than the reference Coulomb potential (dashed) and the reduced local kinetic energy at short distances leads to a positive group delay of the wave packet. The decomposition into monoenergetic waves is shown in the top part. Note that it is the centre line (e.g. ϵ_a) not the oscillations that refers to the energy axis. For the energies ϵ_a and ϵ_e the negative phase delays, $\tilde{\tau}(\epsilon) = \hbar\eta/\epsilon$, are indicated to the right. The illustrated "atomic" potential is not realistic but was chosen to yield a substantial, positive group delay.

space but $V_{\mathrm{Coul}}(x) = -Z_{\mathrm{ion}}e^2/4\pi\varepsilon_0 x$ can be used in the one-dimensional illustration, with e being the elementary charge and ε_0 the electric constant. Absorption of an ultra-short pulse of light leads to a superposition of photoelectron waves at different energies, as illustrated in the left part of Fig. 2.5. In space and time this corresponds to a photoelectron *wave packet*. The bottom part of the figure shows the wave packet's intensity envelope (dark orange) after some time of propagation away from the nucleus. In close analogy to the group delay of an optical pulse propagating through a dispersive medium [50] one can define a group delay for the photoelectron wave packet. The arbitrary potential shown (solid lines) is less attractive than the reference Coulomb potential (dashed lines) and one may expect the locally reduced kinetic energy to lead to a positive group delay with respect to the Coulomb reference. The decomposition into monoenergetic waves is shown in the top part (magenta curves) and somewhat confusingly the phase delays, $\tilde{\tau}(\epsilon) = \hbar\eta(\epsilon)/\epsilon$, are all negative. The explanation lies in that the high energies are affected less than the low energies by the potential, $\eta(\epsilon) \to 0$ when $\epsilon \to \infty$. The *photoelectron group delay* for one-photon ionization, defined as [63, 64]

$$\tau_I^{\mathrm{1ph}}(\epsilon) = \hbar\frac{\partial\eta}{\partial\epsilon}\,, \tag{2.4}$$

is thus still positive when our atomic potential is less attractive (more repulsive) than the Coulomb potential. The photoelectron group delay is also known as the Wigner-like delay, because Wigner made a similar analysis [66] for a scattered electron, then referenced against free space ($V_{\mathrm{ref}}(x) = 0$) instead of the Coulomb potential[4]. Intuitively, electron interaction can be expected to cause repulsion and positive group delays. However, the reference Coulomb potential for an ion with the charge $Z_{\mathrm{ion}} = Z - B$ already includes the full screening of the $+Z$ charged nucleus by the B electrons that remain bound. Sufficiently close to the nucleus the real potential will be more attractive and both negative and positive group delays τ_I^{1ph} are possible, depending on the detailed interaction and from what subshell the electron is taken.

2.4 Pump–probe methods

An obvious way to study a fast process is to record snapshots at different times. By analogy with photography (see back cover), the result will be blurry if the object moves or changes appreciably while a snapshot is being recorded. A supersonic bullet could be photographed using short (10^{-6} s) flashes of light already around 1889 [67] but nuclei in molecules may vibrate and rearrange appreciably in 10^{-14} s = 10 fs and an electron leaves an atom a few orders of magnitude faster yet. To study light–matter interaction and photochemistry it is then natural to look for the shortest possible pulses of light. A pulse in the electromagnetic field cannot last less than one period, which for visible light is 1.3 (violet) to 2.5 fs (red). This has been called the

[4] Since a scattered electron first approaches and then departs, the original Eisenbud–Wigner–Smith delay is twice as large as an ionization delay [64].

femtosecond barrier [23, 68] and molecular [69, 70] but not electronic dynamics could be recorded in the 20th century.

2.4.1 Femtosecond time scale

In the general pump–probe experiment, a photoreaction is initiated by the pump pulse and after a variable delay the probe pulse makes a "measurement" by transferring the evolving molecule to something that gives a measurable signal. For instance, Fig. 2.6(a) shows a generic AB molecule being excited by the probe to AB* where a reaction starts to take place, here a simple dissociation of an antibonding state. The probing process is in this case photoionization (to AB^+ which is also shown dissociative) and the kinetic energies of electron and/or the ionic fragment could be analysed. More generally, a reaction passing through a bound but short-lived intermediate state X which decays to Y, could be probed either by the remaining population in X or the appearance of population in Y, if they yield distinct observables such as absorption coefficient, kinetic energy or mass per charge. The experiment is performed in a stroboscopic fashion, recording only one snapshot per initiated reaction. Assuming that all sample molecules start from identical state distributions, the measurement accumulates statistics for multiple repetitions at one chosen delay before moving to the next probe delay setting.

Pump–probe studies are usually performed with lasers where short pulses can be produced and the delay accurately controlled. In section 5.2.1 soft x-ray photons from a synchrotron are used to study molecular dynamics. These pulses are much

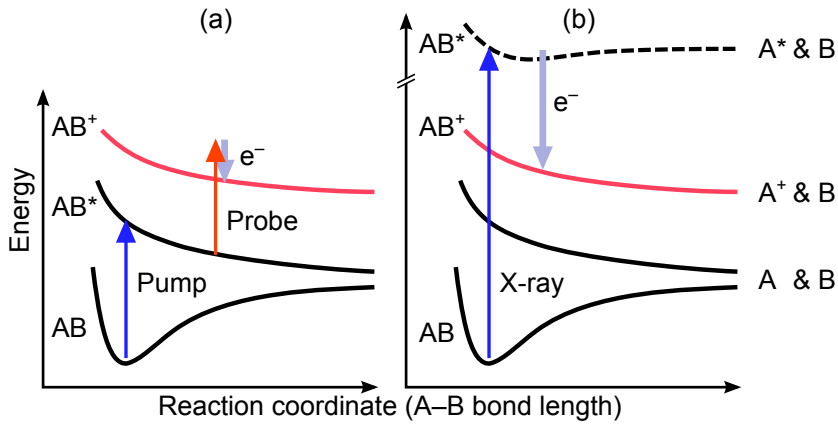

Figure 2.6: **Probing of a photoreaction by photoionization or autoionization.** (a) A pump pulse initiates a reaction, here dissociation of a neutral molecule. A probe pulse photoionizes the sample after an experimentally controlled delay and information about the intermediate state is carried by for instance the kinetic energies of photoelectron and ion. (b) With only one photon (x-ray), the resonant Auger effect can be used to "probe" a core-excited state after a few femtoseconds.

longer than the molecular dynamics but we let a fast Auger decay process in the molecule provide a kind of probe by autoionization, illustrated in Fig. 2.6(b). Sometimes, excited states with different Auger lifetimes can be used as a way to vary the "probe" delay, but the analogy to a pump–probe study should not be stretched too far. An advantage with respect to conventional (bound-electron) lasers is that the synchrotron's monochromatic x-rays can be tuned over a wide range and selectively excite or ionize inner electrons from different atoms in the molecule. The molecule can be put far from equilibrium so that fast, unusual reactions occur and dissociation fragments with a wide range of energies can be analysed. This is the topic of section 5.2.1.

2.4.2 Attosecond time scale

In the attosecond physics community a diverse fauna of pump–probe methods have been demonstrated [22–24]. In many, but not all [71], cases the extreme ultraviolet (XUV) attosecond pulse serves as the pump and an infrared pulse as the probe. Sometimes an isolated attosecond pulse is used [30], in other cases a train of attosecond pulses (of the order of 10 fs long) [21, 31, 32, 72–75]. These techniques make the phase between different partial waves or energies accessible. Recently, group delays in single ionization have been measured [30–32] using the so-called streaking and RABBIT methods. RABBIT will be introduced here and further defined in section 3.3.

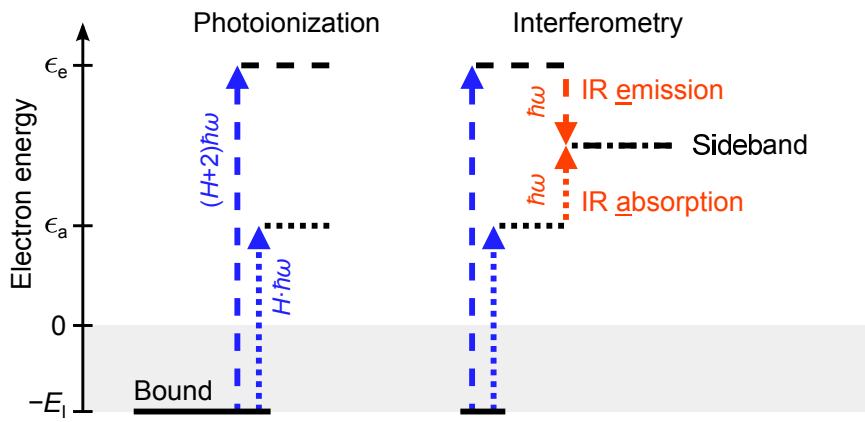

Figure 2.7: **Electron interferometry upon single ionization.**
(left) Ionization by an extreme-ultraviolet photon leads to photoelectrons of the kinetic energy ϵ_a or ϵ_e, depending on whether the absorbed photon energy was $H\hbar\omega$ or $(H+2)\hbar\omega$. These photon energies are harmonics of a fundamental frequency ω in the infrared (IR), with H and $H+2$ being the harmonic orders (odd).
(right) If infrared light is present, the electrons may absorb or be stimulated to emit the IR photon energy, $\hbar\omega$. Fractions of the two different electron wavefunctions (dotted and dashed black) are then transferred to the "sideband" final kinetic energy (dash-dotted) where they interfere.

The RABBIT method relies on interference between two quantum paths to the same final state for the free electron. Figure 2.5 showed that photoionization by an attosecond pulse gives a photoelectron wave packet with a superposition of electrons at different energies. We can consider the two contributions at kinetic energies ϵ_a and ϵ_e separately in the left half of Fig. 2.7. For a suitable choice of energies (which will be explained in section 3.3) the electron fraction at ϵ_a can absorb a probe photon and the fraction at ϵ_e be stimulated to emit a probe photon so that both reach the same final energy. This final energy (dash-dotted), reached by a two-photon process, is known as a *sideband*.

The measured intensity of electrons in the sideband, S, will depend on the phase difference, Δ, between the two interfering terms in the final wavefunction. Δ contains the one-photon scattering phase difference but also properties of the ionizing and probing light. An analysis of the two-photon transition matrix elements (M_a and M_e) leads to the expression [63, 64, 68]

$$S(\tau_\mathrm{IR}) = |M_\mathrm{a} + M_\mathrm{e}|^2 = S_0 + S_\mathrm{osc}\cos(\Delta) = S_0 + S_\mathrm{osc}\cos\big(2\omega(\tau_\mathrm{IR} - \tau_\mathrm{exp})\big) \qquad (2.5)$$

which shows that the intensity oscillates when the delay τ_IR between the pump and probe pulses is scanned. An analogy can be made to the Michelson interferometer [76] where the difference in path length between two arms controls the optical interference. The average intensity S_0 and amplitude S_osc are usually less interesting than the observable sideband delay τ_exp, which contains the photoelectron group delay $\tau_I^{1\mathrm{ph}}$. How the other terms in τ_exp are subtracted will be explained in section 3.3.

Thus while a study of the angular distribution of photoelectrons concerns the intrinsic interference between different partial waves (η influencing β), the RABBIT method uses a probe photon to induce interference between different energies (yielding the energy-derivative of η). Another two-path interferometry method with attosecond pulses has been demonstrated between direct single ionization and sequential ionization via excited intermediate states [77]. In section 5.1.1, RABBIT is applied to direct double ionization to measure the group delay of a two-electron wave packet for the first time.

One could think that to study photoelectron group delays we need an *isolated* attosecond light pulse *shorter* than the time we want to measure, i.e. the time takes the electron to leave the ion. With the interferometric methods, the number of attosecond pulses in a train and the duration of each pulse are actually not limiting the precision as long as the light is spectrally coherent and stable enough between shots. Rather it is the experimental control of the interferometer delay between the attosecond and infrared pulses that needs the same precision as the desired time-measurement.

Chapter 3

Light-source specific methods

The studies reported in this thesis use either a synchrotron light source or high harmonics of laser pulses, forming an attosecond pulse train. Charged fragments from photoionization are detected in both cases (chapter 4) but the properties of the light lead to quite different experimental principles and analysis methods. Some characteristics of the light sources are listed in Table 3.1. Note that if one harmonic is selected from the spectrum its duration (10–20 fs) corresponds to the number of pulses in the train. The individual attosecond pulses (0.1–0.4 fs) are not distinguished in the experiment. When confusion between laser pulse and attosecond pulse must be avoided the expression *laser shot* can be used (generalized to shot in the table). Synchrotron light sources have a tunable monochromator which allows spectroscopic studies where the photon energy is scanned. The spectrally wider comb of high harmonics is often utilized in the time domain, where the pump–probe delay is scanned.

Although the average photon flux is similar for these light sources their time structure gives very different peak photon fluxes. High-power lasers concentrate the intensity of the light and thus the ionization events in few but intense pulses while a

Table 3.1: **Properties of the light sources used.** One energy in the comb of high harmonics is compared to the monochromatized synchrotron radiation. The estimates here apply to harmonics passed through an AlCr filter, which removes lower energies and reduces the flux by almost two orders of magnitude.

		One high harmonic [78]	Synchrotron beamline MAX-lab [79–81]
Photon energy	(eV)	32–42	5–1000
Energy resolution	(eV)	0.3	0.005–0.1
Duration	(s)	10^{-14}	10^{-10}
Number of photons	per shot	10^{7}	10^{4}
Peak photon flux	(photons/s)	10^{21}	10^{14}
Repetition rate	(s^{-1})	10^{3}	10^{8}
Avg. photon flux	(photons/s)	10^{10}	10^{12}
Polarization		linear	linear, elliptic

synchrotron spreads the ionization events more evenly in time. For analysing multiple fragments of a molecule or atom in coincidence (section 4.1) at most one ionization event should occur at a time. This means that a lower gas pressure and longer acquisition time is necessary with lasers. On the other hand, laser set-ups offer an accurate trigger for time-of-flight studies. The spectrometer design in Paper **VI** takes advantage of this by having two sides, allowing the detection of electrons as well as ions. One of the detectors can use the full rate of ionization events when coincident analysis is not required.

3.1 Synchrotron radiation

Synchrotron light sources use relativistic electrons in a storage ring to generate radiation spanning from radio frequencies, via visible light, to hard x-rays. Their high photon flux [82, 83] has since the 1960s revolutionized applications such as x-ray scattering for structure biology [84, 85] and the widely tunable photon energies have enabled x-ray absorption spectroscopy and site-selective excitations for atomic physics and photochemistry [7, 8, 11, 33, 58, 86].

In the present work, the Swedish national laboratory for synchrotron radiation, MAX-lab[1], has been used. It is located in Lund and has three storage rings, of which MAX II with a circumference of 90 m is currently the largest [79, 87].

The principle of a synchrotron light source is outlined in Fig. 3.1. Electrons extracted from a cathode are accelerated and injected into a regular polygon (the storage ring) where magnets at the vertices bend the electron path from one edge to the next. When the relativistic electrons follow a curved path, *synchrotron radiation* is emitted. This is done efficiently by an undulator, which is a repeated structure of alternating magnetic fields with amplitude B_u and period length λ_u. Interference between the undulator periods enhances emission at harmonics[2] of a fundamental angular frequency [82, 83]

$$\omega_1 = \frac{4\pi c_0 \gamma^2}{(1 + K^2/2)\lambda_\mathrm{u}} , \quad K = \frac{eB_\mathrm{u}\lambda_\mathrm{u}}{2\pi m_\mathrm{e} c_0} , \tag{3.1}$$

when observed on-axis. e is the elementary charge and m_e the rest mass of the electron. The γ-parameter is defined by the relativistic electron energy $m_\mathrm{e}\gamma c_0^2$ which is 1.5 GeV in MAX II [87]. That corresponds to an electron speed of $0.99999994c_0$, where c_0 is the speed of light. The fundamental can be tuned for each experiment via B_u in the undulator parameter K, e.g. by an adjustable gap between the magnet poles. The resulting light is sent through a *beamline* with a monochromator that selects a more narrow photon energy (within one harmonic) for the experimental end station.

The time-structure of the light is given by electron bunches of about 100 ps duration and 10 ns separation [80, 81]. The bunches are synchronized to pass through cavities with radio-frequency (RF) electric fields during the half-cycle when the field

[1] "Microtron Accelerator for X-rays" refers to the compact accelerator technique previously used.
[2] Most of the intensity lies in the low-order (1–7) harmonics.

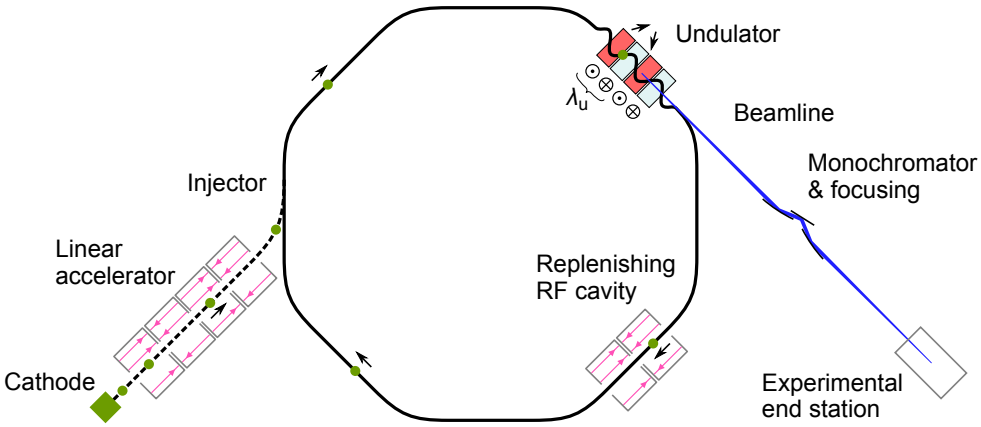

Figure 3.1: **Key components of a synchrotron light source.** Electron bunches (brown dots) circulate the ring and emit light in an undulator.

is accelerating, as illustrated in the hollow boxes of Fig. 3.1. A series of RF-cavities provides the acceleration before injection and a few RF-cavities in the ring replenishes the energy radiated by electrons during each turn. Loss of electrons from the intended trajectory reduces the ring current over time and eventually requires a re-injection (every 12 hours in MAX II).

Studies within this thesis that involve the core-ionization of molecules were made at the soft x-ray beamline I411 of MAX II. It provides horizontally polarised 50 to 1500 eV photons, monochromatized by a grating at grazing incidence angle [88]. For valence ionization, mainly of C_{60} and hydrocarbons, beamline I3 of the 700 MeV MAX III ring [80][3] has been used. It covers the range from 5 eV (ultraviolet) to 50 eV (XUV) with a monochromator at normal incidence angle. A feature of this beamline is that the undulator can be configured to give light with horizontal, elliptical, or vertical polarization [79].

[3] With a circumference of 36 m, MAX III served as a test of compact techniques for the ongoing MAX IV project [80, 89].

3.2 Generation of attosecond pulse trains

The highly non-linear interaction of intense laser light with a gas allows coherent light to be generated in the extreme ultraviolet (XUV) range. The unusually efficient [19] conversion of many low-energy photons to one high-energy photon was understood a few decades ago [20, 21] and opened the field of attosecond science. Without much detail about the laser system this section will explain the basic steps in the generation and application of high harmonics. Wider reviews of attosecond physics are given in references [23] and [22].

All studies involving attosecond pulses or infrared light were performed in the "1 kHz" attosecond physics lab of the Lund Laser Centre [78, 90], prior to its upgrade in 2012. An infrared (0.80 μm) seed laser, with titanium-doped sapphire as medium, delivers an ultra-short pulse with good properties except that its power is not sufficient to generate high harmonics. By stretching this pulse, lowering the instantaneous power further, amplifiers can act on it and increase its power many times. Finally the pulse is temporally compressed while maintaining its energy, which leads to a very high peak power.[1]

When the driving laser light is focused, its electric field is strong enough to overcome the attraction between outer electrons and the nucleus, ionizing an atom of the generating medium (typically a pulsed jet of argon) for a brief moment. The traditional three-step model [20, 78] is used in Fig. 3.2 to describe the response of a single atom to the field:

① Ionization
The atomic potential evolves in the oscillating laser field and exhibits a potential barrier through which valence electrons may tunnel-ionize at certain times. We consider the electron (or a fraction of its probability density) to appear without kinetic energy some distance away from the nucleus, situated on the optically lowered potential energy curve.

② Acceleration
During the next femtosecond, the optical field changes sign. The electron is "lifted" towards higher energy and accelerated back towards the ion.

③ Recombination
When the electron reaches the ion it may return to a bound atomic state by emitting the energy acquired from the driving field. The excess energy takes the form of light again, but now as a single high-energy photon.

The process is repeated in every half-cycle of the optical field (about ten times in a 30 fs driving laser pulse). The periodic emission of high-energy photons means

[1] The average laser power is measurable by a heat sensor to about 3 W (3 mJ per shot at 1 kHz) which is comparable to light bulbs used on bikes. Because the light is pulsed, i.e. mostly "off" but "on" for 30–35 fs, the power during the actual pulse is about 100 GW – equivalent to 40 modern nuclear reactors! The enormous scaling between a light bulb and 40 reactors corresponds to how much shorter than a second already the infrared pulses are.

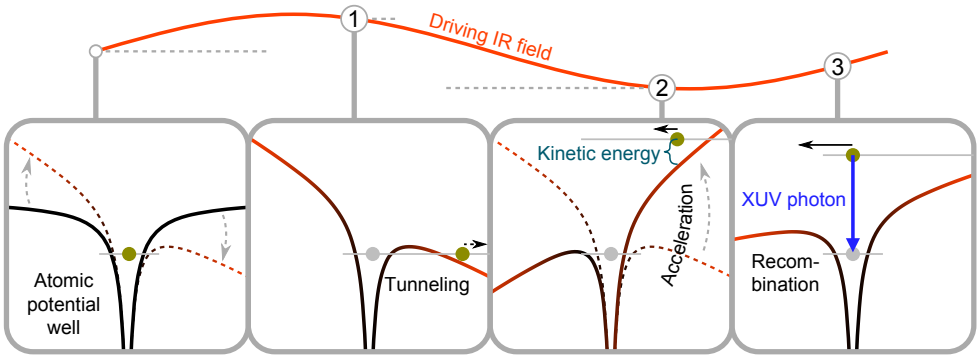

Figure 3.2: **Three-step model for high-order harmonic generation.** The field from a driving laser deforms the atomic potential so that an electron may ① tunnel out of the atom, ② be accelerated back and ③ reach high kinetic energy. Recombining with the atom emits the excess energy as one high-energy photon. In all boxes, solid lines refer to the marked instant while dashed lines give a sense of the evolution.

that the output XUV-field can be described by a Fourier series[2] [50],

$$\mathcal{E}_{\mathrm{XUV}}(t) = \sum_H \mathcal{E}_H \cos\big(H\omega t - \phi(H)\big) = \sum_H \mathcal{E}_H \cos\big(H\omega[t - \tilde{\tau}(H)]\big)\,, \tag{3.2}$$

where ω is the angular frequency of the driving infrared. The XUV component at frequency $H\omega$ is called the harmonic of order H. Components at even H do not appear when the positive and negative half-cycles of the infrared are identical, so the harmonic orders are odd integers. The time structure of the XUV field is determined by the amplitudes $\mathcal{E}_H$ and phases $\phi(H) = H\omega\tilde{\tau}(H)$. Relations between the phases of different harmonics are expressed in the time domain as *phase delay*, *group delay* and *group delay dispersion* (GDD):

$$\text{Phase delay:} \quad \frac{\phi}{\omega_{\mathrm{XUV}}} = \frac{\phi}{H\omega} = \tilde{\tau}(H)\,, \quad H \text{ odd} \tag{3.3}$$

$$\text{Group delay:} \quad \frac{d\phi}{d\omega_{\mathrm{XUV}}} = \frac{1}{\omega}\frac{d\phi}{dH} \approx \tau_{\mathrm{A}}(H) = \frac{\phi(H+1) - \phi(H-1)}{2\omega}\,, \quad H \text{ even} \tag{3.4}$$

$$\text{GDD:} \quad \frac{d^2\phi}{{d\omega_{\mathrm{XUV}}}^2} \approx \frac{1}{\omega}\frac{d\tau_{\mathrm{A}}}{dH} = \frac{\tau_{\mathrm{A}}(H+1) - \tau_{\mathrm{A}}(H-1)}{2\omega}\,, \quad H \text{ odd} \tag{3.5}$$

(These definitions are completely analogous to those for electron wavefunctions in Fig. 2.5.) Their influence on the appearance of an attosecond pulse train is illustrated in Fig. 3.3. As long as all harmonics share a constant group delay, the pulses are as short as possible for the given amplitudes. Attosecond pulses are formed at

[2] For a pulsed driving field this is an approximation. The Fourier *transform* would explain the 0.2–0.3 eV width of the harmonics.

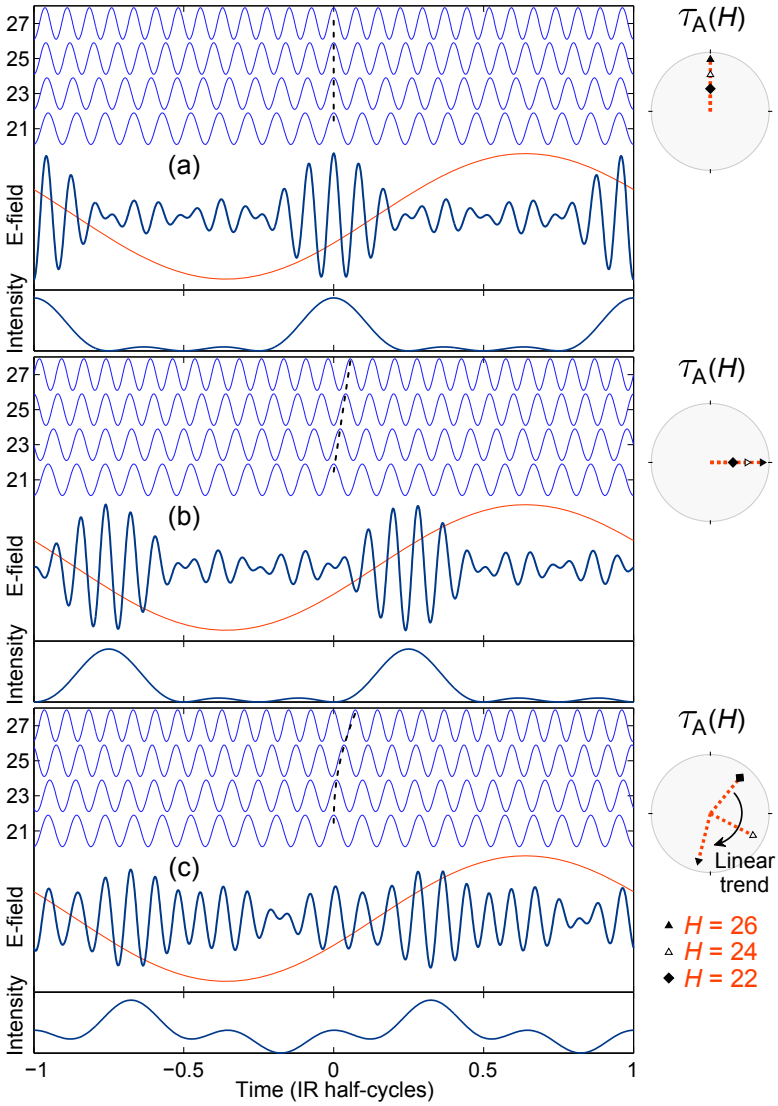

Figure 3.3: **Illustration of the generation of attosecond pulses from harmonics 21 to 27.** Each panel shows electrical fields for the harmonics (vertically shifted), the total field as a thicker dark blue curve and in the bottom part the total intensity. The fundamental infrared (not to scale) is overlaid as a thin red curve at an arbitrary offset. The cases (a)–(c) have different group delays, shown on half-cycle "clocks" to the right and by dashed curves between the harmonic waves. The shortest attosecond pulses in the total field are obtained when the group delay is zero (a) or constant (b), because there are some instants when all harmonics have peaks. Linear chirp (c) gives a varying group delay (GDD = 0.062 fs^2 here) and deteriorates the pulse duration.

instants when all the wave crests meet, while they cancel at other times. Because of harmonic orders being odd, the discrete differential defines group delays $\tau_{\mathrm{A}}(H)$ at the intermediate even H. The clocks on the right side of Fig. 3.3 shows group delays of zero in (a) and $\tau_A(H) = 0.25$ half-cycles $= 0.335$ fs for all H in (c). The constant group delay shifts the attosecond pulse but does not affect its duration (i.e. the width of the intensity envelope in the bottom part of each panel[3]). Dispersion in the group delay between harmonics, as on the clock in (c), smears the pulses to a longer duration. Group delay dispersion is also called *chirp* (of the first order) and higher orders of chirp can be defined by continuing the progression of eq. (3.3)–(3.5).

The spectrum of the generated XUV light is per eq. (3.2) a spectral comb, exemplified in Fig. 3.4. The range of harmonic orders, i.e. the envelope of the spectrum, is affected by the single-atom response, the macroscopic response[4] and filtering. The energy gain from the field in step ② in the single-atom response limits the generated high-harmonic photon energy to [20]

$$\hbar\omega_{\mathrm{XUV}} \leq E_{\mathrm{s}} + 3.17U_{\mathrm{p}} \,, \quad U_{\mathrm{p}} = \frac{e^2}{2\varepsilon_0 c_0 m_{\mathrm{e}}} \frac{I_{\mathrm{IR}}}{\omega^2} \,, \tag{3.6}$$

where $E_{\mathrm{s}} = E_{\mathrm{I}}$ is the ionization energy [91, 92] of the generating gas. The ponderomotive energy, U_{p}, is given by the intensity, I_{IR}, and frequency of the driving field [78]. The elementary charge, e, electric constant, ε_0, speed of light in vacuum, c_0, and electron mass, m_{e}, are all constant[5]. For a given laser intensity, the high-energy cut-off can be controlled by the choice of generating gas. A low-energy cut-off can be achieved by passing the high harmonics through a thin metallic filter. In the present work, the filter always contains aluminium to prevent the driving infrared light from reaching the experimental target chamber (blocking all energies below 20 eV [75, 93]). For Paper **I**, a chromium layer is added to transmit only a narrow window around 40 eV. Even in this window chromium has a low transmittance, about 1/500 of that of aluminium [78, Fig. 2.9].

Although not required for interferometry, I would like to point out the conditions for producing XUV-pulses with durations measured in attoseconds. With an upper cut-off typically between 30 and 100 eV, the period time of the highest harmonic is 140 to 40 as. Pulse durations approaching the period time can be achieved, as illustrated in Fig. 3.3, if the chirp is zero for several high harmonics. Therefore both the intrinsic chirp in the generation and dispersion [50] caused by propagation through the gas must be controlled to produce an attosecond pulse train. For the rays selected by a small aperture ("short trajectories"), the single-atom response gives a positive chirp which can be compensated by a negatively dispersing medium, typically a metal film, less than a millimetre thick. [75, 93] The thickness of and materials in the metallic filter, as well as the generating gas density, can be controlled to tailor the chirp. In 2006, 130 as pulses were produced in Lund [90, 93] and in 2012 a 67 as pulse

[3] With the present choice of phase delays the shape of the total field (carrier–envelope phase) is however changed, from having the central peak positive in (a) to negative in (b).

[4] Phase matching between the propagation of driving infrared and resulting XUV is necessary for the contributions from different atoms to add constructively [78].

[5] This equation applies to vacuum, the intensity in other media should be multiplied by μ_{r}/n.

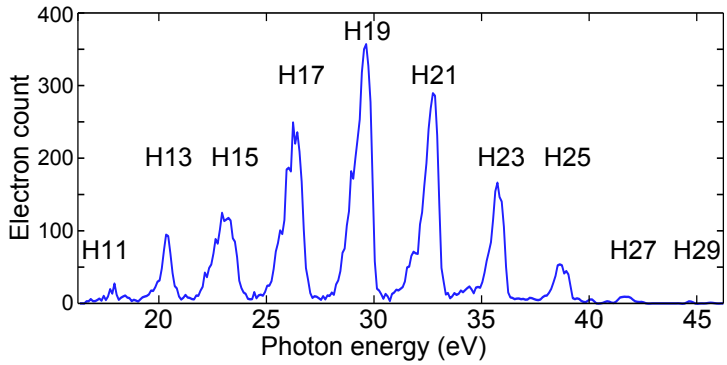

Figure 3.4: **High harmonic orders 11 to 29.** From a photoelectron spectrum of argon, the kinetic energy axis has been converted to photon energy. The harmonics were generated in a different argon jet and filtered through a thin aluminium foil.

was produced in Orlando (a recent review by that group is given in Ref. [94]). The latter example was an isolated attosecond pulse, having a continuous spectrum. The spectrum with discrete harmonics appears for trains of attosecond pulses[6].

3.3 Electron interferometry: the RABBIT method

A well-established technique for photoelectron interferometry is known as RABBIT, for Reconstruction of Attosecond Beating By Interference of Two-photon transitions [21, 74, 75]. Its initial application was to prove the existence of attosecond pulse trains by measuring the chirp (photon group delay derivative) of the high harmonics [21]. More recently it has been used to get information about electron delays instead of photon delays [31, 32].

The principle of the method is to ionize a sample by high harmonics (an attosecond pulse train) in the presence of a probing infrared field. Figure 3.5 shows the experimental set-up, where the laser beam is split into an intense fraction driving the high-harmonic generation and a weak fraction that becomes the probe after an adjustable delay, τ_{IR}.[1]

The interferometric scheme was introduced already in section 2.4.2 and we can now identify the two photoelectron energies as reached in ionization by the harmonics of order H and $H+2$. After absorbing or emitting one infrared photon the two quantum paths interfere in the sideband of order $H+1$ (dash-dotted in Fig. 2.7). The probability, S, to detect an electron in the sideband oscillates when scanning

[6] The semiclassical three-step model allows a continuous range of energies to be gained and emitted. The periodicity can be seen as the cause of discrete harmonics in this model [95].

[1] We define τ_{IR} to increase when the IR-pulse is sent later. Absolute zero is not known with attosecond precision and experiments that only need relative offsets are performed. For weak ionization processes, such as double ionization, statistical noise requires the scan to be made slowly. Drift in the delay-control can be calibrated away using a reference signal in the single ionization spectrum.

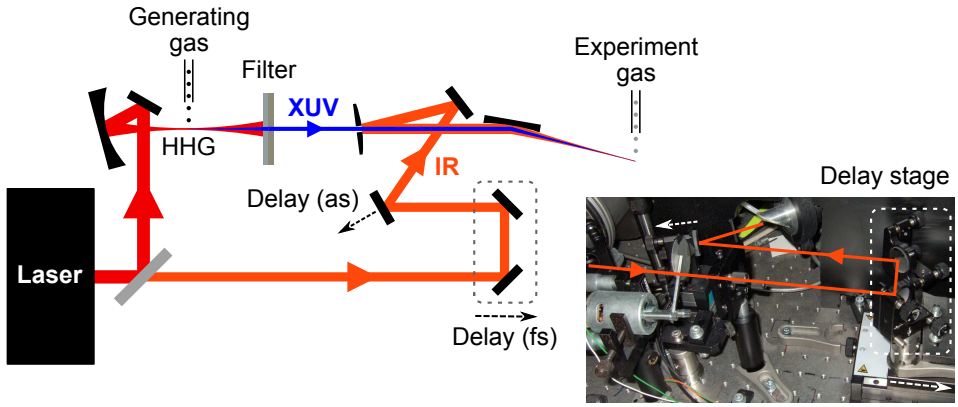

Figure 3.5: **Sketch of the set-up for high-harmonic generation and interferometric experiments.** A beam of laser pulses is split into a high-power arm where XUV high-harmonics are generated (HHG) and an arm with adjustable delay for the weak, IR probe. The coarse (fs) delay is controlled by translating a pair of mirrors and finer (as) delay by a single mirror mounted on a piezoelectric actuator – both shown in the photograph to the right. Finally, the IR and XUV are brought to overlap after a mirror with a central hole and focused on the experimental gas sample.

τ_{IR}, in accordance with [63, 64, 68]

$$S(\tau_{\mathrm{IR}}) = S_0 + S_{\mathrm{osc}} \cos\big(2\omega(\tau_{\mathrm{IR}} - \tau_{\mathrm{exp}})\big) \quad \text{where} \quad \tau_{\mathrm{exp}} = \tau_{\mathrm{A}} + \tau_I^{\mathrm{2ph}}\,. \tag{3.7}$$

The experimentally observable group delay, τ_{exp}, is the sum of the optical group delay τ_{A} for the attosecond pulses and τ_I^{2ph} for the electron wave packet after the two-photon transition (XUV-ionization and IR-probing). In a strict sense, the derivatives that transform phase delay into group delay have been evaluated as discrete differentials between the two harmonics, centred at the sideband's energy. Equation (3.7) assumes that the IR field is weak enough to exclude absorption/emission of two IR-photons [64].

The relative signal, $S_{\mathrm{rel}} = \frac{S}{\langle S\rangle} - 1 \approx \frac{S_{\mathrm{osc}}}{\langle S\rangle} \cos\big(2\omega(\tau_{\mathrm{IR}} - \tau_{\mathrm{exp}})\big)$ will be used in diagrams because it gives comparable units (percentage) regardless of underlying signal and emphasizes the fact that the absolute detection efficiency needs not be calibrated. The equality is exact if the scan equidistantly samples an integer number of cycles, so that the average $\langle S\rangle$ equals the constant term S_0 in (3.7) [96]. This may not be the case after calibrating the time scale and combining different scans, so the parameters are fitted by a numerical least squares procedure.

An example interferogram, or "RABBIT trace", can be seen in Fig. 3.6. Single ionization of argon is chosen because its spin–orbit splitting (0.18 eV [97]) is small enough to be ignored for a simple interpretation of the spectrum: the infrared-induced appearance of sidebands at even harmonic orders is sketched on the left side. The

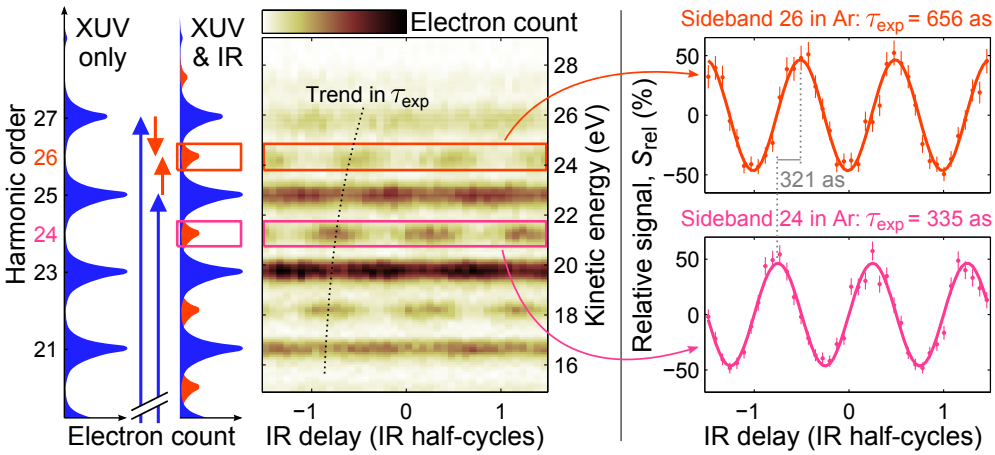

Figure 3.6: **RABBIT trace from single ionization of argon.** (left) Sketched electron spectra without and with the IR field, which makes sidebands appear at even harmonic orders. (middle) Experimental spectra recorded at multiple IR delays are shown using a colour scale. (right) Two sideband signals selected by red and pink boxes from the electron spectra.

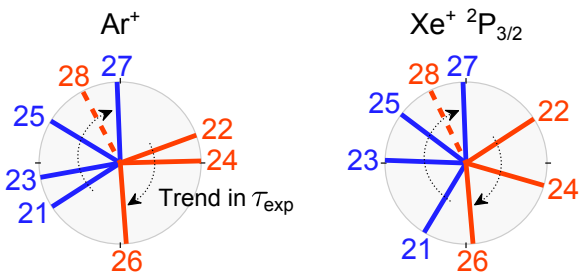

Figure 3.7: **Measured RABBIT delays shown on a clock.** Sidebands are shown in red (even numbers, H) and harmonics in blue (odd H). $\tau_{exp}(H)$ increases clockwise and harmonic 27 was made to point up. One turn is an infrared half-cycle (1341 as). Single ionization of argon (Fig. 3.6) is shown on the left clock and xenon on the right. For xenon only the ionic ground state Xe^+ $5p^5$ $^2P_{3/2}$ is used.

rectangles marked in the two-dimensional central interferogram (colour histogram) show how spectral regions corresponding to specific sideband orders are selected. Their delay-dependent signals $S_{\mathrm{rel}}(\tau_{\mathrm{IR}})$ are shown in separate diagrams on the right-hand side, with clear oscillation of about 50 %. By fitting equation (3.7) to them, the experimental group delay $\tau_{\mathrm{exp}} = \tau_{\mathrm{A}} + \tau_I^{\mathrm{2ph}}$ is determined for each sideband.

To determine the chirp of the attosecond pulse train by RABBIT, which was the original application [21], one can assume $\tau_{\mathrm{exp}} \approx \tau_{\mathrm{A}}$, because the variation in τ_I^{2ph} is comparably small[2] at most energies in Fig. 3.6. If the attosecond pulses had chirp only of the lowest order (constant $d\tau_{\mathrm{A}}/dH$), the dotted curve in the interferogram would be a line. The curvature seen indicates higher-order chirp, possibly caused by the chromium band-pass filter. A good overview of all sidebands and harmonics is given by Fig. 3.7 that shows $\tau_{\mathrm{exp}}(H)$ as hands on a clock. With a revolution time of half the infrared period time the clock naturally conveys the periodicity of interferometric information. The trend of increasing τ_{exp} (positive chirp) is seen between sidebands. Examining the odd harmonics shows that they oscillate with the opposite phase to neighbouring sidebands, because the total number of free electrons is conserved when the IR-interaction takes place in the continuum. The dashed sideband 28 is an exception, presumably due to the lack of harmonic 29. Figure 3.7 also shows the corresponding clock for single ionization of xenon. Both measurements were made with the aluminium+chromium filter but at different dates, meaning that τ_{A} may differ. For the newer RABBIT applications, when the aim is to compare electron delays, a method for subtracting the τ_{A} term is necessary.

To determine electron group delays, we compare different ionization processes brought on by the same pair of harmonics, as recently demonstrated for ionization from different atomic subshells [30–32]. Because the common τ_{A}-terms cancel, the group delay difference $\tau_{I_2}^{\mathrm{2ph}} - \tau_{I_1}^{\mathrm{2ph}} = \tau_{\mathrm{exp},2} - \tau_{\mathrm{exp},1}$ is directly measurable. Although τ_I^{2ph} comes from a two-photon transition, it has been established for single ionization that the delay contribution from the probing infrared, τ_{cc}, is relatively easy to calculate. Subtracting it then yields the one-photon delay [63, 64, 68]:

$$\tau_I^{\mathrm{1ph}} = \tau_I^{\mathrm{2ph}} - \tau_{\mathrm{cc}}\,. \tag{3.8}$$

τ_I^{1ph} is the Wigner-like group delay experienced by the XUV-photoelectron wave packet as it departs from the ion, defined in section 2.3.2 with respect to a Coulomb potential and illustrated in Fig. 2.5. The generalization that allows (3.8) to be used also for direct double ionization is presented in section 5.1.1 and the supplement of Paper **I**.

The "continuum–continuum delay" τ_{cc} would classically correspond to the oscillating infrared field's perturbation of the ionic potential. For kinetic energies well above the infrared photon energy the calculation of τ_{cc} is "universal" in the sense that very little information about the atom or light is necessary, only the effective charge (+1), ω and the kinetic energy. The continuum–continuum delay is negative and tends towards zero for high energies (-30 as $< \tau_{\mathrm{cc}} < 0$ for $\epsilon > 30$ eV [64]). For

[2] More strictly, atomic calculations [32] and the next paragraph can provide values for τ_I^{2ph}.

direct double ionization, two electrons are active and one may partially screen the doubly charged ion core from the other. This can be modelled as an effective charge between 1 and 2 ([9], Paper **I**).

Photoelectron group delays have also be obtained by *streaking* by a strong infrared field [30], which is similar to RABBIT in many ways except for what kind of calculation accounts for the effect of the infrared. In experiments together with the Attosecond Physics group in Lund, the RABBIT method with a weak infrared probe was used, which has the virtue that a perturbative quantum mechanical treatment is possible.

Chapter 4

Spectrometry of charged particles

Most of the atomic or molecular processes investigated in this thesis produce a doubly charged ion or two ions. Detecting two or more photo-reaction products *in coincidence* is essential for the analysis in these cases, as will be described in the first part of this chapter.

Particles that are charged, i.e. electrons and ions, can be accelerated towards a detector. In all but one study, spectrometers that measure the *time of flight* between an ionization region and a detector were used. Depending on the spectrometer type this time gives the kinetic energy and/or mass of the particle. Its three-dimensional (3D) momentum vector can be obtained if the detector also records the impact *position*. The remainder of this chapter describes spectrometry methods and relevant resolution aspects, for one spectrometer based on a magnetic field and a range of spectrometer designs based on electric fields.

The differences in time-structure and photon energy between the laser-based high harmonics and a synchrotron light source (Table 3.1) have motivated the development of two separate electrostatic spectrometers. Because many synchrotron pulses arrive within a typical flight time ($\leq$30 μs), electrons are used as start signal in a dedicated ion spectrometer. The well-separated laser pulses, on the other hand, allow a photon-trigger and a two-sided spectrometer for both electrons and ions.

4.1 Coincident detection of ionization products

Coincident detection of multiple fragments is a powerful technique for understanding photoionization dynamics. The angular correlation between fragments of a molecule may inform on the dissociation time scale (section 2.1). Quantities such as the total kinetic energy released in double ionization (informing on the atomic/molecular states) would be unavailable unless both fragments are detected. While coincidence is very general and can be used for larger systems, e.g. triple and quadruple ionization [98, 99], it imposes some requirements:

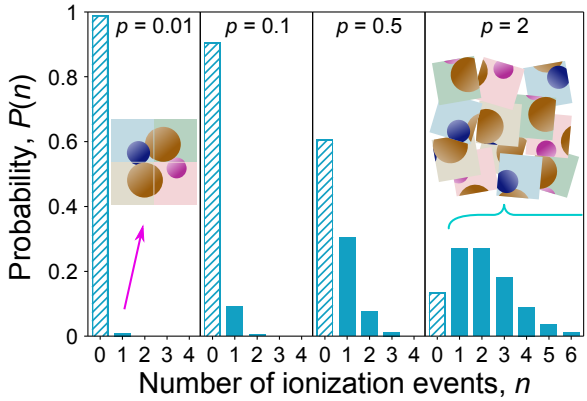

Figure 4.1: **Poisson probability distributions for the number of ionization events, n, per shot.** When on average $p = 2$ events occur per shot (rightmost histogram), ionizing two atoms is as likely as ionizing one. Then false coincidences will dominate – illustrated by too many puzzle pieces. For a low p such as 0.01, ionizing more than one atom is very unlikely and if multiple fragments are detected they can be assumed to come from one original atom – a unique solution to the puzzle. A downside is that most shots of light in this case give no ionization at all ($n = 0$, hatched).

- The light source and sample density should be such that at most one atom/molecule is ionized at a time, otherwise unrelated fragments may be detected together as a *false coincidence*.
- The spectrometer must be able to detect the multiple fragments within one ionization event and store data from different events separately.

These aspects will be developed in the following.

The possibility that one shot from the light source ionizes a particular number, n, of molecules (or atoms) is given by the Poisson distribution [100] $P(n) = p^n \mathrm{e}^{-p}/n!$, illustrated in Fig. 4.1. The parameter p is the average number of ionization events per shot (expectation value $\langle n \rangle$) and should be kept well below unity to ensure that $P(n = 1) \gg P(n > 1)$. With an average of $p = 0.5$ ionization events per shot, the distribution shows a significant probability for ionizing two molecules. As a rule of thumb, $p \leq 0.1$ is necessary to ensure that most coincidences are true, i.e. fragments coming from the same original molecule. As can also be seen in the figure, a low p also means that most shots of light give no ionization event at all. With a synchrotron light source that provides 10^8 shots per second this is not a problem, but the high-power laser systems for attosecond studies are just becoming able to give more than a thousand shots per second. A coincident attosecond experiment thus needs to be run for a longer time to gather enough data. In many cases it is possible to relax the p-constraint and get coincidence-like information by analysing covariances [101–103]. If an experiment has been performed with low p, a covariance analysis does however not bring any new information.

Concerning the ability of spectrometers to separate ionization events from different shots of light, all our time of flight spectrometers are intrinsically suited for this. The very measurement of flight time relies on there being a trigger to signal the start time of a new event, and the recording of a few scalar numbers (flight time and position for 3D momentum) can be performed at a high rate. In the 2D momentum imaging spectrometer, a CCD camera records the image of a phosphorescent screen which is more difficult or to do at kHz or MHz repetition rates with satisfactory resolution and noise levels. The 2D imaging study reported in this work was integrating many shots from the synchrotron into each image.

Among the time of flight spectrometers, which resolve different shots of light, resolving the multiple ionization fragments still imposes some limitations in the coincidence (as well as covariance) capability. We currently use time-to-digital converter (TDC) technology to measure the flight times. The TDC triggers on distinct pulses in the voltage from a pre-amplifier and constant-fraction discriminator[1]. The RoentDek ATR-19 discriminator [104] has a dead-time of 20–25 ns, within which a second particle will not be detected (or cause an average time to be detected). For 3D momentum imaging of ions this is not a major problem, as only ions of the same mass/charge and axial momentum would arrive at the same time. For electrons, however, time differences of this order are expected regardless of momenta and a loss of data would occur. In the study of the electron-pair from double ionization we have therefore used a magnetic bottle electron spectrometer, where electrons are dispersed over a larger time interval and the loss is minimized to electrons with identical energies. A recent technical development is analogue-to-digital converters (ADC) operating with the required precision and repetition rate [105]. Since they record the pulse shape, a superposition of two electronic pulses becomes detectable.

Example: Electron pair spectrometry

In the study of double ionization we record both of the electrons originating from one atom to get information about the two-electron wave packet. The magnetic bottle electron spectrometer will be described in the next section, but the analysis of coincidence data can be described already. The detected double ionization probability was $p_{\mathrm{DI}} = 0.005$. Because low photon energies were filtered away, single ionization from Xe 5p or 5s gives notably higher electron energies than any double ionization and a false coincidence with single ionization ($p_{\mathrm{SI}} = 0.06$) is unlikely within the analysed double ionization spectrum.

Figure 4.2 shows two-dimensional representations of the pair of electrons detected upon double ionization of xenon by high harmonics. The electrons in the pair are denoted fast and slow, with the kinetic energies $\epsilon_{\mathrm{fast}} > \epsilon_{\mathrm{slow}}$. The two-dimensional spectrum in (a) is produced by using one electron energy as coordinate for each axis. Here its contribution to the intensity was included both at $(\epsilon_{\mathrm{fast}}, \epsilon_{\mathrm{slow}})$ and the permuted $(\epsilon_{\mathrm{slow}}, \epsilon_{\mathrm{fast}})$, to show a mirror-symmetric map. The appearance of diagonal stripes in (a) shows that the electrons in a pair are correlated. Information about the

[1] Which in turn receives signals from the micro-channel plate or delay-line detector in the spectrometer.

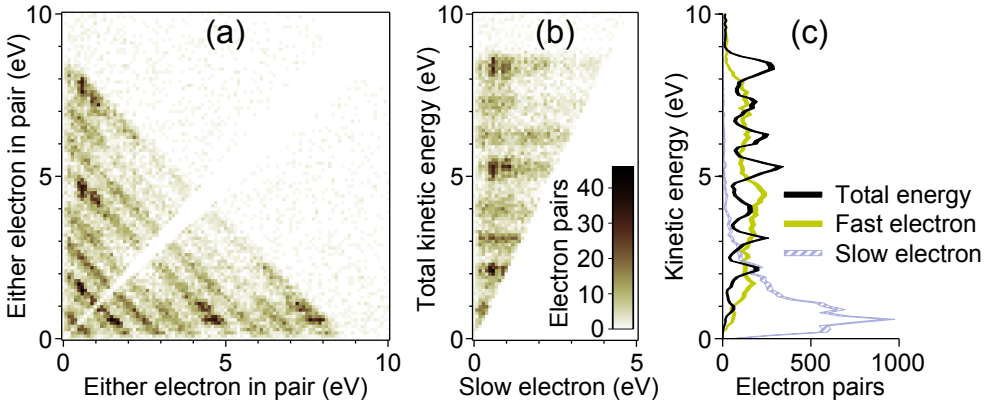

Figure 4.2: **Representations of electron pair spectra.** The electrons in the pair are denoted fast and slow, based on their kinetic energy. (a) Using one electron energy as coordinate for each axis gives this two-dimensional spectrum. (b) Using the sum of both electron energies as the vertical axis, and the slow electron's energy as horizontal axis, a more compact version is obtained. (c) The axis of total energy of the correlated electrons clearly exhibits more structure than the spectrum of either electron on its own. The curve thickness shows ± one Poisson standard deviation.

difference between photon energy and final-state energy is encoded along the diagonal of total kinetic energy, $\epsilon_{\text{fast}} + \epsilon_{\text{slow}}$. Taking this dimension as one axis and ϵ_{slow} as the other axis gives the preferred representation (b). The total energy may also be used on its own (black curve in c) and it clearly exhibits more distinct peaks than the individual electron spectra. If one accounts for the fact that our light contains several harmonic orders, (a) is very similar to the measurement of Eland *et al.* with monochromatic light [14].

False coincidences would appear in Fig. 4.2 (a) as horizontal and vertical stripes, not expressing any correlation[2]. Since the rate of false coincidences is negligible here we only see diagonal stripes which express total-energy conservation. These stripes are horizontal in (b) where the total kinetic energy is used as one axis. The 25 ns detection dead-time causes a white region around the region of identical energies in two-dimensional spectrum, most clearly seen between the mirrored copies in (a).

[2] Representations that treat electrons individually, such as the "all electrons"-spectrum in Fig. 4.5 would not be affected by false coincidences.

4.2 Magnetic bottle electron spectrometer

The magnetic bottle electron spectrometer (MBES) offers coincident detection of electrons, which is essential for studying multiple ionization. Experiments with up to four electrons in coincidence have recently been made at synchrotrons operating in single-bunch mode [98, 99]. In the present work, an MBES has been used to study an electron pair from double ionization of xenon by high harmonics. The well separated laser pulses are favourable for time-of-flight electron spectrometry.

Compared to the 3D momentum imaging spectrometers, the MBES does not preserve angular information. Its one-dimensional energy spectrum is on the other hand better resolved and the angular acceptance is larger than for most other spectrometer types [106, 107]. The long time-of-flight in the MBES minimizes the problem of detector dead-time, particularly for slow electrons.

Principle of the MBES

In the magnetic bottle electron spectrometer (MBES) [108, 109] a magnetic field is applied along the spectrometer axis. The Lorentz force on electrons with a non-axial velocity will alter their direction but not their kinetic energy. Due to a gradient towards a weaker field further from the ionization region, electrons will eventually have an average velocity (in helical trajectories) towards the detector. The field gradient gives the magnetic field lines the so-called "bottle" shape. [108, 110]

After being redirected by the field gradient, electrons move towards the detector through a drift tube of length D_{MBES}. The flight time, t, gives the kinetic energy $\epsilon_{\mathrm{flight}}$:

$$\epsilon_{\mathrm{flight}} = \frac{m_{\mathrm{e}} D_{\mathrm{MBES}}^2}{2t^2}\,, \tag{4.1}$$

where m_{e} is the electron mass.

The MBES of the Lund Laser Centre is shown in Fig. 4.3. An illustration is overlaid to locate the 80 cm long drift tube and the micro-channel plate detector. The light, incident from the left in the figure, is vertically polarized. A photodiode in the laser system triggers the start of the time of flight measurement. Electrons within 2π steradians of sold angle (a hemisphere) are collected by this spectrometer when using only the magnetic field.

To further increase the collection efficiency, particularly for low energies, an additional electric field can be applied across the interaction region. In Paper **I** we apply 2 V, which from the interaction point to the start of the flight tube gives $U_{\mathrm{acc}} = 1$ eV of extra kinetic energy. Approximating the acceleration as instantaneous at the source, the relation between initial kinetic energy ϵ and $\epsilon_{\mathrm{flight}}$ obtained from the time of flight is $\epsilon = \epsilon_{\mathrm{flight}} - U_{\mathrm{acc}}$.

The above description idealized the flight time to be fully independent of the emission angle. In reality different trajectories will have slightly different flight times and the magnetic field parameters are to some extent compromises between optimization for low and high electron energies. The resulting shape of spectral peaks will be analysed in the following.

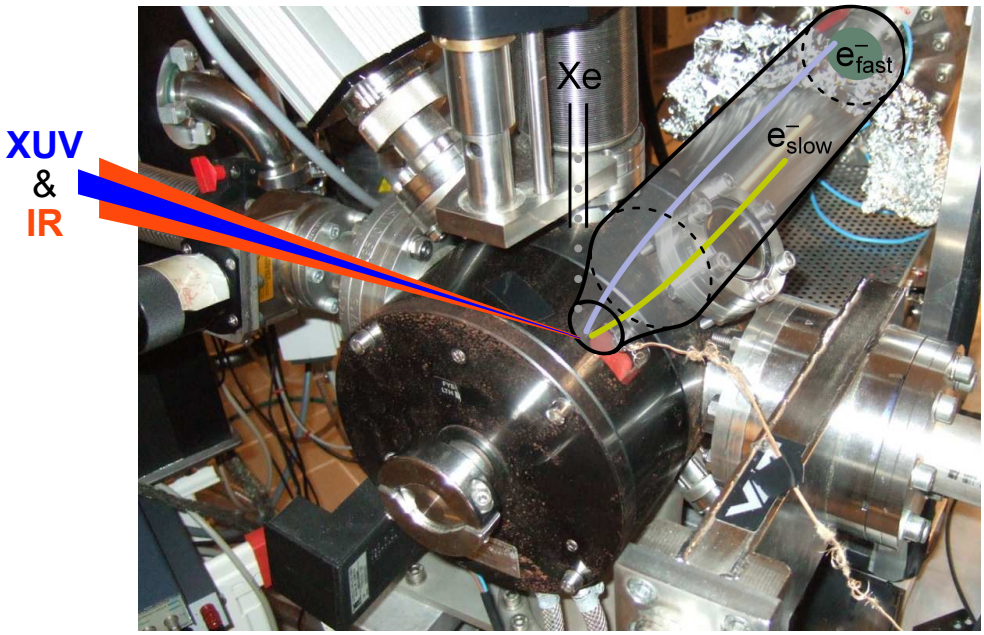

Figure 4.3: **Magnetic bottle electron spectrometer (MBES).** The laser system in Fig. 3.5 provides XUV and IR light from the left, focused where the experiment gas (here Xe) is sprayed into the MBES. Electrons are guided by the magnetic field lines to reach a detector after a time dependent on their initial speed.

Peak profiles

Although the previous section explained the MBES design to make electrons of each energy arrive at a well-defined time, some angular and source position dependence remains [109, 110]. The short laser pulses also produce a broad spectral width of the high harmonics, and short-lived atomic states could contribute further broadening. In total this makes each experimental peak have some width and shape. To find the nominal energy of a spectral peak, and resolve partially overlapping peaks, a model including realistic peak shapes was developed and fitted to the spectra. In the original design report [108] the spectrometer line shape was analysed. For non-zero emission angles with respect to the central axis, the flight time is increased by a perturbation δt_s. The time-of-flight distribution for an ensemble of electrons thus obtains a tail towards longer times. The length of the tail is proportional to the ideal flight time, t_0, while its detailed shape depends on the angular distribution.

In the present work, the case of an isotropic angular distribution in Ref. [108] was considered. The distribution of δt_s was modelled as an exponential decay with probability density $e^{-\delta t_s/(at_0)}$ for positive δt_s and zero probability for negative. The proportionality constant between t_0 and the tail length depends on the MBES settings and is expressed by an asymmetry parameter, a. The value $a = 0.015$ was satisfactory for the entire 0 to 32 eV energy range in Paper **I**. The peak-shape model developed in this work convolves the exponential with a Gaussian that represents all other broadening mechanisms, mainly the width of the harmonics.

An experimental spectrum is displayed in Fig. 4.4(a) as a histogram with 0.1 eV

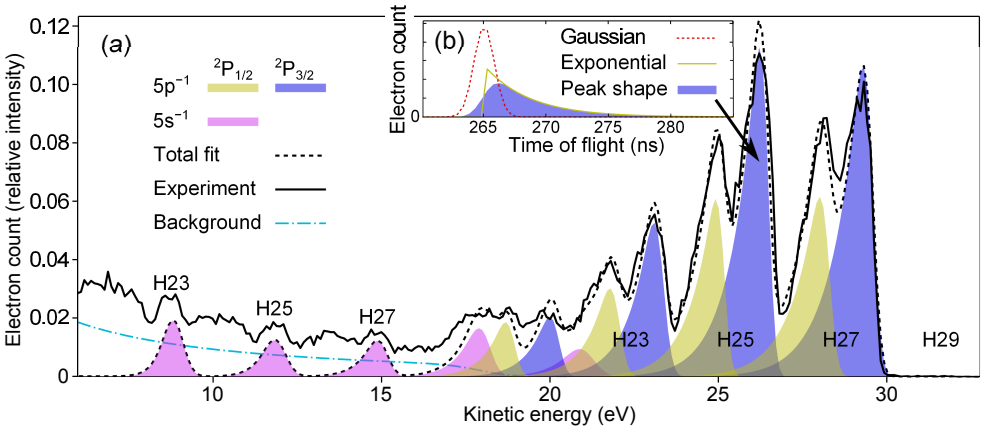

Figure 4.4: **Peak profiles in an MBES electron spectrum.**
(a) Single ionization of Xe by high harmonics. Modelled MBES peak profiles (filled areas) for 5p and 5s ionization have been fitted together with a background term (dash-dotted). (b) The model for harmonic 25 (H25) is isolated and explained in the time-of-flight representation. It is the convolution between a Gaussian for the photon width and an exponential tail for the spectrometer response.

energy bins. The convolution between exponential and Gaussian distributions needs to be performed in the time-of-flight domain and is illustrated by an example for harmonic 25 in the inset (b). The mapping from energy to time, $t(\epsilon)$ is defined by inserting $\epsilon_{\text{flight}} = \epsilon + U_{\text{acc}}$ in eq. (4.1). For instance, the ideal (in absence of asymmetry) peak energy ϵ_0 corresponds to the time of flight $t_0 = t(\epsilon_0)$. The spectral peak shape, $P(\epsilon)$, is then obtained via

$$P(\epsilon) = \left|\tfrac{\mathrm{d}t}{\mathrm{d}\epsilon}\right| P(t(\epsilon)) \,, \quad P(t) \propto \int_0^\infty e^{-x/(at_0)} e^{-((t-x)-t_0)^2/(2\sigma_{\mathrm{g}}^2)} \,\mathrm{d}x \,, \tag{4.2}$$

where the Gaussian standard deviation $\sigma_{\mathrm{g}} = \left|\tfrac{\mathrm{d}t}{\mathrm{d}\epsilon}\right| \delta\epsilon$ is expressed using a width $\delta\epsilon$ in the energy domain. Normalization coefficients have been omitted. A complication arises because eq. (4.1) maps equidistant energy bins to non-equidistant time bins. Instead of evaluating the convolution numerically, a direct expression for $P(t)$ in terms of the complementary error function is used [111], shown as the filled peak shape in (b).

Optimization of parameters for fitting the single ionization spectrum was performed with the Trust-Region-reflective algorithm of Matlab's `lsqnonlin` [112]. The numerical work included a few iterations of fitting peak shapes to the spectrum and improvement of the MBES-calibration by comparison of ideal peak energies to spectral references. When a satisfactory calibration and fit had been found, covering both the single- and double ionization regimes, all parameters except the peak areas were locked and these areas fitted to spectra for individual XUV–IR delays in the interferometric scan. In some dense regions of the spectrum (around 20 eV and for some sidebands) intensity can be redistributed among closely overlapping peaks without changing the total fit much. Such ambiguity, or extra degree of freedom, can be reduced by preferring the statistical $(2J + 1)$ ratio between areas for the $5\mathrm{p}^{-1}$ $^2\mathrm{P}_{3/2}$ and $^2\mathrm{P}_{3/2}$ levels. With peak areas denoted by S, a cost term proportional to $|S_{3/2} - \frac{2}{3}(S_{3/2} + S_{1/2})|$ for each harmonic, was introduced. The proportionality constant was set very low to not influence the fitting in the certain regions but only offer a hint in the ambiguous part.

Double ionization electron-pair spectra were fitted as described in section 5.1.1.

Detection efficiency

To estimate the probability for electrons to be detected in the MBES, a comparison between coincident and non-coincident data can be made. Figure 4.5 contains spectra for all electrons and separate curves for the electrons occurring within a pair. The electrons originating from a double ionization event have at most 10 eV kinetic energy.

In general, it is important to be aware of the possibility of *aborted higher coincidences* when analysing data where multiple degrees of ionization co-exist; in some double ionization events only one of the electrons will be detected. One may note that the "all electrons" and "slow electron in pair" curves share many features and would be similar if the "all electrons" count was multiplied by 0.4. The analogous relation between "all" and the "fast" electron is plausible between 4 and 8 eV. This suggests that the electron detection efficiency is about 40 % ($0.4^2 = 16$ % for a pair).

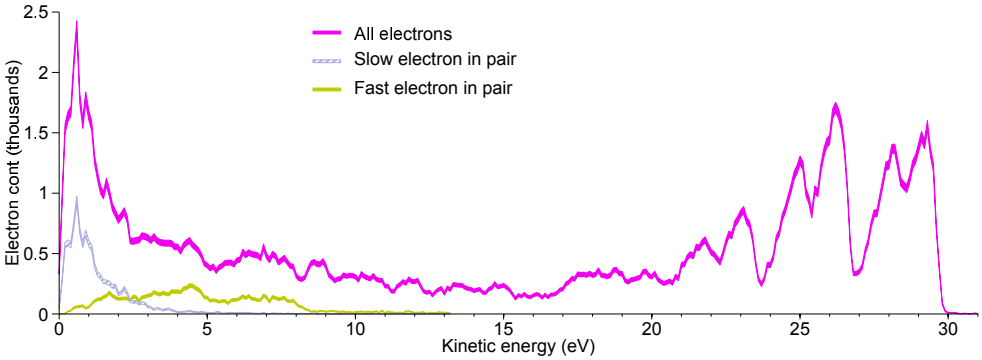

Figure 4.5: **Electron spectrum from xenon ionized by high harmonics.** The spectrum with all electrons (magenta) includes the single ionization data (Fig. 4.4) at high kinetic energies and double ionization (Fig. 4.2) at low energies. The subset of data where *a pair* of electrons came in coincidence gives spectra for the slow (cyan, hatched) and fast (orange) electron. The curve thickness shows ± one Poisson standard deviation.

The overall efficiency depends on both the detector and the angular acceptance. The angular acceptance is expected to be increased for very low-energy electrons because an 1 eV electrostatic acceleration was applied. A detection probability of 65 % was reported for the MBES of Eland *et al.* [14] with 4π angular acceptance. If the detectors behave similarly, this would indicate that our MBES configuration achieved an angular acceptance greater than 2π for low-energy electrons.

4.3 Electrostatic spectrometers

Spectrometers with static electric fields can make the angular information accessible and allows momentum vectors to be imaged in 2D or 3D. For a given kinetic energy, an electrostatic spectrometer gives geometrical trajectories independent of mass, with mass only influencing the time of flight.

Figure 4.6 illustrates a *one*-field spectrometer, extracting particles from a source point towards a detector at a distance of D_{ext} along the z-axis. The time of flight, t, contains information about the mass and, to a variable degree, the initial axial momentum, p_{z}. A very strong extracting field makes p_{z} have a negligible influence on the time, which is the aim for mass spectrometry. A moderate field allows p_{z} to be obtained as a perturbation of the flight time for each mass. In general the ratio, $\kappa = \epsilon/U_{\text{ext}}$, between the kinetic energy ϵ of interest and the extracting work, $U_{\text{ext}} = q\mathcal{E}_{\text{ext}}D_{\text{ext}}$ where q is the particle charge and $\mathcal{E}_{\text{ext}}$ the electric field, can be used to quantify the spectrometer mode. $\kappa \approx 0$ is the strong extraction case and $0 < \kappa < 1$ allows axial momentum resolution. For $\kappa \gtrsim 1$ only particles emitted in some directions will reach the detector.

Better control over the time of flight is possible in spectrometers that, like Fig. 4.7, contain multiple field regions [113, 114]. The extraction region corresponds to Fig. 4.6) and remains the most important for p_{z}-resolution. The additional regions can be seen as "optical elements" with the purpose of enhancing other resolution aspects. The

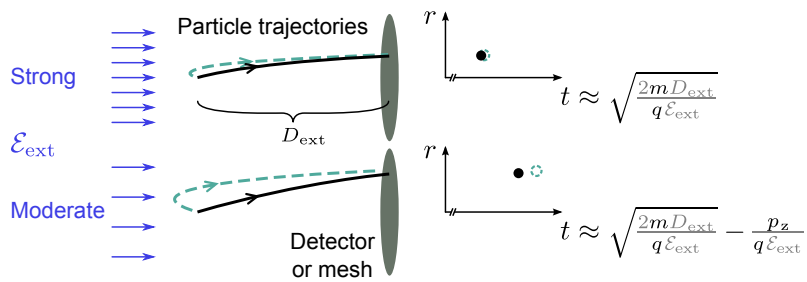

Figure 4.6: **Electrostatic one-field spectrometer.** The time of flight, t, yields information about the particle mass per charge, m/q. Dashed and solid trajectories are drawn for particles emitted in different directions. For a moderate extracting field, $\mathcal{E}_{\text{ext}}$, the axial momentum, p_{z}, can be resolved as an offset in the flight time.

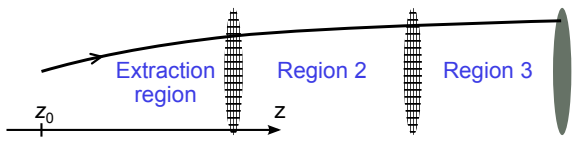

Figure 4.7: **Electrostatic spectrometer with multiple field regions.** Designs with different field regions, separated by metallic meshes, give increased control over the dispersion in time of flight.

simplest optical element is the *drift tube*, a region without electric field. As described in the following, it can improve the mass resolution. The use of an inhomogeneous field as *electrostatic lens* to improve radial momentum resolution will be described thereafter.

3D momentum imaging of ions and electrons will be shown to benefit from different spectrometer geometries and field-strengths. As a result, our two spectrometers have quite different designs. Paper **V** describes 3D focusing in an ion-spectrometer for synchrotron use. For laser-based light, Paper **VI** presents a hybrid design where both electron and ion imaging is possible.

4.3.1 Mass spectrometry

The identification of ion masses is essential for understanding photo-reactions leading to dissociation of molecules [115, 116]. In Fig. 4.6 the acceleration by an electric field was illustrated, with a time of flight proportional to $\sqrt{m/q}$ where m is the ion mass and q its charge, usually +1 e or +2 e. The quantities limiting the ability to resolve different masses are the size of the source volume (where ionization occurs) and the maximum kinetic energy of the ions. In the early work of Wiley and McLaren [113], low-energy ions starting from different positions were considered. They showed that the source size's influence on the time of flight could be eliminated in spectrometers with at least two regions.

The photoionization source volume is determined by the intersection between the beams of light and gas[1]. Both beams are perpendicular to the central z-axis in our spectrometers. It is the distribution of ionic source positions along the z-axis that matters for the time of flight, since the effective extraction distance $D_{\mathrm{ext}}^{\mathrm{eff}} = D_{\mathrm{ext}} - z_0$ is longer for ions starting further away, at a point $z_0 < 0$. The ions that start at negative z_0 also gain more energy from the extracting field (they start at a higher potential energy). At the mesh separating the first and second region, these ions thus arrive later but with a greater speed. If the second region is a drift tube of the right length, $D_{\mathrm{b}} = 2D_{\mathrm{ext}}$, they will catch up with the earlier ions precisely at the detector. This condition for *axial space focusing*, presented by Wiley and McLaren in 1955 [113], makes the flight time independent of z_0 (to the first order). Their article also considers the case of two field regions followed by a drift tube, but the one-field solution seems to be more common for momentum imaging spectrometers [40, 41, 117–120].

If axial focusing is implemented, or the ions have considerable energy ($\kappa = \epsilon/U_{\mathrm{ext}} \gtrsim 10^{-3}$), the kinetic energy, ϵ, will limit the mass resolution. This happens because an ion emitted in the negative z-direction will require a turn-around, potentially increasing its flight time enough to overlap with that of a heavier ion. The turn-around time is determined in the extraction region (compare dashed trajectories in Fig. 4.6) but the temporal separation between masses is influenced also by the other regions. The masses will be more separated in time if less acceleration is applied in the other regions, so typically an extracting field is followed by a long field-free

[1] If the light has a short depth of focus, its intensity variation may further narrow the volume.

drift tube. In this case (with axial focusing or a negligible source size), Paper **VI** shows that the maximum resolvable mass is proportional to $(2 + D_\mathrm{b}/D_\mathrm{ext})\sqrt{U_\mathrm{ext}/\epsilon}$, where U_ext is extraction work and D_b the length of the drift tube. A stronger extraction and longer drift tube are thus to be beneficial for mass resolution of high-energy ions. Our dedicated ion spectrometer has a tube that is $D_\mathrm{b} = 75$ cm long, while only 15 cm was selected for the hybrid electron and ion spectrometer (motivated in the next section). In a shorter tube, a decelerating field can be used to extend the flight times and resolve ions of high kinetic energy. Paper **VI** introduces the concept of *effective drift length* to make it clear how acceleration or deceleration in the other regions influence the time of flight.

In the general two-field spectrometer, axial focusing is not restricted to a fixed length ratio of $D_\mathrm{b}/D_\mathrm{ext} = 2$. With an accelerating work U_b across the second region and the voltage ratio $b = U_\mathrm{b}/U_\mathrm{ext}$ as parameter[2], axial focusing is achieved when $D_\mathrm{b}/D_\mathrm{ext} = 1 + b + \sqrt{1+b}$ (Paper **VI**). For $b = 0$ the drift-tube case with a length ratio of 2 is recovered and a longer tube can be used if it has an accelerating field ($b > 0$). As previously noted, a decelerating field in the second region ($b < 0$) improves separation of high-energy ions. For optimal mass resolution, b should thus be adapted to the source size and kinetic energy range. When studying fragments of molecules, energy is usually the limiting term. The hybrid spectrometer also has a short third region, not to control resolution but to provide a high impact energy for detection efficiency when weak fields are used in the first two regions.

4.3.2 Momentum imaging

The correlation between photo-reaction fragments' kinetic energies and emission angles can be studied if all momentum vectors, $\vec{p}$, are detected in coincidence [40, 60]. For time-of-flight mass spectrometry, the main limitation was the spread due to kinetic energy. 3D momentum imaging spectrometers analyse this spread to determine the p_z-component of the momentum, and have a position sensitive detector to determine the transverse components, p_x and p_y. The hybrid spectrometer is depicted in Fig. 4.8. Particularly the electrode array and a particle trajectory illustration in (b) may provide a useful context for the following description. Methods for improving the resolution will be explained first for the axial and then for the transverse (radial) momentum component.

The relationship between p_z and the flight time is given by the lower equation in Fig. 4.6[3]. The p_z-resolution for ions is limited by the axial size of the source but, as was explained for mass spectrometry, axial focusing can reduce this limitation. Figure 4.9(a) illustrates how ions starting at different z_0 arrive at different times (and thus different radii) to the first mesh but simultaneously to the detector. For electrons, however, the spread of flight times is so short that the time resolution of the detector (0.1–0.5 ns FWHM [104]) often becomes a more important limitation. To

[2] The expression $1 + b$ here corresponds to k_0 in the notation of Wiley and McLaren [113].

[3] Particles with too negative p_z ($\kappa \geq 1$ here) will not be extracted before reaching the repelling mesh. A p_z^2-term in $t(p_\mathrm{z})$, which was not shown, makes the function non-bijective near this limit.

resolve p_z of electrons with energies below a few electronvolts, the temporal separation must be expanded by using a weak extraction field.

Concerning the transverse momentum components, they are conserved throughout the spectrometer if all electric fields are parallel to the z-axis, as assumed in the mass spectrometry section. The detected position is thus $x = x_0 + tp_x/m$ where x_0 is the location of the ionization event (and analogously for y). The transverse source size δx_0 is imaged to $\delta x = \delta x_0$ and results in a momentum resolution of $\delta p_x = m\,\delta x/t$. Figure 4.9(b) shows that an electrostatic lens [121] can be used to focus the particle trajectories radially and improve the resolution. Here, two of the electrode rings (shown as lines at large radii in the cylindrical coordinates) are put at a repelling potential and cause an inhomogeneous field in the second region of the spectrometer. Particles starting closer to the repelling electrode are deflected more towards

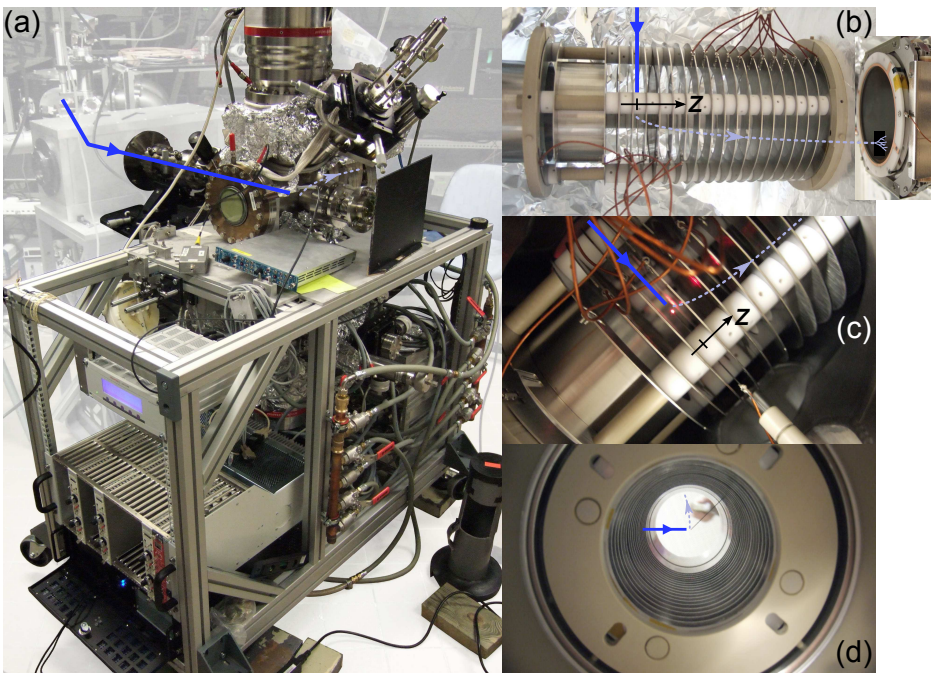

Figure 4.8: **3D momentum spectrometer for electrons or ions.** (a) Overview of the experimental set-up with the incoming beam of light as a dark blue arrow. The background has been masked with white. (b) The array of electrodes. One of the meshes can be seen as a dark area just to the right of the beam of light. The dashed curve indicates a particle trajectory towards the 3D detector. (c) The spectrometer mounted within the vacuum chamber. A gas needle extends into the interaction region from the bottom right. An alignment laser makes its tip visible as a bright spot. (d) View through the spectrometer before mounting detectors. The needle is visible from the top right (with a hand in the background).

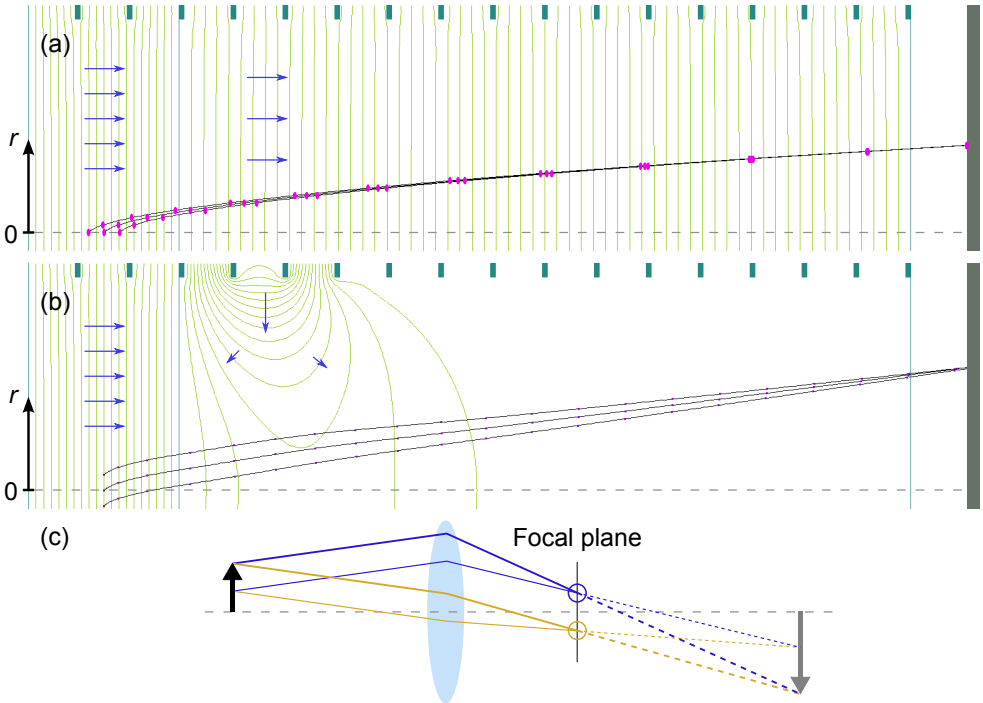

Figure 4.9: **Focusing of axial and radial momentum.** The zoomed-in simulations in (a–b) represent the interior of the electrode array in Fig. 4.8(b). Trajectories for 1 eV particles emitted at 45° angle are shown from three source points, spaced by 3 mm axially in (a) and radially in (b). The extraction voltage is $U_{\mathrm{ext}}/q = 20$ V and 2 V electric potential contour lines are shown in yellow.
(a) The magenta dots on the trajectories mark equidistant instants in time to visualize that the flight time to the first mesh depends on the start point. The weaker field in the second region is set ($b = 6$) to compensate for this, and a focusing of time markers can be seen near the detector (right side).
(b) Trajectories from different transverse positions are focused by an electrostatic lens, providing acceleration (arrows) towards the central axis (dashed). Conceptually this is similar to having a detector in the focal plane of an optical lens (c), where the emission angle rather than source point is imaged.

the centre, so that the same final x (or radius r) is reached for a given $\vec{p}$ regardless of x_0.[4] One can quantify the radial focusing quality by a deblurring factor [117] $\delta x/\delta x_0$ which should ideally be close to zero for all energies and emission directions. Figure 4.9(c) shows the close analogy between the focusing of particle trajectories and the focal plane of an optical lens. The deflection (bending) of trajectories is excessive for particles that pass the lens at larger radii, resulting in a shorter focal length for outer trajectories than for those at small radii. In the analogy to optical imaging, this means that the lens has spherical aberration and barrel distortion. The aberration prevents perfect focusing with a large aperture and the distortion means that the mapping between x and p_{x} is nonlinear. Better radial focusing can be achieved by using a strong extraction field to collimate particle trajectories into a narrow cone (paraxial rays) before the lens. The narrow cone will however also demagnify the image, so that the spatial resolution of the detector eventually becomes more of problem than the lens. A longer flight tube, or even a second lens, can be used to magnify the image again [118].

Total resolution

Combining the axial and radial resolution aspects one finds a conflict for electrons, due to the finite time-resolution of the detector: To resolve p_{z} well the extraction field should be weak but to improve radial focusing it should be stronger. 3D-imaging of electron momenta is therefore difficult when the transverse source size is large. The weak extraction field, needed to expand the p_{z}-information, also expands the flight time and the radial image. To maintain 4π angular collection for the same maximum energy despite the expanded radii, the detector needs bee moved closer (or made larger). Paper **VI** reports how to achieve a balance between electron (short drift tube, weak extraction) and ion (long drift tube, strong extraction, axial focusing) aspects. More parameters are used for the homogeneous (axial focusing) and inhomogeneous (radial focusing) fields to make the spectrometer adaptable to various applications although the geometry is fixed.

Thermal spread in the initial velocity becomes resolution limiting for small momenta, regardless of spectrometer design. The simplest gas source is an effusive gas jet. It injects gas at room temperature through a needle almost reaching the beam of light as shown in Fig. 4.8(c–d) and Fig. 4.10(b). The gas temperature can be reduced by using a molecular/atomic beam, where the gas is injected via an expansion nozzle [122] and is collimated through narrow skimmers. Although the beam reduces thermal spread, the average initial velocity $\vec{v}_{\mathrm{initial}}$ gives a time-of-flight (i.e. mass) dependent offset in the xy-image, $\vec{v}_{\mathrm{initial}}t$. This needs to be accounted for whenever small fragment velocities are studied for multiple masses.

[4] An influence of p_{z} on r, via the time of flight, is problematic for 2D imaging but can be accounted for in 3D imaging where p_{z} is measured.

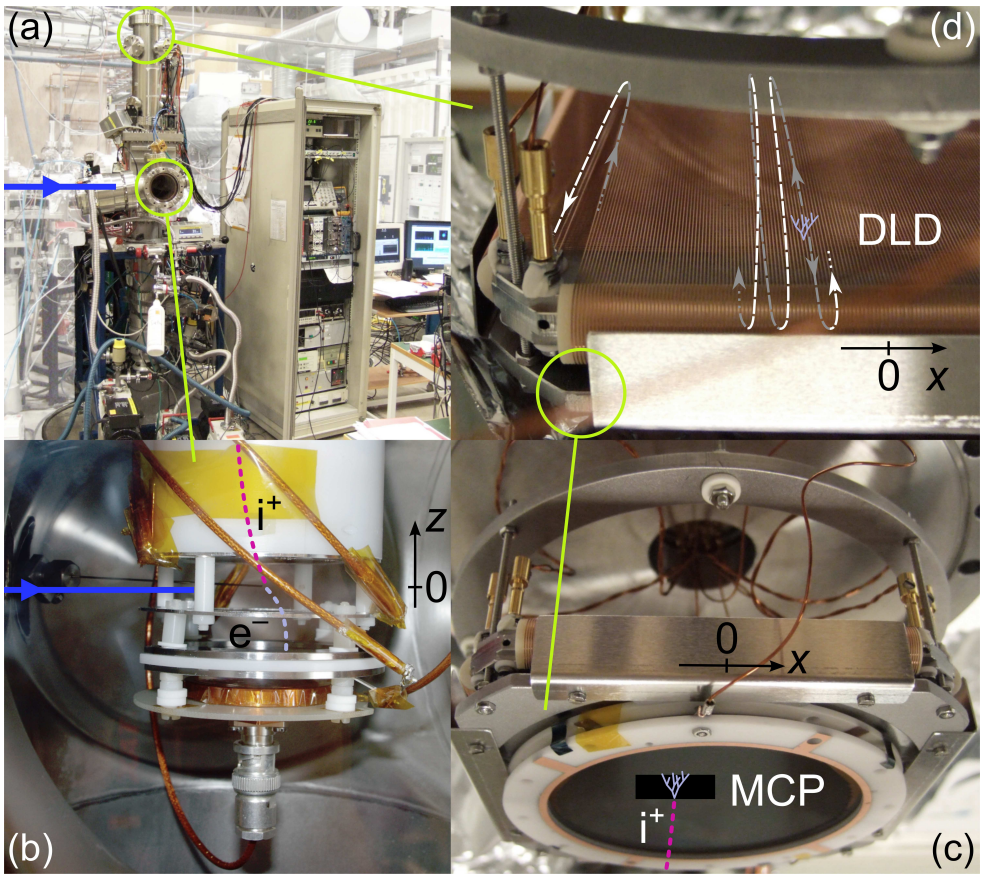

Figure 4.10: **Ion spectrometer for 3D-momentum and mass.** (a) Vacuum chamber and electronics attached to beamline I3, with incident XUV indicated from the left. The background has been masked with white. (b) Zoom-in on the interaction region, with gas needle and light from the left, electron detector just below and ion spectrometer extending upwards. (c) When an ion hits the micro-channel plate (MCP) at the top end of the spectrometer, it gives rise to an avalanche of electrons behind the MCP (d) where they induce a pulse on the delay line detector (DLD).

Detector types

If the time is not measured, but all particles have the same mass (or a time-gated detector is used) the (x, y)-distribution still gives two momentum components [123, 124]. If all ionizing photons are polarized along the same line in the xy-plane this is sufficient to deduce the 3D distribution via cylindrical symmetry – the so-called Abel inversion [125, 126]. For single ionization, when coincident detection is typically not of interest, there are advantages with using only two momentum dimensions: (i) Particularly for electrons, better 2D resolution [124] can be obtained when the p_z and time-dimension is ignored and a strong extraction field used. (ii) A camera can accumulate the 2D momentum image regardless of the number of ionization events per shot, allowing for faster experiments.

For 2D detection, often called velocity map imaging spectrometry (VMIS), we use a phosphorescent screen and a regular CCD-camera to record the data. For 3D momentum imaging we use a *delay line detector* (DLD) [60, 104] that gives x, y and t coordinates for individual particles[5], suitable for investigating correlations between different fragments of one dissociating molecule. They key parts of the 3D-spectrometer for ions are shown in Fig. 4.10. (a–b) give an overview and (c–d) explain the detector. Ions travel up through the spectrometer and hit a micro-channel plate, MCP in (c), where it gives rise to an avalanche of electrons. Behind the MCP (d) this induces a pulse on the delay line detector, DLD. Dashed curves illustrate how the pulse travels along the (pair of) wires coiled with a pitch in the x-direction (left–right). The electron cloud hits the DLD on the side facing away in the picture (grey curves) and leads to pulses propagating in each direction, looping via the visible side (white curves). The time difference between pulses reaching the left and right endpoints of the wire gives the x-coordinate of the hit. Inside the "x-coil" there is a perpendicular coil for readout of the y-coordinate.

[5] There is also a fourth, redundant, dimension in the raw data which can be used as a consistency-check.

Chapter 5

Applications

Using the methods presented earlier, the specific studies of electronic and molecular dynamics will be described here.

5.1 Attosecond electron dynamics

This section presents two very different approaches to access electron dynamics on the attosecond time scale: a pump–probe study of atomic double ionization and an angle-resolved study of single ionization of a large molecule. In the atomic case, the quantum mechanical two-electron correlation is analysed by electron interferometry. The spectral analysis is presented more extensively here than what could be included in Paper **I**. In the molecular case, the correlated motion (plasmon) the valence electrons in C_{60} with respect to the "cage" of nuclei is discussed in terms of classical physics for a conducting sphere. In both cases, we obtain information about the derivative of the scattering phase – the group delay of the electron or electron pair – which is closely linked to the forces experienced by the electrons during ionization.

5.1.1 Time-resolved double ionization of xenon

Measurements on the two electrons emitted during double ionization are essential for investigating dynamics in multi-electronic systems [127]. Electronic processes occur on the attosecond time scale, which until recently has not been directly accessible in experiments [128, 129]. Two studies of argon using strong laser fields succeeded in obtaining information about when, within a few-cycle laser pulse, the first and second electrons were set free. The Coulomb potential of the ion is negligible in such studies and the free-electron propagation is determined solely by the laser field – using either its direction [130, 131] or magnitude [27] to map emission times onto the observable electron momentum. The role of the interaction between electrons (bound as well as free) can be highlighted by using a weak (perturbative) field, where only one or two photons are absorbed to provide the energy.

Perhaps the most fundamental processes where electron correlation can be studied is the *direct* double ionization by one photon. Because this cannot occur without

interaction between the electrons it provides a stringent test for advanced theories, particularly in helium where it is the only double-ionization process and the system is limited to three bodies. Although the high double-ionization threshold of helium has so far discouraged attosecond time-resolved experiments, a fairly good understanding has been achieved through studies of differential cross sections (i.e. angular distributions) [16, 132]. Great theoretical challenges remain for all other atoms and molecules [133] due to the additional electrons.

For the one-photon double ionization study reported here, xenon was chosen as sample for its low double ionization threshold, above which attosecond pulse trains could be readily generated. Two-electron coincidence spectra have been reported for xenon without time resolution [14] as well as on the multi-femtosecond time scale [15], in the latter case including angular information.

Xenon is a heavy noble gas atom with 54 electrons, making it a showcase for multi-electronic effects [14, 134]. The $5p^{-1}$ and $5s^{-1}$ ionization energies are 12.1 and 23.4 eV while the $5p^{-2}$ double ionization threshold is 33.1 eV. In the 30–38 eV region of interest, Xe^{+*} Rydberg states [135] (left side of Fig. 5.1) can be described either in the LS or the jK coupling scheme [136–139][1]. The importance of correlation is manifested by the fact that no single configuration contributes more than 50 % to the configuration mixture [137, 140], regardless of coupling scheme, and the assignment is still subject to research [141]. Due to strong spin–orbit interaction the fine-structure spans a much larger energy range than in lighter elements: 4.5 eV for the dication ground-state configuration (right side of Fig. 5.1).

Information about time delays in double ionization was obtained in our experiment via electron interferometry with a weak infrared probe (RABBIT). When extending the interferometric measurement principle from single ionization to a two-electron wave packet, some fundamental questions need to be considered:

- Can we measure a time for *direct one-photon* double ionization?
- And how is *one* time-delay associated with a *pair* of electrons?

To answer the former, one- and two-photon double ionization processes in xenon will be described and used to fully assign the two-electron spectrum. The time measurement is described thereafter and in Paper **I**.

One-photon double ionization of xenon

In contrast to helium, where the ground state is accurately known (reviewed in [33, sec. 1.1.2]) and double ionization removes all the electrons, additional electrons remain in heavier atoms and molecules. This enables *indirect* double ionization processes [142], where the system first relaxes to a singly-charged excited intermediate state. Eland and co-workers' investigation of the complex one-photon double ionization of xenon by two-electron coincidence spectra [14] has been instrumental for the analysis of our spectra.

[1] To distinguish the $(^3P_{J_c})$-series implies the use of jK coupling, while to discuss singlet and triplet cores implies LS coupling. The former is found in high-resolution literature for $n \leq 6$ [137, 139] and the latter for higher n [36, 138]. A mixed notation (both $^{2S_c+1}$ and $_{J_c}$) is used in Fig. 5.1.

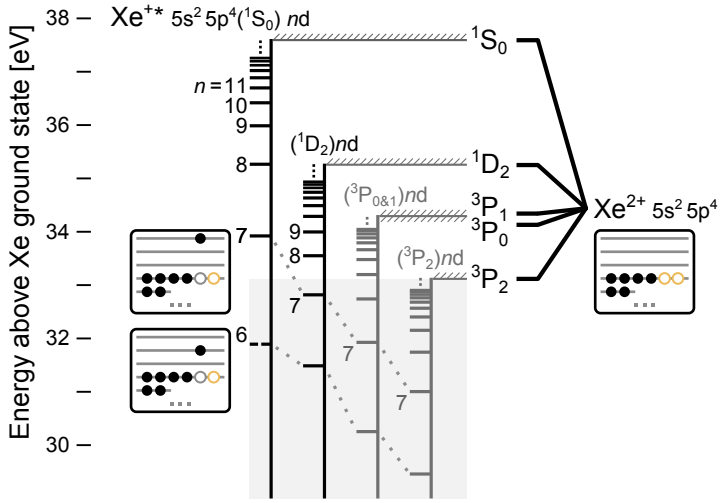

Figure 5.1: **Rydberg series in Xe^+, converging to Xe^{2+}.** Only the (black) series with singlet Xe^{2+} cores are needed to explain one-photon spectra [14, 138]. Triplet series, $^3P_{J_c}$ (grey), are guessed by comparing literature and our data.

To explain direct double ionization, the two mechanisms schematically illustrated Fig. 5.2 are often considered [9]. *Knockout* applies a classical mechanics perspective where the first electron starts to leave the ion and collides with another electron to "knock" it out of the ion. *Shake-off* is a purely quantum mechanical consequence of the electron orbitals being slightly different in the cation than in the neutral atom. Absorption of a high-energy photon suddenly removes one electron so that the relaxation of the remaining electronic wavefunction can be described as a projection onto the new basis set of the ion. Since these basis sets are not orthogonal, overlap exists for many final states and there is a finite probability for the projection to "shake" an electron to a different orbital as well as to the continuum. A simple motivation for neutral and ionic orbitals being different is that the screening of the nucleus is reduced when there are fewer electrons (particularly in inner shells). At moderate (XUV) photon energies, the sudden approximation is less accurate, but we will see that correlation between (sub)shells plays a role in xenon.

The dominant double ionization process is *indirect*, meaning that the first step is single photoionization with shake-up to excited states of Xe^{+*}. States lying above the double ionization threshold (see Fig. 5.1) then decay by autoionization to Xe^{2+}. For states near the threshold, electron correlation is important and the relaxation is dominated by *conjugate* shake-up[2] [143, 144]. Only excited states with the outer

[2] A shake process involves a dipole transition for one electron and a monopole transition for another electron. With respect to the normal shake, conjugate shake swaps the final angular momenta between photoelectron and excited electron. This can be explained by involving configuration-mixed states [36, 37], see Fig. 5.7. With γ representing the photon, an example of shake-up is $\gamma + 5p^6 \rightarrow 5p^4\, np\, \epsilon d$ in the normal case and $\rightarrow 5p^4\, nd\, \epsilon p$ in the conjugate case.

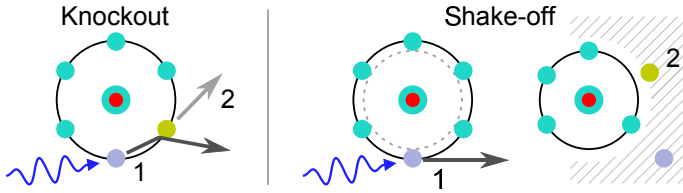

Figure 5.2: **Mechanisms for direct double ionization upon absorption of one photon.** Energy from the primary photoelectron (1) is transferred to the secondary (2) via a collision (knockout) or when initial wavefunctions are projected onto the ionic basis set (shake-off).

electron in d-subshells are necessary to understand the spectra [14, 36, 138, 140]. Their energies are well described by one *Rydberg series* per fine-structure level of the Xe^{2+} $5p^4$ dication, detailed in Fig. 5.1. Each cation state has a dication core (of energy E_I) and an nd-electron bound to it, strongly when $n = 6$ and asymptotically free when $n \to \infty$. With $E_{Ry} \approx 13.6$ eV as the Rydberg unit of energy, the resulting Xe^{+*} energy can be approximated by

$$E_n \approx E_I - \frac{E_{Ry} Z_{eff}^2}{(n-\mu)^2} \tag{5.1}$$

where the quantum defect, μ, and the effective charge, Z_{eff}, are introduced to account for the extended size of the core [34]. In a hydrogen atom the core is simply a proton and exact energies are given with $Z_{eff} = 1, \mu = 0$. The 54 protons and 52 electrons of the Xe^{2+} core result in an effective charge of 2 at large radii (large n) but the screening is incomplete at smaller radii and correlation with other electrons may cause further deviations. It is more common to use only either μ or Z_{eff} as parameter, introducing a n-dependence in $\mu(n)$ if necessary, but the form with two constant parameters has been used for multi-electron systems [145–147]. Both parameters were fitted[3] to reference data so that the entire series (any n) could be included in the model of our experimental spectra. In the Xe^{+*} $(^1S_0)nd$ ^2D series, no energy for $n = 6$ seems to have been reported. The fit to data from Ref. [14] can be extrapolated to 31.0 eV for $n = 6$, but instead of breaking the trend between cores (dotted in Fig. 5.1) an unassigned experimental energy from Ref. [138] is used (broken line).

[3] Z_{eff} and μ were fitted to energies in the literature [14, 36, 137–140]. For $(^1S)nd$ with $E_I = 37.59$ eV: $Z_{eff} = 2.03, \mu = 3.09$. $(^1D)nd$, $E_I = 35.25$ eV: $Z_{eff} = 2.16, \mu = 1.89$. $(^3P)nd$, $E_I = 34.29$ eV (unresolved $J_c = 0$ and 1): $Z_{eff} = 1.78, \mu = 2.74$. For the latter series, an alternative $\mu \approx 2$ with Z_{eff} fixed at the more expected value of 2 would for $n \geq 9$ still give errors below 0.1 eV.

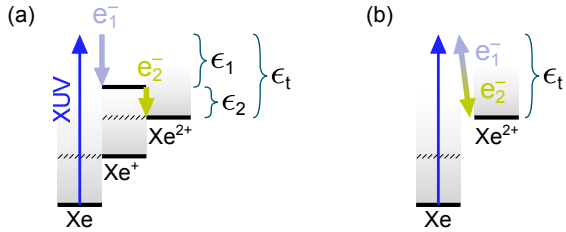

Figure 5.3: **Kinetic energies in the spectral model.** (a) Indirect double ionization is simulated in two steps, with the discrete kinetic energies ϵ_1 and ϵ_2. (b) For direct double ionization, discrete structure is only present in the total energy, ϵ_t.

Spectral model with XUV photons

To analyse our electron-pair spectra, a spectroscopic model was developed. Its principle is here explained for one-photon (XUV) processes, before including two-photon (XUV & IR) contributions.

For indirect double ionization, the discrete intermediate state suggests a model with two steps: a photoelectron of energy ϵ_1 and a secondary electron of energy ϵ_2. This is illustrated in Fig. 5.3(a). The photoelectron and the secondary electron are in general not distinguishable: experimentally they will be labelled by their energies, ϵ_{fast} and ϵ_{slow} with $\epsilon_{\text{slow}} < \epsilon_{\text{fast}}$. For the present analysis, most of the spectrum can be read by associating "slow" with "secondary" but both energy permutations are considered in the simulation (compare Fig. 4.2(a)). The total kinetic energy, $\epsilon_t = \epsilon_{\text{fast}} + \epsilon_{\text{slow}} = \epsilon_1 + \epsilon_2$, is not dependent on electron labelling and will be used as one axis. For direct double ionization, the lack of discrete intermediate states leads to an arbitrary energy sharing between the electrons, illustrated by a continuously coloured double-arrow in Fig. 5.3(b).

The two-electron spectrum is simulated by adding incoherent intensity contributions from direct and indirect double ionization (DI):

$$I(\epsilon_t, \epsilon_{\text{slow}}) \propto \sum_H I_H \sum_f \Big(F_{\text{dir}}(\epsilon_t, \epsilon_{\text{slow}}) + \big[F_{\text{ind}}(\epsilon_t, \epsilon_{\text{fast}}) + F_{\text{ind}}(\epsilon_t, \epsilon_{\text{slow}}) \big] \Big) , \quad (5.2)$$

where I_H is the intensity of harmonic H and f enumerates the five final states of Xe^{2+}. The definitions of the terms F_{dir} for direct and F_{ind} for indirect will be given below (implicit dependencies on the iteration variables have been hidden).

The contribution from direct double ionization,

$$F_{\text{dir}}(\epsilon_t, \epsilon_{\text{slow}}) = \frac{\partial \sigma_{\text{dir},f}}{\partial \epsilon_{\text{slow}}} \times P_t(\epsilon_t) , \quad (5.3)$$

is the energy-differential cross section, $\partial \sigma_{\text{dir},f} / \partial \epsilon_{\text{slow}}$ for the final state f, multiplied by a function $P_t(\epsilon_t)$ expressing the spectral peak profile for the energy $H\hbar\omega - E_f$ (section 4.2). No dependence on ϵ_{slow} is included[4]. This means that each direct con-

[4] A U-shaped spectrum (along either electron energy axis) with an intensity minimum at $\epsilon_t/2$ is known from helium [8, 9] but not pronounced near threshold in Xe [14].

tribution to the two-electron spectrum (Fig. 5.4(d)) is a homogeneous stripe at a particular total kinetic energy. Integration along this stripe relates the differential cross section to the total cross section, $\sigma_{\mathrm{dir},f}$:

$$\sigma_{\mathrm{dir},f} = \int_0^{\epsilon_\mathrm{t}/2} \frac{\partial\sigma_{\mathrm{dir},f}}{\partial\epsilon_\mathrm{slow}}\,\mathrm{d}\epsilon_\mathrm{slow} \;\Leftrightarrow\; \frac{\partial\sigma_{\mathrm{dir},f}}{\partial\epsilon_\mathrm{slow}} = \frac{2}{\epsilon_\mathrm{t}}\sigma_{\mathrm{dir},f}\,. \tag{5.4}$$

Supported by Ref. [14] and our data, $\sigma_{\mathrm{dir},f}$ is approximated as energy-independent. One may note that Wannier's law, applicable closer to the threshold, would have $\sigma_{\mathrm{dir},f} \propto \epsilon_\mathrm{t}^{\alpha}$ with $\alpha \approx 1$ [148].[5]

The indirect double ionization contribution is constructed by adding the contribution from each discrete intermediate state. The state is denoted using the principal quantum number, n, and a variable s to tell which of the Rydberg series $\{(^1\mathrm{S})n\mathrm{d}$, $(^1\mathrm{D})n\mathrm{d}$ and $(^3\mathrm{P})n\mathrm{d}\}$ it belongs to. The first step is shake-up to a Xe^{+*} state of energy $E_{s,n}$, with the excitation cross-section $\sigma_{s,n}$. This state may decay by various competing processes p of rate $\Gamma^p_{s,n,f}$ to final state f. With only an XUV photon, the processes are autoionization (AI) and fluorescence[6]. Although the fluorescence rate is low, it is relevant for high n [149] and states below threshold (sequentially ionized, see next section). The contribution to the two-electron spectrum is given by the probability (quantum yield) for autoionization and peak shape functions:

$$F_\mathrm{ind}(\epsilon_\mathrm{t},\epsilon_2) = \sum_s \sum_{n=6}^{100} \sigma_{s,n} \times \frac{\Gamma^\mathrm{AI}_{s,n,f}}{\sum_p \sum_f \Gamma^p_{s,n,f}} \times P_\mathrm{t}(\epsilon_\mathrm{t})\,P_2(\epsilon_2)\,, \tag{5.5}$$

$$\text{where}\quad \Gamma^\mathrm{AI}_{s,n,f} = \frac{\tilde{\Gamma}^\mathrm{AI}_{s,f}}{(n-\mu_s)^3} \quad\text{and}\quad \sigma_{s,n} \approx \frac{\tilde{\sigma}_s}{(n-\mu_s)^3}\,.$$

The two-dimensional peak shape has the same total-energy factor, P_t, as for direct DI but also the peak shape for the secondary electron, P_2, located at the energy difference between intermediate and final states, $E_{s,n} - E_f$. As shown below equation (5.5), autoionization rates within a series are given by one *reduced* autoionization rate $\tilde{\Gamma}^\mathrm{AI}_{s,f}$ [149–151]. Note that its value will be much larger than the actual rates due to the scaling by $(n-\mu_s)^{-3}$, where μ_s is the quantum defect of the series. Also the shake-up cross section, $\sigma_{s,n}$, is modelled to follow such a scaling [144, 149]. The values of $\sigma_{s,n}$ are shown in Fig. 5.4(a), after adjustments at some $n \leq 10$ to fit our data (including two-photon data). Adjustments that redistribute cross section between the series, e.g. the increase in $(^1\mathrm{D})$ and reduction in others at $n = 10$ could be related to configuration interaction.

The model parameters were essentially determined by first fitting the $^1\mathrm{D}_2$ stripe, which can only be reached by AI from the $(^1\mathrm{S})n\mathrm{d}$ series and by direct DI, and then proceeding with the other final states. Figure 5.4(b) compares the resulting simulation with the experiment, selected from the electron pair-spectrum (c) for

[5] Intensity in the two-dimensional spectrum is proportional to $\partial\sigma_{\mathrm{dir},f}/\partial\epsilon_\mathrm{slow}$. To avoid divergence when $\epsilon_\mathrm{t} \to 0$ in eq. (5.4), a Wannier-like constant intensity ($\alpha = 1$) is used below 0.5 eV.

[6] For fluorescence the only final state considered is the cation ground state at $E_\mathrm{g.s.} = 12.1$ eV, with a classical rate estimate [34] proportional to $(E_{s,n} - E_\mathrm{g.s.})^2$.

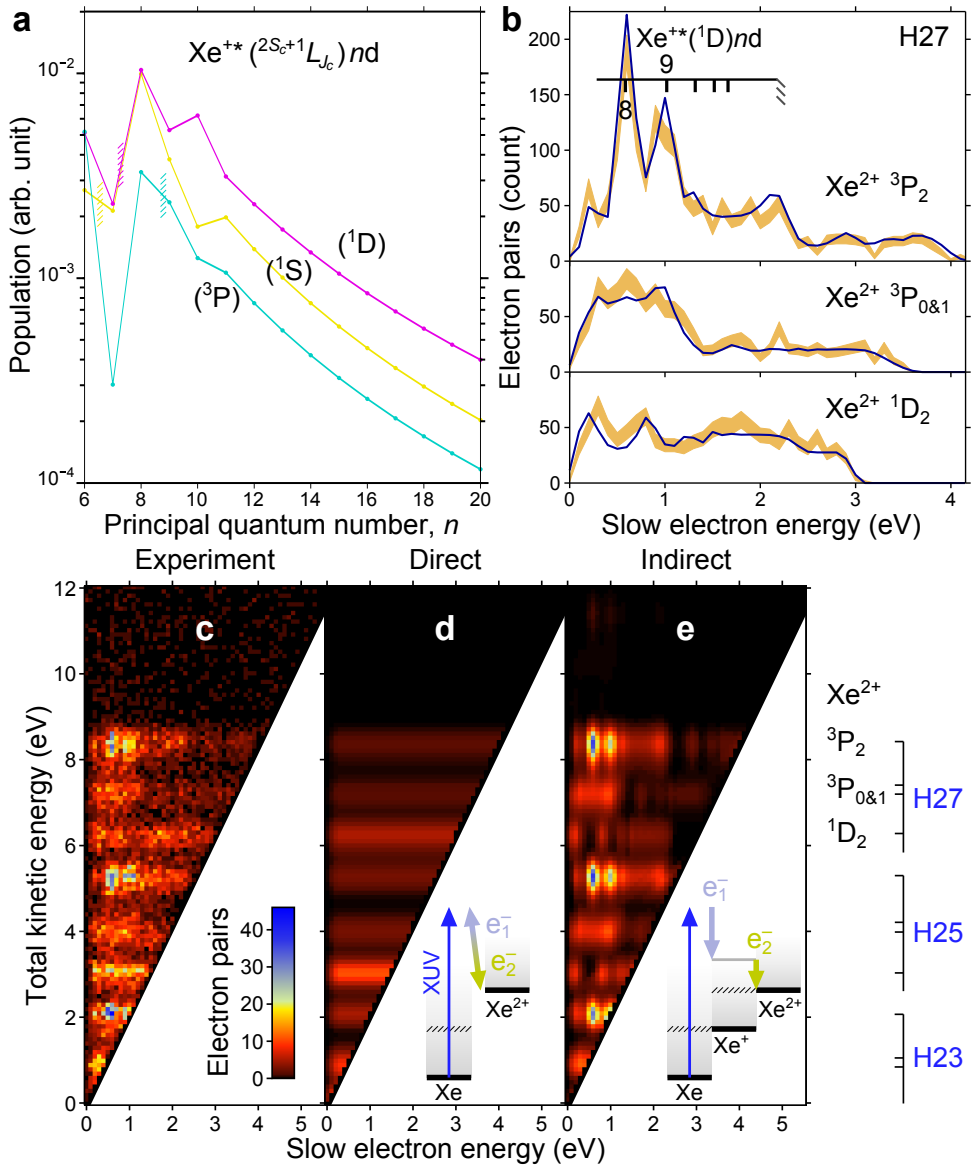

Figure 5.4: **Calibration of the double ionization model to experimental data.** (a) Shake-up during single ionization populates Xe^{+*} states with an intensity proportional to $(n - \mu_s)^{-3}$, here adjusted at low n to fit our data. States to the left of the hatched lines are below the 33.1 eV double ionization threshold. (b) Comparison of one-photon experiment and simulation, within stripes of the two-electron spectrum corresponding to different final states for harmonic 27 (41.6 eV photon energy). The experimental data (orange curves) comes from the two-electron coincidence spectrum in (c) and the simulation (blue curves) is the sum of (d) and (e). (e) is the result of autoionization of the states in (a).

Table 5.1: **Comparison of intensities in the two-electron spectrum.** The relative intensities (branching ratios) obtained from the model are shown for harmonic 27 (41.6 eV photon energy) to be compared with the experimental analysis from Ref. [14] (40.8 eV) and the statistical weight. In the middle part of the table, indirect and direct double ionization (DI) are separated. In the bottom part, the total intensity is renormalized to ease the comparison.

	Xe^{2+} final state				
	$^3P_2$	$^3P_0$	$^3P_1$	$^1D_2$	$^1S_0$
Total kinetic energy (eV)	8.5	7.5	7.3	6.4	4.0
Statistical weight	5	1	3	5	1
Indirect DI	8.5	0.7	2.1	3.3	-
Direct DI	2.8	0.6	1.7	6.0	0.12
Ref. [14] direct DI	4.6	0.9	1.7	5	0.9
Total / 1.76	6.5	0.7	2.2	5.3	0.07
Ref. [14] total	6.5	1.1	2.3	5	0.8

harmonic 27 and different final states. The Xe^{2+} $^1S_0$ final state at 4 eV total kinetic energy for harmonic 27 overlaps $^3P_{0,1}$ for harmonic 25 and is not labelled in the figure. The full simulation is shown with the direct contribution in (d) and the indirect in (e).

The ratios between reduced cross sections (and thus intensities) for direct DI were initially taken to follow the $2J+1$ statistical weight of the final states [14]. The fitting led to an increase of $^1D_2$ and reduction of $^1S_0$, resulting in the direct branching ratios in Table 5.1. This table also shows indirect intensities for harmonic 27, with the exception that there can be no autoionization towards $^1S_0$. All quantities are compared with the results of Eland *et al.* for a similar photon energy [14]. The most striking deviation is that our direct model intensity for $^1S_0$ is lower than expected. Some of this may be due to the fact that its kinetic energy (4 eV) overlaps the harmonic 25 contribution to $^3P_{0,1}$ but branching ratios for $^3P_{0,1}$ are on the low side also within harmonic 25. Eland *et al.* observed that only the $^1S_0$ intensity followed a Wannier-like trend with photon energy, in agreement with the low $^1S_0$ intensity found by threshold photoelectron coincidence spectroscopy [152].

The lifetimes of Xe^{+*} states are expected to lie in the femtosecond to picosecond range (varying with n). The width of peaks along the slow electron axis is therefore dominated by the spectrometer resolution (0.07 eV standard deviation for the Gaussian in section 4.2). For the dominant Xe^{+*} states the fluorescence rate is negligible compared to autoionization. Thus neither natural linewidth nor the fluorescence rate offers a clear absolute rate reference and as long as the *ratios* between rates to different final states are preserved, an absolute rescaling (by one order of magnitude) does not affect the simulated spectrum much. As a consequence, the magnitude of the reduced rates presented in Table 5.2 should mainly be compared within rows although a nominal unit of fs^{-1} is given. This table underlies the simulation that leads to the indirect DI information in Table 5.1.

To compare intensities with the experiment in Fig. 5.4(b) and Paper **I**, a flat noise background is added, fitted to the average above 9 eV in Fig. 5.4(c).

Table 5.2: **The reduced autoionization rates, $\tilde{\Gamma}^{\mathrm{AI}}_{s,f}$, used in the model.** Actual rates are obtained by dividing the reduced rate by $(n-\mu_s)^3$. The rates are given in a nominal unit of 10^{15} s^{-1} for the order of magnitude but should mainly be compared within rows. Unreachable final states are marked with hyphens.

Rydberg series, s	Xe^{2+} final state, f				
	$^3P_2$	$^3P_0$	$^3P_1$	$^1D_2$	$^1S_0$
$(^1S)n$d	12	2.4	7.2	24	-
$(^1D)n$d	40	16	48	-	-
$(^3P)n$d	36	-	-	-	-

Spectral model with two colours

For the measurement of photoelectron group delays by electron interferometry, an infrared probe photon is introduced. This leads to nonsequential and sequential double ionization processes which need to be identified in the two-electron spectrum before temporal information can be analysed.

By *nonsequential* DI we mean that both electrons are still emitted as a consequence of the XUV ionization (direct or indirect) and that the infrared only redistributes their energies, causing interference at "total-energy sidebands". In the direct case, sidebands due to absorption/emission of an infrared photon are obtained by including even orders, H, in equation (5.2). The same is done for indirect DI, meaning that nonsequential indirect DI in the model only considers infrared absorption/emission by the primary photoelectron (leading to the kinetic energy ϵ_1)[7].

When indirect double ionization occurs *sequentially*, Xe is ionized by the XUV and then Xe^{+*} by the IR. This means that the second electron is ejected after interaction with an IR-photon and that ϵ_2 is increased[8] with respect to the autoionization case. Sequential IR absorption appears as an additional process that competes with autoionization and fluorescence in equation (5.5).

Figure 5.5 compares the experimental spectrum with XUV and IR in (a) with the simulation. While the supplement of Paper **I** displayed the full simulation, Figure 5.5(c–g) shows the various processes separately and without the XUV-only background. To ease the comparison, such a sideband-only spectrum is emulated for the experimental data in (b) by taking the difference between XUV&IR and XUV-only spectra and applying noise reduction.

The nonsequential processes in (c–d) give sidebands shifted $\hbar\omega = 1.5$ eV up and down in total energy with respect to Fig. 5.4(d–e). From each harmonic 13 % of the intensity is transferred to the sideband above and 13 % to that below (depleting the XUV-only terms in the simulation). Furthermore, the reduced excitation cross sections in sidebands were adjusted by +20 % for $(^1S)n$d and −20 % for $(^1D)n$d.

[7] Absorption by the secondary electron would be energetically identical to sequential DI. Because the momentum-gauge dipole operator is proportional to the momentum ($\sqrt{\epsilon_i}$) [153], absorption/emission by the low-energy electron, which is usually the secondary, should be less likely.

[8] Also energy reduction due to stimulated emission from above-threshold states is included if it gives positive kinetic energy [153], but all above-threshold sequential rates are too weak to be seen.

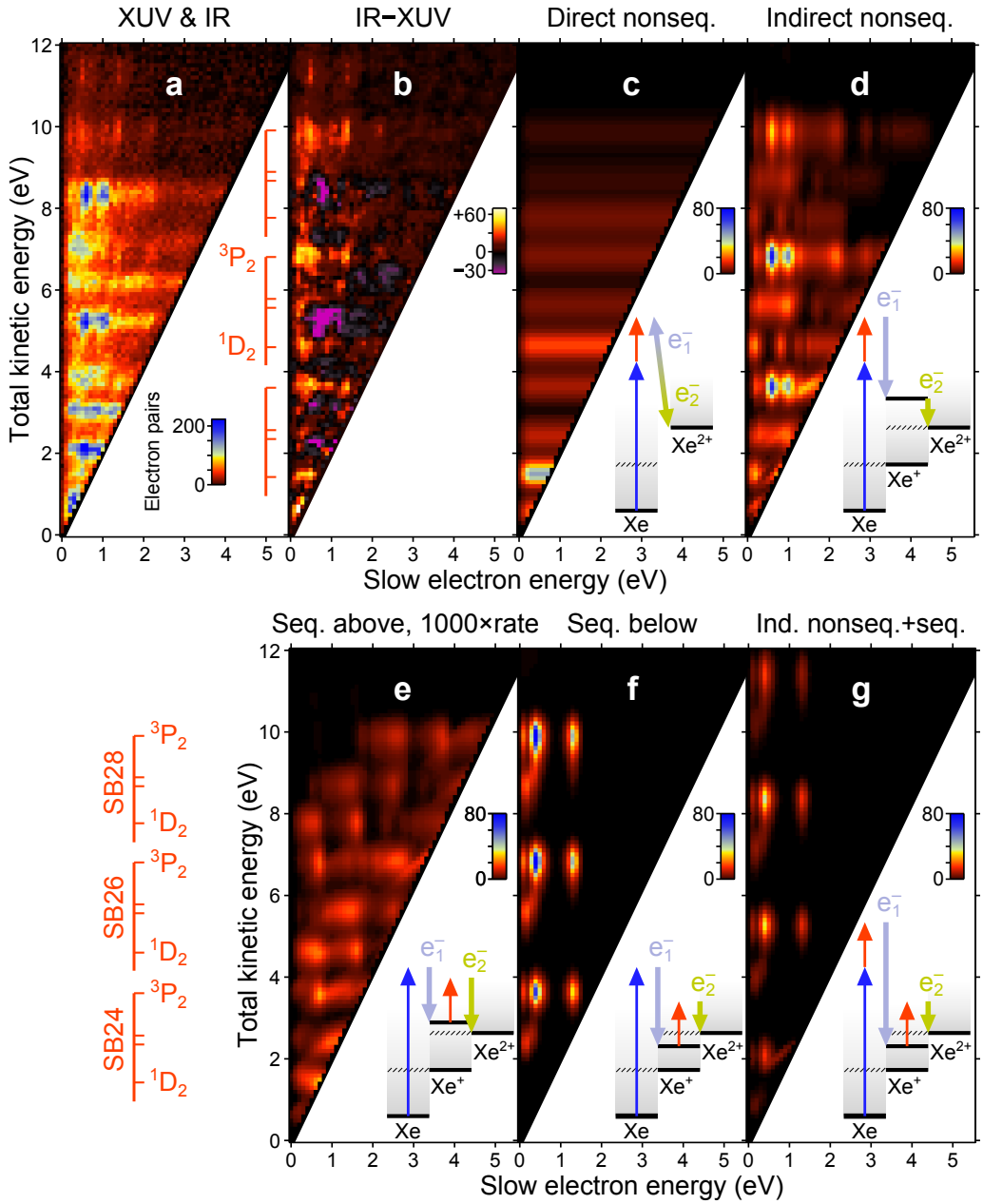

Figure 5.5: **Effects of the infrared probe on the electron-pair spectrum.** Experimental data with XUV and IR is shown in (a). In (b) its difference from the spectrum without IR (noise-reduced by a $\sigma = 0.1$ eV Gaussian). The remaining panels show simulated IR-processes: (c) direct, (d) indirect nonsequential, (e–f) sequential from above/below the DI threshold, and (g) two IR photons, combining non-sequential and sequential absorption. The sequential rate is increased by a factor 1000 in (e) compared to the actual simulation.

Sequential processes are shown in Fig. 5.5(e) if the Xe^{+*} state is above the double ionization threshold, otherwise in (f). The experiment in (a–b) does not contain the above-threshold structure simulated in (e); the difference is most striking at 10 eV total energy. We therefore conclude that autoionization dominates over sequential absorption, presumably due to the low IR intensity used. To still make the above-threshold sequential process visible for this comparison of spectral structure, it is shown with 10^3 times the actual model rate in (e). Sequential rates independent of n are used, but a similar structure and the same conclusion would be found with an $(n - \mu_s)^{-3}$ factor.

The low sequential rate that we found is still sufficient to compete with fluorescence, so sequential DI via states below the threshold is seen in (f) and the experiment. In the two-electron spectrum, peaks due to sequential DI usually appear shifted in the 45° direction with respect to the autoionization peaks in Fig. 5.4(e), because both the total and slow electron energies increase by 1.5 eV when the slow electron gains the IR photon energy (photoionization instead of autoionization in the second step).

Harmonic 29, resulting in up to 11.5 eV total kinetic energy, was hardly seen in the XUV-only experiment, but peaks with another structure in that energy region appeared when the IR was present[9]. By allowing sequential ionization of Xe^{+*} also when the primary electron has interacted nonsequentially, this structure was reproduced in Fig. 5.5(g). Two IR photons are absorbed in this case and the sequential rate is tripled. Since below-threshold states in Xe^{+*} only contribute to the spectrum via sequential ionization, it is not possible to know for certain how much of this change lies in their XUV-excitation cross section and how much lies in the sequential rate. The cross section was kept constant in the simulation.

The two-electron simulation can be summarized by two stages: XUV-only and nonsequential XIV±IR ionization first populates cation states and gives direct DI, then all indirect DI is obtained via competing decay rates. The simulation based only on energy sharing and three Rydberg series gives a very good understanding of the mechanisms behind the experimental spectra. Based on this one finds a few sideband regions for the $^1D_2$ final state where direct nonsequential DI is stronger than indirect DI, e.g. at 4.6 eV total energy near the diagonal of equal energy sharing[10]. Identifying direct DI regions was a prerequisite for analysing photoemission times theoretically as described in the next section and Paper **I**.

Photoemission time delay for direct double ionization

The identification of nonsequential sidebands for direct double ionization allows the interferometric technique explained in sections 2.4.2 and 3.3 to be applied. When the delay of the IR-probe is scanned with respect to the XUV harmonics, intensities in

[9] Measurements with IR on and off in parallel (using a shutter wheel) during one scan show that this is not just due to a change in H29 intensity between measurements. The observed I_{29}/I_{27} intensity ratio of 4 % for double ionization but only 0.01 % for 5p single ionization seems related to H29 (at 45 eV) being in the photoionization Cooper minimum of Xe [62, 154].

[10] The assignment of this region is also supported by the lack of back-to-back electron emission observed with femtosecond XUV-pulses [15, Fig. 16(b)].

the two-electron spectrum (Fig. 5.6(a)) oscillate. By referencing the oscillation phase (τ_{exp} in delay) to that for the same sideband order in single ionization, a map of the group delay of the two-electron wave packet is obtained, as shown in Fig. 5.6(b).

The assignment in Fig. 5.5 found that sequential processes (f–g) were confined to at most 1.5 eV for the slow electron. To the right of the vertical dashed line in Fig. 5.6(b) only nonsequential processes occur, for direct as well as indirect DI. Although the greatest average intensity is found in spots of indirect DI the most significant oscillations were found for direct DI.

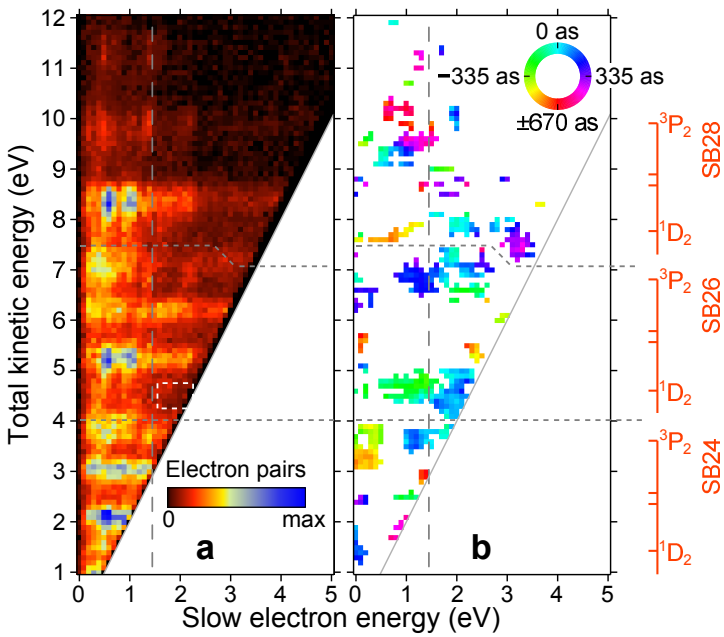

Figure 5.6: **Experimental maps of intensity and delay for the electron pair.** (a) The two-electron spectrum with XUV and IR. (b) Two-photon group delay with respect to single ionization for the same sideband order, $\tau_{\mathrm{DI}}^{\mathrm{2ph}} - \tau_{\mathrm{SI}}^{\mathrm{2ph}}$. Xe^{2+} final states are labelled on the right-hand side and horizontal lines separate the regions for sideband (SB) 24, 26 and 28. To the right of the vertical line at 1.5 eV only nonsequential DI is seen and direct nonsequential DI dominates for the $^1D_2$ final state. The interferometric measurement principle leads to a cyclic colour scale, indicated as a clock. Non-oscillating areas are masked in white. The white box in (a) indicates the region analysed in the text. The single ionization time references, subtracted to cancel the chirp of the attosecond pulses, are related by $\tau_{\mathrm{SI,SB26}}^{\mathrm{2ph}} - \tau_{\mathrm{SI,SB24}}^{\mathrm{2ph}} = 241 \pm 21$ as and $\tau_{\mathrm{SI,SB28}}^{\mathrm{2ph}} - \tau_{\mathrm{SI,SB26}}^{\mathrm{2ph}} = 582 \pm 58$ as. To assign contiguous oscillating areas to the same sideband, a step was introduced in the border between SB26 and SB28 (near 7 eV). Without this step, an unexpected colour change of ±582 as would occur within the area crossing the border.

An analysis of delays in indirect nonsequential and sequential DI would need to consider the polarizability of the cation. The evolution of neutral samples "dressed" by laser fields have recently been analysed from different perspectives (e.g. [155, 156] and references therein) but it was outside the scope of the present work. In two-photon (XUV+XUV) single-ionization of helium, the pulse duration has been shown to influence the angular distribution (related to delay via the scattering phase) when sequential and non-sequential contributions interfere [157]. Other complications concern the lifetime of the cation. The lifetime before sequential ionization should be influenced by the IR intensity and make the result dependent on laser parameters. For indirect nonsequential DI, the considerable autoionization lifetime may lead to emission of the secondary electron after the end of the 30 fs IR pulse. In that case, the interferometric experiment probes the single ionization step rather than double ionization. For these reasons, and to approach the formalism developed for the three-body problem in helium, the time analysis presented in Paper **I** was concentrated on direct DI. In this case the continuum electron pair is created by one XUV-photon, and the measured group delay $\tau_{\mathrm{DI}}^{\mathrm{2ph}} = \tau_{\mathrm{DI}}^{\mathrm{1ph}} + \tau_{\mathrm{cc}}$ gives access to the one-photon time $\tau_{\mathrm{DI}}^{\mathrm{1ph}}$ if the continuum–continuum delay τ_{cc} is calculated.

To answer the question of how *one* time is associated with a *pair* of electrons I will here explain a few parts of the theoretical supplement of Paper **I**. In our calculation of the direct DI delay, using multi-body perturbation theory, we currently approximate the IR photon to interact equally likely with the primary and secondary electron (which are indistinguishable in the spectrum). The kinetic energy domain for the wave packet is two-dimensional (ϵ_1, ϵ_2) but the two electrons are not independent – the sum of their kinetic energies is quantized by photon and dication energy. A group delay for each electron can be defined by differentiation of the scattering phase along each axis $(\hbar\partial\eta/\partial\epsilon_i)$, most easily pictured in the coordinate system of Fig. 4.2(a). Just like the diagonal direction of *total energy* was found to be more relevant than either individual energy axis (compare Fig. 5.4(d)), we define the "pair time delay" by differentiation of the scattering phase along a direction where both energies change. Because we assumed equal amplitudes of matrix elements for interaction with either electron[11] the direction of differentiation is the diagonal of equal energy sharing, equivalent to the average of the individual electron times: $\tau_{\mathrm{DI}}^{\mathrm{1ph}} = \hbar(\partial\eta/\partial\epsilon_1 + \partial\eta/\partial\epsilon_2)/2$.

For the Xe^{2+} $^1D_2$ final state, near the diagonal of equal energy sharing, the modelling in Fig. 5.5(c–d) revealed that direct nonsequential DI dominates over indirect. In Fig. 5.6(a) this region is marked by a dashed white rectangle for sideband 26[12] and (b) shows that it oscillates with a group delay of $\tau_{\mathrm{DI}}^{\mathrm{2ph}} - \tau_{\mathrm{SI}}^{\mathrm{2ph}} = 55 \pm 61$ as with respect to $5p^{-1}$ single ionization (SI). While this means that the sideband 26 for DI and SI are practically oscillating in phase, the underlying one-photon delay is much longer for double ionization. To find its value, one needs τ_{cc} calculated for two-electron wavefunctions with partial screening of the ion. My collaborators' theoretical work behind this will not be described here but because the screening is different for

[11] Non-equal amplitudes can in principle be handled by using a four-path matrix element, coherently including absorption/emission by either electron.

[12] The two quantum paths brought to interfere in sideband 26 are harmonic 25 and 27 in Fig. 5.4(d), i.e. one-photon wave packets of 3 and 6 eV total kinetic energy.

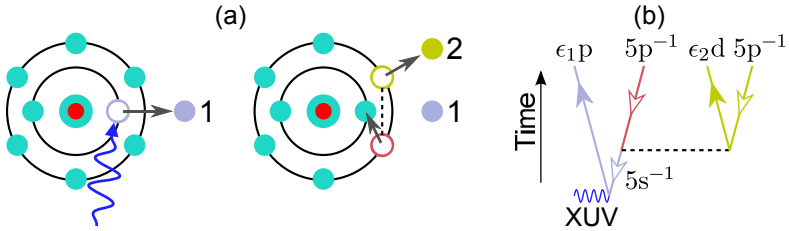

Figure 5.7: **Conjugate shake-off.** (a) Cartoon illustrating the Auger-like filling of the primary hole in the 5s subshell and Coulomb interaction (dashed line) to transfer energy to the secondary electron. (b) The corresponding Feynman-like diagram. For a pedagogical introduction to Feynman diagrams, see Ref. [158].

shake-off and knockout [9], two different delays will be presented. By combining τ_{cc} from the supplement of Paper **I** with the calculated single ionization time reference [154] the measurement can be converted into absolute one-photon group delays of $\tau_{DI}^{1ph} \approx 485$ as within the shake-off model or 535 as for knockout. Direct calculations of one-photon group delays from theory gave 510 as (shake-off) or 485 as (knock-out), which are consistent within one experimental standard deviation in both cases but closer for shake-off. A wider comparison between experimental and theoretical delay maps (Figure 4 of Paper **I**) in areas where direct DI is expected to dominate, also hints towards the shake-off mechanism more than the knockout.

Both mechanisms of direct DI are thought to co-exist, so a weighted average of the two delay calculations would be expected in the experiment. In helium it is well known that knockout is limited to low photon energies while normal shake-off (approximating photoionization as sudden) dominates at high photon energies [9]. The many electrons of xenon do however allow other mechanisms than in helium. As pointed out for shake-up earlier, *conjugate* shake remains strong at low energies and is enabled by electron correlation (for instance in the initial state) [36, 37]. Since the dominant nd Rydberg states in xenon were produced by conjugate shake-up, it is by extension to the continuum natural that we perform the calculation for conjugated shake-off with an ϵ_2d secondary electron. In Fig. 5.7, the conjugate shake-off process is seen to start with photoionization of a 5s rather than 5p electron (or 5s term in the mixed initial state). The hole (i.e. the electrons remaining in the ion) then interacts and rearranges to the final 5p^{-2} double hole and the secondary ϵ_2d continuum electron.[13] This rearrangement and Feynman diagram is identical to the Auger effect, but here occurs within the $n = 5$ shell and presumably faster. The time delay we measure relates to propagation in the final state, not the Auger-like lifetime.

In conclusion, we have demonstrated that the combination of coincidence spectroscopy and interferometry gives both the electron-pair intensity and a group delay related to its scattering phase. Together they give complementary information about the transition matrix elements of one-photon direct double ionization.

[13] The calculation for knockout starts with photoionization of 5p and assumes the final continuum state is ϵ_1d ϵ_2f. See the supplement of Paper **I**.

5.1.2 Plasmon resonance in photoionization of C_{60}

The connection between scattering phase (η) and angular distribution (characterized by β) of the emitted electron is well known for atoms, as introduced in section 2.3.2. In attosecond metrology, the derivative of η is manifested in the group delay of the photoelectron ($\tau_{\mathrm{SI}}^{1\mathrm{ph}}$) [63]. For molecules and condensed matter, connections between these quantities have not been explored as much, although the existence is not unexpected. In Paper **II**, synchrotron radiation is used to study β and verify a new formulation of the connection between β and $\tau_{\mathrm{SI}}^{1\mathrm{ph}}$, for the C_{60} molecule. The nearly spherical (icosahedral) symmetry of this molecule [159] means that the angular theory for atomic systems can be applied with minor modifications.

Another motivation for studying C_{60} [159] is that its 240 valence electrons constitute a very large system of correlated electrons. This nearly macroscopic oscillation, can essentially be treated classically. When local effects (e.g. within 0.1 nm) are not of importance, the phenomenon can be described as a mode of oscillation in electron density (and electric field), called a *plasmon*, rather than via individual electron coordinates. Surface plasmons are of particular interest in nanometre structures where applications and outlooks range from chemical sensors [160, 161] to faster information technology by combining photonics and electronics as plasmonics [162, 163]. Regardless of applications, there is a fundamental interest to explore the borderline between quantum and classical mechanics by studying systems ranging from small to large and from weakly to strongly bound [164]. In this context C_{60} with a diameter of 0.7 nm is smaller than engineered nanoparticles and bound much more strongly than van-der-Waals clusters of atoms. Efforts are currently being made to study the dynamical aspects of plasmons in nanostructures with attosecond light sources [165, and references therein].

Plasma oscillation and polarizability

The cage of carbon atoms, illustrated in Fig. 5.8(a), has the hexagonal faces characteristic of fullerenes but also pentagons to obtain the curvature, like a soccer ball. In an elementary description of the valence orbitals, the four 2s and 2p electrons of each carbon atom form sp^2 hybrid orbitals [35, 166], of which three make σ-bonds along the surface (lines in the figure). The fourth orbital (π-bond) has nonzero electron density just outside and inside the cage. Without distinguishing orbitals, a net electron density can be defined (blue cloud in (b)). This is done in the so-called jellium model [167, 168] and the cage is approximated by a shell of positive charge (red ring). A simpler treatment of the electrons as a classical medium, conducting or liquid, confined within a thick spherical shell is also possible [169]. Those models are similar to Mie scattering theory [170, 171] which was initially developed for solid spheres.

When an external electric field is applied, for instance within a pulse of light, the electrons are displaced as illustrated in Fig. 5.8(c) for vertically polarized light. Since the nuclei are nearly stationary at the timescale of electronic motion, a separation between positive and negative charges is created – formally a plasma. The change in charge density induces a molecular dipole moment (of complex amplitude

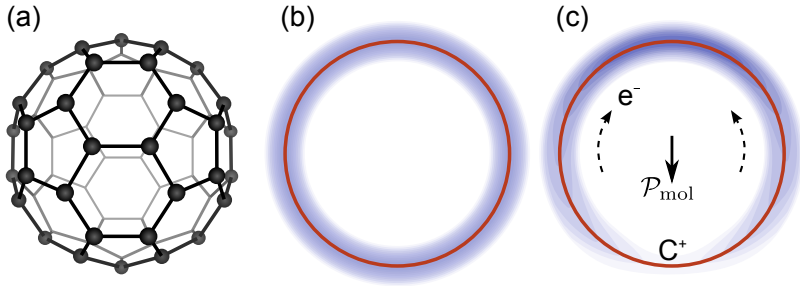

Figure 5.8: **C_{60} and the surface plasmon.** (a) Geometry of C_{60} with carbon atoms marked on the front half. (b) Electron density (blue cloud) at equilibrium and ion density (red circle) in the spherical jellium model. (c) Electron density redistributed during the oscillation of the plasmon (or driven by an external field). The induced dipole moment ($\mathrm{Re}[\mathcal{P}_{\mathrm{mol}}e^{-i\omega t}]$ at time t) points down at this instant.

$\mathcal{P}_{\mathrm{mol}}$). Typically there are dampening forces within the molecule, and eventually the light field changes sign, so the electron displacement and charge density will oscillate around the equilibrium: a plasma oscillation or plasmon for short. The magnitude and phase of the induced dipole are determined by the complex *polarizability*, α, defined by $\mathcal{P}_{\mathrm{mol}}(\omega) = \alpha(\omega)\mathcal{E}(\omega)$ where $\mathcal{E}(\omega)$ is the complex amplitude of the external field at angular frequency ω [35]. The polarizability theory underlies for instance the classical description of Raman scattering [172] but is still studied in new ways with attosecond pulses [155].

The same kind of relation, between external field and polarization density is written $\mathcal{P}(\omega) = \chi(\omega)\varepsilon_0\mathcal{E}(\omega) = (\varepsilon_{\mathrm{r}}(\omega) - 1)\varepsilon_0\mathcal{E}(\omega)$ for macroscopic dielectric media, with the susceptibility χ or relative permittivity ε_{r} [50, 173]. ε_0 is the electric constant. In dilute samples, e.g. evaporated into a vacuum chamber, the macroscopic and microscopic parameters are linked by $\chi\varepsilon_0 \approx \alpha N$, where N is the number density of molecules[14]. Thus α, χ and ε_{r} are three ways to quantify the linear frequency-response of a sample to light. For dispersive media these quantities are frequency dependent and complex-valued. The refractive index of the medium is $n_{\mathrm{r}} \approx \sqrt{\mathrm{Re}\,\varepsilon_{\mathrm{r}}}$ and the absorption coefficient $a \approx -\frac{\omega}{c_0 n_{\mathrm{r}}}\mathrm{Im}\,\varepsilon_{\mathrm{r}}$ (in the case of weak absorption) where c_0 is the speed of light in vacuum [50, 173]. By absorption spectroscopy, the imaginary part of $\varepsilon_{\mathrm{r}}(\omega)$ (and $\alpha(\omega)$) are possible to determine but the real part is not accessible from the spectrum[15]. In general, the magnitude of the frequency response tends towards zero (1 for ε_{r}) when $\omega \to \infty$; not even electrons respond instantaneously. More interestingly, there can be resonances with particularly large magnitudes at frequencies specific to the sample. Upon crossing a resonance, the real part of the frequency response changes sign, i.e. the induced dipole goes from being in phase with the driving field to being in anti-phase.

[14] In a dense medium, $\mathcal{E}$ is altered locally by the dipoles of the surrounding molecules so that the Clausius–Mossotti relation $\alpha N = 3\varepsilon_0\chi/(\chi+3) = 3\varepsilon_0\frac{\varepsilon_{\mathrm{r}}-1}{\varepsilon_{\mathrm{r}}+2}$ should be used instead [35, 174].

[15] If the imaginary part is known for *all* ω, the Kramers–Kronig-relation gives the real part [50].

In C_{60}, the first surface plasmon resonance, illustrated in Fig. 5.8(c), lies at a photon energy of 20 eV [169, 171, 175]. It can be understood as electron motion between opposing hemispheres. The figure depicts an instant where electron density is relocated from the bottom to the top half of the cage, effectively along the polarization axis. Near 40 eV there is another oscillation mode, having charge density with the opposite phase inside and outside the cage or alternatively represented as electron motion through the cage (up and down locally, not relocating to the other hemisphere) [167, 169]. The contribution from electrons in π-bonds dominates in the 20 eV plasmon [167, 176] but all 240 valence electrons are active in the calculation. The period time of the oscillation is the same as the period of the exciting optical field, 21 as for 20 eV photons. The 20 eV plasmon is located well above the 7.6 eV single ionization threshold, a rather special situation that allows the plasmon excitation to decay by autoionization with a lifetime of only about a femtosecond (estimated from the spectral width). It is well known from the work of Fano that autoionization or direct photoionization quantum paths interfere to affect the photoelectron spectrum [38]. In the present study, the influence of the collective oscillation on the direct photoionization is considered, not via interference of quantum paths but via the (not quantized) electric field that acts on the electron.

Methods

C_{60} molecules were evaporated from an oven in vacuum to intersect the beam of light at beamline I3 at MAX III, offering photon energies from 5 to 50 eV. We scanned the photon energy around the 20 eV resonance (from 17 to 22 eV) while imaging the momentum of electrons with a 2D velocity map imaging spectrometer (then Abel-inverted to 3D in software). For electron energies corresponding to the two lowest final state configurations of C_{60}^+ the angular anisotropy parameter $\beta(\omega)$ was examined.

Time-dependent density functional theory calculations in the local-density approximation (TDLDA) [167, 168, 170, 176] were used by my co-authors to model $\alpha(\omega)$, or more precisely the electric screening potential corresponding to the induced electric field $\mathcal{P}_{\mathrm{mol}}/\varepsilon_0$. The nearly spherical symmetry also allowed an approximation using the familiar analytic theory for atomic systems (eq. (2.2) in section 2.3.2). As a first step a connection between α and the scattering phase was defined by a classical propagation through the oscillating potential. From the scattering phase then both β [51, 53, 61] and a Wigner-like group delay $\tau_{\mathrm{SI}}^{\mathrm{1ph}}$ [63] can be obtained. What we analyse is the *relative* scattering phase and group delay, referenced not against a Coulomb potential but against the C_{60} potential without plasmon (here obtained from the TDLDA).

Result

With 20 eV photon energy, ionization from the highest occupied molecular orbital (HOMO) or HOMO−1 leads to electrons of 12.4 or 11.1 eV kinetic energy (Figure 1 in Paper **II**). The angular distribution for electrons below 8 eV is isotropic regardless of photon energy, but for HOMO and HOMO−1 (both of π character) the anisotropy

$\beta(\omega)$ goes through a minimum at the resonance. The minimum of $\beta \approx 0.7$ at 20 eV and the off-resonance anisotropies ($1 \leq \beta \leq 1.6$) can be reproduced by both the TDLDA and the analytical model. The relative scattering phase in the model is converted to group delay and we find that the plasmon increases or reduces the group delay of the departing electron, depending on whether the frequency of the light is above or below the resonance. Such a sign-change is expected because of the earlier mentioned sign-change of the frequency response when crossing a resonance, thus the electron is either released at an elevated or reduced potential energy compared to the case without plasmon contribution to the field. The group delay varies about 100 as for HOMO−1 and 70 as for HOMO.

The method demonstrated in Paper **II** should be applicable also to metallic or dielectric nanoparticles and large clusters, if the plasmon is autoionizing so that photoelectrons are produced at the resonant photon energy. It provides both the real and imaginary parts of the polarizability from a (2D) measurement on a finite spectral interval and a model calculation, which may be simpler than obtaining a wide-range spectrum for Kramers–Kronig analysis [174] or measuring the refractive index of a dilute sample. This method of assessing the plasmon's contribution to electron group delay with monochromatic light rather than broadband attosecond light pulses can be advantageous for samples with dense spectra.

5.2 Femtosecond dynamics in molecules

Chemical reaction involves the motion of nuclei. In the Born–Oppenheimer picture it is driven towards minimization of the energy of the electronic state. Industrial and biological chemistry often takes place in liquid solvents that prevent direct access to the kinematics of the products, and can involve very complicated molecules. In this thesis, photochemical reactions are studied for molecules consisting of a few atoms in the gas-phase where momentum vectors of the products can be measured for reactions that lead to ionization and dissociation. The rather direct and complete measurement, free from environmental disturbances, is a good model system for exploring basic molecular dynamics. The accessible dynamics concerns connections between electronic states, geometric changes and fragmentation. An improved understanding of these fundamentals can be useful also for the analysis of larger chemical systems. Dissociation channels where the molecule bends to form a new bond between some atoms before dissociation are particularly interesting since new species or radicals can be formed. We concentrate on fast reactions, where the complex coupling between nuclei and electrons may occur and affect the reaction path.

As introduced in section 2.4, the evolution of a photoreaction can be investigated via snapshots by a probe pulse sent at different instants or via autoionization of a molecule which has been core-excited. Section 5.2.1 summarises results from core-excited molecules in Papers **III**–**IV** and section 5.2.2 presents a pump–probe experiment.

When probing by (sequential) photoionization, the delay of the probe pulse is a parameter and thus any observable is directly related to temporal evolution of the molecule. The parameter is sometimes seen as a control knob for influencing the reaction path [177, 178], i.e. an interest in selecting final state (selective bond breaking [179] or charge localization [180]) rather than understanding the intermediate state. Femtosecond precision in the delay between pump and probe pulses has long been available with lasers [23, 69, 70], but the low photon energy available puts constraints on what samples can be excited or ionized in a spectrally selective way, typically by multi-photon absorption or using filtered high harmonics. Ionization by a strong laser field or attosecond pulses are used in different applications to access the shortest time scales, hitherto concentrated to atoms or diatomic molecules to minimize the density of states. The tunable and higher photon energy of free-electron lasers offers an attractive combination of spectral selectivity and femtosecond time resolution [29].

The method of probing by autoionization (typically resonant Auger) relies more heavily on a complete characterization of the photofragment momenta to understand the dynamics. Kinetic energies of electrons [17, 18] or ions [60, 115] can sometimes be related to at what stage during a dissociation reaction an Auger decay occurred, and thus set the reaction on a qualitative time scale. Measuring both types of fragments is of course ideal [40–42] but a quite good understanding of the kinematics can be reached by analysing the 3D momentum vectors of two or three ions from a small molecule, detected in coincidence. While the time range probed is set by the Auger lifetime, the soft x-ray photon energy of a synchrotron can be tuned to different core-excited states (e.g. an 1s electron from C or O promoted to the lowest unoccupied

molecular orbital). This element and site selectivity can allow measurements with different Auger lifetimes (control of the "probe" delay) and control of the branching ratio between fragmentation paths with different localization of the charge [58]. The core-excited states can explore non-Franck–Condon geometries by decaying to cation or dication states that are not reachable by vertical photoexcitation or direct ionization.

For dissociation that occurs much faster than rotation, the axial recoil approximation allows the anisotropy parameter β of fragments to be analysed as introduced in section 2.3.1. The absorption cross section favours transition dipole moments along the polarization vector and introduces an alignment of excited molecules. Anisotropy ($\beta \neq 0$) in the distribution of fragments reveals that dissociation occurred faster than rotation of the molecule. The value of β may further tell whether fragments were mostly emitted along or perpendicularly to the transition dipole moment, with the respective rotation-free limits of $\beta = 2$ and -1. Neglecting rotation, β may also be converted to bond angle for a bent molecule, at least in the C_{2v} symmetry group of water.

5.2.1 Core-excited tri-atomic molecules

Molecules with three atoms are the simplest systems where bending and more than one mode of vibration can occur. Everyday molecules such as water (104° bond angle, point symmetry group C_{2v}) and carbon dioxide (linear, $D_{\infty h}$) offer sufficient complexity to repeatedly be re-investigated in various ways. In the work presented here, the resonant absorption of a soft x-ray photon prepares a neutral molecule with a 1s hole and one electron in a normally unoccupied molecular orbital. In a diagram of potential energy curves, such as Fig. 5.9, the electronic transition is vertical (faster than nuclear motion) and typically leads to a core-excited molecule that is not at its equilibrium geometry. This sets the nuclei in motion, here expanding the A–BC bond in a generic ABC molecule. Depending on when an Auger decay occurs, different final states or reaction paths may be reachable. The left part of the figure illustrates that core-excited states within the Franck–Condon region have distinct peaks in the absorption spectrum, allowing tuning of the photon energy to selectively populate a particular state (only one is shown, ABC^*). Core-excited states are well above the dissociation and ionization energies of all constituent atoms, so fragmentation into three atomic ions is possible but the most common reaction is often double ionization with either a diatomic fragment or a third neutral fragment.

The kinetic energy of the fragments can be related to the speed of the dissociation. The photo-excitation in Fig. 5.9 is followed by double autoionization. The kinetic energies of the two emitted electrons are represented by the downwards arrows labelled e_1^- and e_2^-. We study the dissociation of molecules into at least two charged fragments by measuring the 3D momenta of the ions, i.e. the emission angle and kinetic energy. For short-lived excited states, the kinetic energy release is given by at what point the dissociative final state (ABC^{2+}, red curve) is reached. Ionization at a short distance typically gives a strong repulsion, high kinetic energy and a rapid dissociation without much time for bending or other deformations. Later decay of the electronic

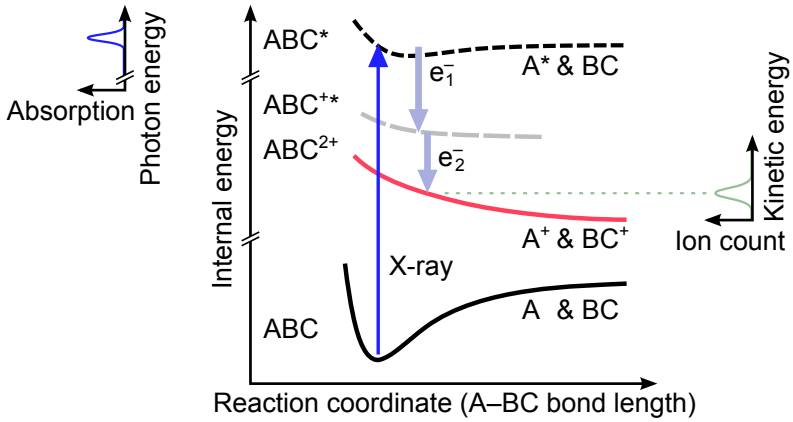

Figure 5.9: **Nuclear motion leading to dissociation in the dication.** This extends Fig. 2.6(b) to a photoreaction with double autoionization from a neutral core-excited state (ABC^*). It is here assumed that Auger decay leads to an excited, short-lived or bound, cation (ABC^{+*}) so that the main part of the kinetic energy is released in the final state (ABC^{2+}) during dissociation.

state, at a larger bond length, leads to slower ions where the shape of the potential energy surface can play a role in steering the reaction through vibrating and bending modes. If a substantial amount of kinetic energy is released along more than one of the potential-energy curves, a precise assignment may require access to the electron energies but the basic correlation between energy and speed of dissociation remains. Thus, within each dissociation channel (events producing the same set of fragments), the events that yield a high total kinetic energy of the fragments give more accurate information about bond angles in the (neutral) intermediate state while low-energy events can bend and reach and more exotic fragmentation paths. The internal energy of the fragments (electronic or vibrational) has been neglected here. A large part of Paper **IV** concerns the observed reduction or increase in angle between fragments at low kinetic energies in different channels.

The data set of coincident ion momenta can be analysed in many ways beyond determining the total kinetic energy release. For the assignment of dissociation processes we have analysed the energy correlation between three fragments using *Dalitz plots*. A Dalitz plot shows barycentric coordinates of squared momentum, $\pi_i = |\vec{p}_i|^2 / \sum_j |\vec{p}_j|^2$ where $\vec{p}_i$ is the momentum vector of fragment i [181–183] The normalization to $\sum_i \pi_i = 1$ removes one degree of freedom, so for three fragments the barycentric coordinates span the two-dimensional interior of a triangle. Physically, momentum conservation further constrains the coordinates to an inscribed circle with $0 \leq \pi_i \leq 2/3$ as shown in Fig. 5.10(a). If dissociation occurs simultaneously (concerted) along both bonds, there is no further constraint and (b) shows intensity over most of the circle for a core-excited water molecule (O $1s^{-1}\,4a_1$). The neutral fragment (hydrogen) is not detectable but if all other fragments are detected it is given by momentum

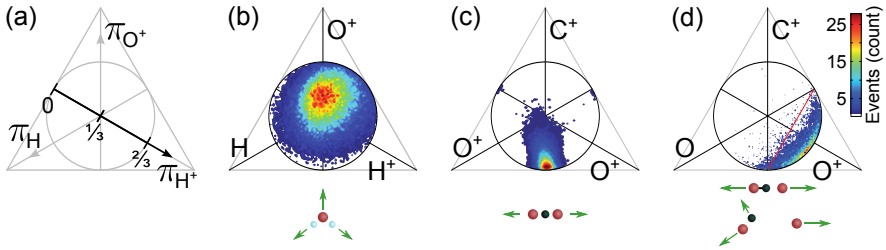

Figure 5.10: **Dalitz plots and the signatures of different dissociation processes.** (a) The barycentric squared momentum coordinate π_i for fragment i points towards its corner of the triangle and is zero on the opposite side, here shown for H^+. (b) Concerted dissociation of H_2O along both bonds gives a broad, nearly centred distribution for a bent molecule but (c) no momentum for the middle C^+ fragment from a linear CO_2 (OCO) molecule. (d) Sequential dissociation gives a narrow distribution perpendicular to the coordinate of the first fragment, here O^+. When the bond within CO^+ breaks at a later stage, momentum conservation in its rest frame imposes a strong anti-correlation between the absolute momenta of the C^+ and O.

conservation. A symmetric, concerted dissociation of a linear molecule is shown in (c) for triple-ionization of CO_2. The intensity is concentrated in the point where the central carbon remains at rest ($\pi_{C+} = 0$) while the oxygen ions depart with equal speed in opposite directions. When CO_2 bends in the core-excited state, as shown in Paper **III**, intensity spreads to the rest of the Dalitz plot – approaching the case in (b). A third variant that has a distinct signature in the Dalitz plot is sequential dissociation where one bond is broken before the other. Figure 5.10(d), for non-resonant ionization of CO_2 at 60 eV photon energy, can be interpreted as $(OCO)^{2+} \rightarrow O^+ + (CO)^+ \rightarrow O^+ + C^+ + O$. Conservation of momentum between the C^+ and O fragments of the second dissociation, occurring within the rest frame of $(CO)^+$, gives a strong anti-correlation between π_{C+} and π_O while correlation with the initial π_{O^+} is almost lost. The result is a nearly one-dimensional stripe in the Dalitz plot at a constant π_{O^+}.

Renner-Teller effect in CO_2

Paper **III** explores the dynamics following resonant photoexcitation of an 1s electron in carbon dioxide to the lowest unoccupied molecular orbital (LUMO) $2\pi_u$. Sketches of the CO_2 orbitals as linear combinations of atomic orbitals are shown in Fig. 5.11. With the core hole in carbon the C $1s^{-1}2\pi_u$ resonance occurs at a photon energy of 291 eV and with an oxygen hole O $1s^{-1}2\pi_u$ is located at 535 eV – as seen in the ion yield spectra in Fig. 5.12. To clarify that these are states in the neutral molecule, O $1s^{-1}$-excited Rydberg series converging to the C $1s^{-1}$ or O $1s^{-1}$ ionization energies are also labelled [184, 185]. The ground state of dissociated $O^+ + CO^+$ lies at 33 eV and can be reached via vertical ionization to CO_2^{2+} around 38 eV [43]. From the core-

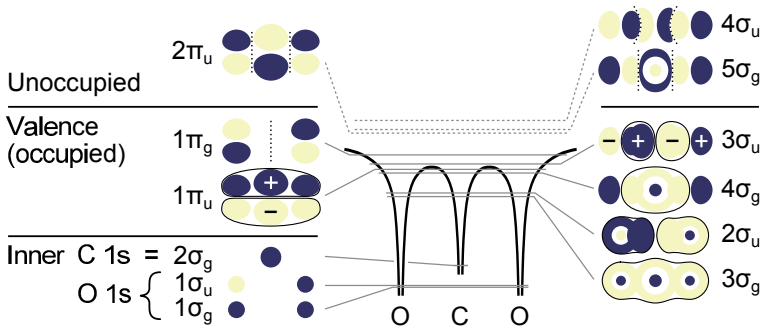

Figure 5.11: **Molecular orbitals in carbon dioxide.** While the 1s-subshell is localized in each atom, atomic valence orbitals mix constructively (solid contours) or destructively (dashed nodes) and form bonding or antibonding molecular orbitals [186]. Energies and the sketched electric potential are not to scale.

excited states, autoionization (including at least one Auger decay) can give double as well as triple ionization. Energetically, dissociation along any or both bonds is possible and the purpose of the experiment is to find which dissociation channels actually occur, which together with theory about the potential energy surfaces and autoionization lifetimes can elucidate the dynamics. The principle of using autoionization rather than a probe pulse to analyse a photoreaction was introduced in section 2.4 and in our case both kinetic energy and angular correlation between the fragments is observable.

The Renner–Teller effect arises when a state is degenerate with respect to bending. Renner was perhaps the first to analyse the splitting of an energy level due to bending, i.e. a coupling between nuclear and electronic motion [188, 189]. Jahn & Teller discussed this kind of splitting more generally and proved that molecules with a degenerate ground state will deform and break the nominal symmetry [190]. The

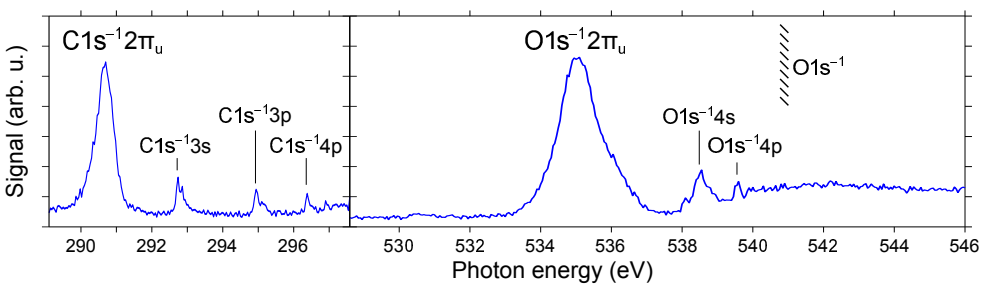

Figure 5.12: **Near-edge x-ray absorption fine structure in CO_2.** The short Auger lifetimes (6 and 3.5 fs) and consequently unresolved vibrational structure gives wide peaks for the carbon (left) and oxygen (right) $1s^{-1}\pi_u$ compared to Rydberg states.

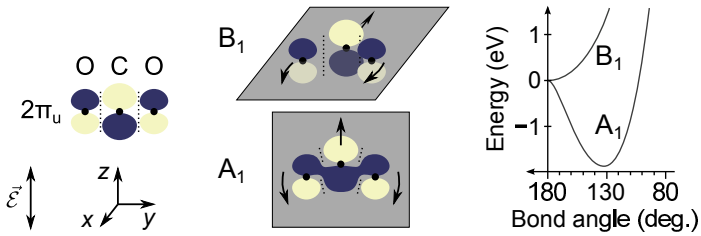

Figure 5.13: **The Renner–Teller effect.** The transition dipole moment from 1s to the $2\pi_u$ orbital favours polarization, $\vec{\mathcal{E}}$, along the axis denoted z here. Bending of the molecule in the xy or yz plane increases (B_1) or reduces (A_1) the energy of the electronic state (curves from Ref. [187]).

only exception is linear molecules, where degenerate states can be stable. CO_2 is linear in both its neutral and cationic ground state. In the neutral core-excited $1s^{-1}2\pi_u$ state, the linear geometry with a total symmetry of $^1\Pi_u$ is however unstable[1]. To understand this, recall that mirroring a Π_u state in one plane containing the molecular axis changes the sign of the wavefunction while mirroring it in the perpendicular plane (also containing the axis) does not [35]. Due to the rotation symmetry of the linear molecule there is no way to distinguish the two planes and the Π_u state becomes degenerate. The transition dipole moment for the core-excitation leads to a preferred alignment with the molecular axis perpendicular to the polarization of the light ($\Sigma \rightarrow \Pi$ transition in Fig. 2.3(b)). With respect to the $2\pi_u$ orbital, shown again in Fig. 5.13, this corresponds to vertical polarization. Denoting the polarization axis as z and the molecular axis as y, two distinct planes of bending can now be defined while maintaining the π_u-orbitals along z. Bending of the molecule in the xy-plane gives a state of the B_1 symmetry label while bending in the yz-plane corresponds to A_1. For B_1, the linear geometry with a 180° bond angle gives the equilibrium while for A_1 a 2 eV lower energy is reached at about 130° [187]. Thus the degenerate Π_u is split into states of higher and lower energy when bent, shown by the Walsh diagram at the right-hand side of Fig. 5.13. Visually this can be interpreted in the middle part of the figure as non-zero electron density appearing in the C–O bonds in the A_1 geometry while the antibonding character remains for B_1. Looking at the pattern of same-sign (e.g. dark) parts for other orbitals in Fig. 5.11 it is clear that no other orbital than $2\pi_u$ has the necessary symmetry.

In the Born–Oppenheimer approximation, electronic excitation occurs without change in nuclear coordinates – "vertically" between the potential energy curves. From the curves in Fig. 5.13, the 180° bond angle of the ground state is incompatible with excitation to the A_1 equilibrium, and Franck–Condon overlap requires a simultaneous bending vibrational excitation in A_1 (vibrational quantum number $v \approx 11$ [191]). By detuning to the low-energy side of the resonance, population of B_1 is prevented and in a classical picture one would think bending occurs simultaneously

[1] Since a 1s-hole does not affect bonding much, core-excited CO_2^* is often compared to the ground state of NO_2, which is bent.

with the electronic transition, invalidating the Born–Oppenheimer approximation. Because of this, the Renner–Teller effect in CO_2 is a well-studied model system for vibrational–electronic coupling [59, 185, 192]. Our study in Paper **III** is not the first with coincident detection of the fragment momenta, but the use of Dalitz plots strengthens the identification of dissociation processes. We compare plots for different kinetic energy ranges and for channels where two or three ions were detected. The latter also allows a calibration for the effect of aborted coincidences, where triple ionization occurs but the limited detection efficiency for coincident fragments of the same mass leaves one O^+ ion undetected yields a false contribution to the double-ionization analysis.

We find fragment angles extending down to 20° and a clear signal for the extreme bending result where an O_2^+ fragment is produced in coincidence with C^+. Judging by the angular anisotropy (β-parameter) the folding of the terminal oxygen atoms into an oxygen molecule is much faster than rotation. The anisotropy is comparable to previous observations of proton migration in acetylene (ethyne, HCCH) forming C_2^++H_2^+ [193]. With oxygen being much heavier than protons, a time scale similar to OCS where only a small anisotropy was found for C_2^++OS^+ [194] would seem likely. Since the C^++O_2^+ pair is absent in direct ionization we conclude that the bending initiated by the Renner–Teller effect is the cause of the rapid oxygen migration. The importance of motion in the core-excited state is further supported by the fact that the branching ratio of C^++O_2^+ in relation to other channels is doubled for C $1s^{-1}2\pi_u$ which has twice the Auger lifetime of the O $1s^{-1}2\pi_u$ (6 and 3.5 fs, respectively).

Correlation between potential energy and bond angle for H_2O

For an Auger transition in water, excitation of the oxygen 1s electron is the only option. As Fig. 5.14 shows, the electron can be promoted to molecular orbitals of different symmetry (e.g. $4a_1$ and $2b_2$ [35]) and any difference in the resulting dynamics examined [18]. The $1s^{-1}2b_2$ lies 2 eV higher in the Franck–Condon region and is not immediately dissociative, having a potential energy well with a depth of at least 5 eV [195].

The neutral water molecule is bent in its ground state and the bond-rearrangement channel O^++H_2^+ has been observed in the inner-valence region. In Paper **IV** we analyse the correlation between kinetic energy and bond angle in the three-body breakup H+O^++H^+ and find that smaller bond angles occur for lower energies. An assignment using literature energies for states in the dication H_2O^{2+} and the relevant fragment final states suggests that three-body breakup and the complete bond rearrangement are competing (perhaps following the same initial reaction path) and that low internal energy of H_2O^{2+} leads to bond rearrangement while dissociation occurs without complete bending for higher energies. Analogously to Fig. 5.9, the internal energy of H_2O^{2+} corresponds to the kinetic energy released during dissociation.

The very lowest states of H_2O^{2+} dissociate by breaking only one bond, leading to H^++OH^+. The angle between these fragments closely matches the neutral 104° except on the low-kinetic energy side of the distribution when the initial excitation was to $2b_2$, where the angle is increased. One may speculate that a wave packet in

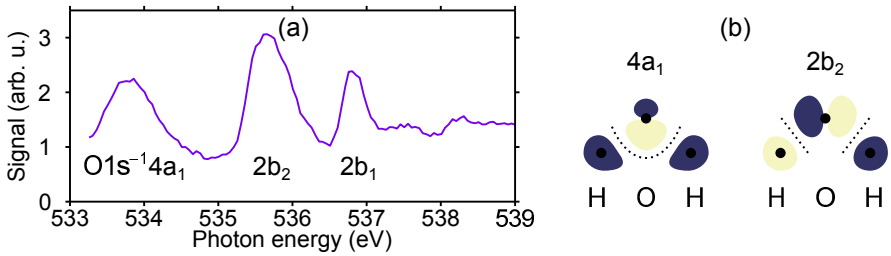

Figure 5.14: **Core-excited water**. (a) Near-edge x-ray absorption fine structure in H_2O, calibrated to Ref. [18] in energy. (b) Sketches of the antibonding $4a_1$ and $2b_2$ molecular orbitals.

this non-dissociative excited state explores a wider range of angles before the Auger decay lets it dissociate. This may give access to linear (180°) states in H_2O^{2+} that lie below the bent ones but can not be reached by a vertical transition from the neutral. An assignment using linear states matches the observed low-energy cut-off of the kinetic energy release.

5.2.2 Pump–probe study of the dissociation of acetylene

The motion of nuclei in chemical reactions often occurs over time intervals of femtoseconds or picoseconds. Short-range nuclear motion around local energetic minima can be rationalized using vibrational and bending modes but isomerization to other equilibria also occurs, in organic molecules often as proton migration. Such isomerization processes are often associated with functionality in biological processes.

Ultra-fast proton migration has attracted much attention, currently progressing by studies of small cationic hydrocarbons in pump–probe schemes using low or high harmonics of laser pulses (XUV pump, IR probe) [45, 196] or using free-electron lasers (XUV pump, XUV probe) [46, 197]. Non-radiative energy conversion mechanisms such as intramolecular vibrational relaxation (IVR) have been investigated on the femtosecond time scale in neutral organic molecules [70] and recent free-electron laser studies of acetylene provide experimental evidence for the IVR process as an efficient energy-redistribution mechanism. Being among the smallest hydrocarbons, acetylene (ethyne, C_2H_2) is a widely studied model system for proton migration. From bent configurations the vinylidene isomer, with both protons bonded to a single carbon, is accessible, and it is the dominant channel for decay from the first excited state in the acetylene cation.

In the ground state of both the neutral and cationic species acetylene is linear and the term symbols for the $D_{\infty h}$ symmetry are used. In the following description of electronic states of the cation, the linear geometry is assumed unless otherwise stated. Upon photoionization by a comb of XUV high-harmonics ranging from 20 to 40 eV, cations are prepared in the ground state $X\ ^2\Pi_u$ (vertical ionization energy 11.4 eV) and the first three excited electronic states: $A\ ^2\Sigma_g^+$ (16.7 eV), $B\ ^2\Sigma_u^+$ (18.5 eV) and $C\ ^2\Sigma_g^+$ (23.5 eV) [178, 198–200]. The differences in equilibrium geometries in these states compared to the ground state leads to the excitation of many vibrational modes. This is seen clearly when the photoelectron spectrum obtained with 40 eV synchrotron radiation [199] in Fig. 5.15(a) is compared to the adiabatic energy level diagram in (b).

Electronically excited states may undergo ultra-fast isomerization or dissociation, often violating the Born–Oppenheimer approximation.

- A long-standing debate on whether the A state decays by proton migration to vinylidene [206] or by conical intersections to the ground state [210] was recently resolved by a unified theoretical treatment. Time scales of 60 fs for isomerization (matching free-electron laser experiments [46, 197]) and about 250 fs for vibronic coupling were found [211, 212]. Vibrationally excited A-states can pre-dissociate [35, 57] towards $H + C_2H^+$, with the appearance energy 17.35 eV [203, 213].
- The B state has a shorter lifetime, about 14 fs, with the proposed decay mechanisms being vibronic coupling to A or X in a bent geometry and spin-orbit coupling to repulsive states [201, 213]. Onsets in partial ion yield spectra reveal that it dissociates both to the first limit and to $H^+ + C_2H$, at 18.9 eV [213, 214].
- The dynamics of the high-lying C state is much less understood but it is known to be predissociative [200, 202]. For dissociation by breaking of the C–H bond it

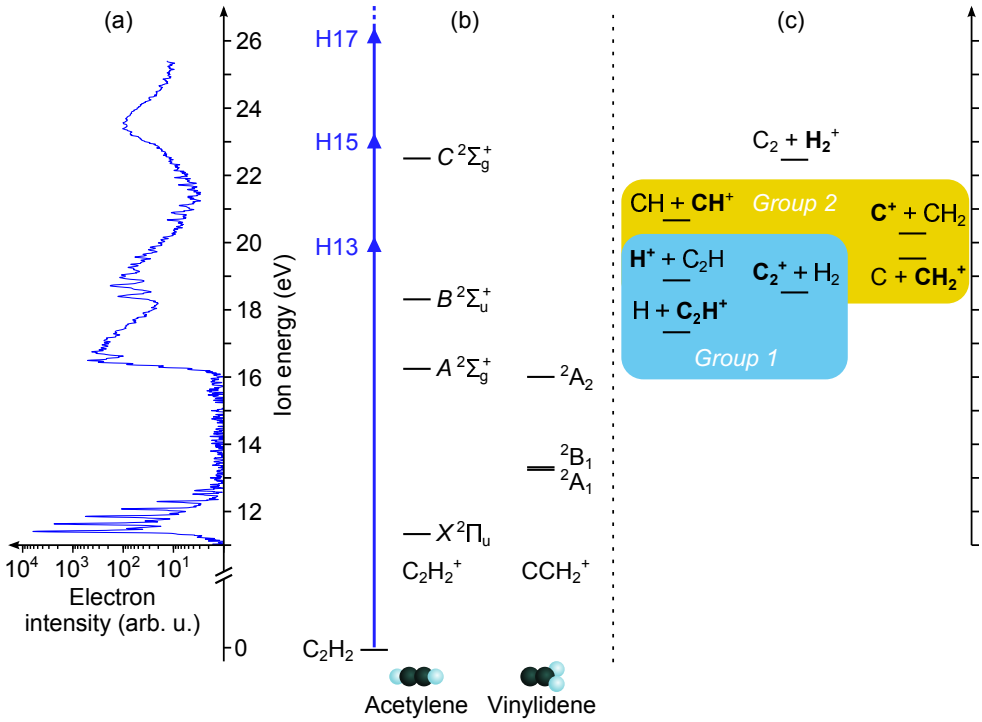

Figure 5.15: **Electronic states of the acetylene cation and fragment appearance energies.** (a) Photoelectron spectrum with 40 eV photon energy, provided by S. Canton [199]. (b) Electronic states of the cation in the acetylene and vinylidene isomers. Adiabatic ionization energies are given relative the neutral acetylene ground state [201] (estimated for $C\ ^2\Sigma_g^+$ [200, 202]). (c) Dissociation limits resulting from the breaking of one bond, with fragments in their ground states [202–207]. (Some excited states can be found in Refs. [202, 208, 209].) For the three lowest dissociation limits (Group 1) the C–C bond remains intact while it is broken in the next three (Group 2). The topmost limit, producing H_2^+ will not be analysed. The energy axis is repeated on the right to aid the readout.

seems to favour $H^+ + C_2H$ over $H + C_2H^+$ [214]. Breaking the C–C bond leads to $CH + CH^+$, probably with CH^+ in an excited state [202].

- The presence of one or more states in the 21 eV region, between B and C, has been discussed and the spectrum shown in Figure 5.15(a) clearly resolves vibrational structure in this region although the intensity is low. The first appearance energies for $CH + CH^+$ (20.8 eV) and $C^+ + CH_2$ (21.2 eV) have been reported in this range. The latter channel requires isomerization to vinylidene [202, 204, 213].

Two-hole one-particle states were found at energies above the C state but will not be considered here.

Dynamics in the acetylene cation will be presented here, based on a preliminary analysis of mass spectra from XUV pump – IR probe experiments. The dissociation limits in Fig. 5.15(c) have been grouped by energy into Group 1 (the three lowest) and Group 2 (breaking the C–C bond) we present the fragments produced at these limits in the following and show that these exhibit dynamics on different time scales.

Experimental methods

The XUV pump pulse consists of high harmonics, generated in krypton at 9×10^{-4} mbar (1 mbar = 100 Pa).[2] Harmonics below 20 eV are blocked by an aluminium filter while higher orders are present up to about 40 eV. The photon energies of harmonics 13 to 17 are marked as arrow-heads on the blue line in Fig. 5.15. We checked that no signal from correlated ionic pairs (double ionization fragments) is observed but a small amount of $C_2H_2^{2+}$ is expected at the same time-of-flight as CH^+ (mass/charge ratio of 13 u/e). The double ionization threshold is 32 eV but even with 38 eV photons single ionization has been reported dominant [46]. To measure the evolution of the cationic states, an infrared pulse of 1.5 eV photon energy, 30–35 fs duration (FWHM) is used as probe for the time-resolved experiment. The intensity of the probe pulse is high enough that multi photon processes may take place but our analysis indicates that these are generally unlikely.

Mass spectra are recorded in an electrostatic spectrometer with a position sensitive detector (Fig. 4.8). The harmonic-generation beamline limited the spectrometer background pressure to 2×10^{-8} mbar. Acetylene was injected at room temperature via an effusive jet to pressures of $2–8 \times 10^{-7}$ mbar in the different scans. Mass spectra resulting from ionization by the pump or probe pulse are shown in Fig. 5.16. In the mass spectrum for XUV-ionization (black curve), the signal from the acetylene mother ion is at least an order of magnitude greater than the residual gas, for instance water. The most abundant fragments are those in Group 1 (yellow) with the lowest dissociation limits in Fig. 5.15(c): C_2H^+, C_2+ and H^+. The Group 2-fragments (blue) CH_2^+, C^+ and CH^+ are also clearly seen. The peak from H_2^+ is very weak, matching the fact that it is the highest two-fragment dissociation limit. There are a number of peaks originating in acetone, $(CH_3)_2CO$, which is present to stabilize acetylene in the gas bottle. This accounts for several background gas fragments especially the

[2] Measurements with harmonics from argon at 1.2×10^{-2} mbar were also made.

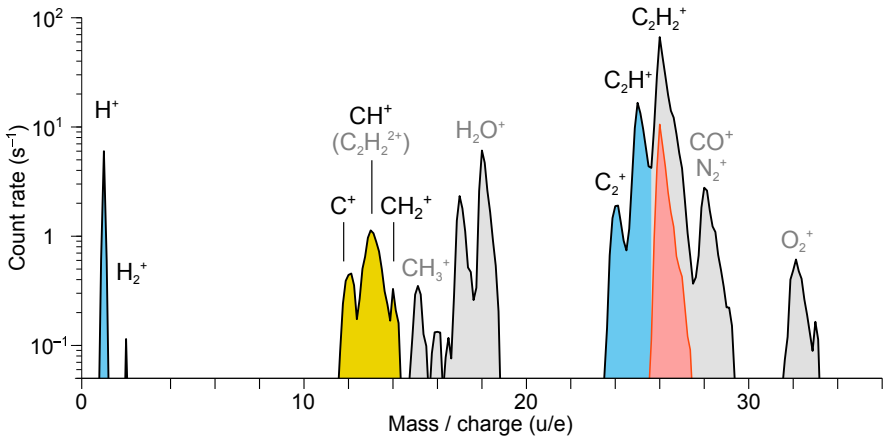

Figure 5.16: **Mass spectra with the XUV or IR pulses**. Ionization by the XUV pulse produces all of the expected acetylene fragments (black curve and text). The cyan or yellow coloured areas refer to the grouping of dissociation channels in Fig. 5.15. Ions labelled in grey text are from the background gas, including the CH_3^+ fragment from acetone. The infrared probe pulse with a moderate intensity can multi-photon ionize acetylene (red filled peak) but not dissociate it.

CH_3^+ peak. This does not affect our analysis of acetylene since previous studies show that fragmentation of acetone and acetylene after ionization at 23 eV produces no common fragments in the mass spectra [203]. Since the acetone mother ion is an order of magnitude weaker than acetylene and neither acetone nor its CH_3^+-fragment show dependence on the probe delay, the acetone contribution is ignored.

The intensity of the probing IR laser pulse is set at the threshold where multi-photon ionization occurs, where the intensity is expected to be a few times 10^{12} W/cm^2. To ionize acetylene, eight infrared photons must be absorbed. Fig. 5.16 shows a mass spectrum in red where the only acetylene peak is from the mother ion indicating that no dissociation is induced after IR multi-photon ionization.

The width of peaks in the mass spectrum is the combined effect of axial momentum and the extended source volume where the XUV beam intersects the effusive jet. It should however be noted that the logarithmic scale exaggerates the visible width. The best momentum resolution is obtained for the H^+ fragment, which will be analysed in terms of kinetic energy later. The first stage of the analysis concerns the intensities of the peaks, which will be analysed as functions of pump–probe delay.

Effects of the probe pulse

The intensity of the IR probe is too low to ionize the cation; only probe-induced transitions to potential energy surfaces within the cation need to be considered. While the probe intensity is sufficient to ionize neutral acetylene, multi-photon transition rates with many photons would be vanishingly small when the initial sample is reduced

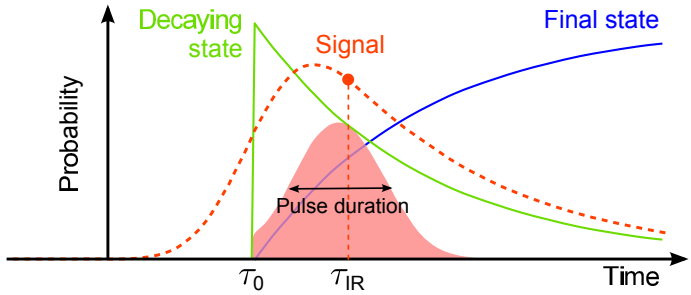

Figure 5.17: **Model for the signal in a pump–probe experiment**. It is assumed that the population in a particular state (green curve) appears rapidly at time τ_0 and decays exponentially to the blue final state. The time offset, τ_0, is zero if the green state is prepared directly by the pump pulse, but positive if nuclear motion is required to reach it. The probe pulse induces a transition from the decaying state to a different state which constitutes the observed signal (dotted red). For a particular probe delay, τ_{IR}, the signal is proportional to the shaded area, which is the product (convolution) of pulse envelope and population.

to those molecules already ionized by the XUV. From the X state, which has the highest initial population upon ionization [215], the four-photon transition required to reach A is forbidden by parity selection. Absorption of a fifth photon would lead to a vibrational level far from the Franck–Condon region and consequently also be unlikely. The first allowed transition is $X \rightarrow B$ (six-photon absorption). It is expected to be much weaker than transitions from the A, B and C states, requiring only one or two photons. In conclusion, the X state population can be ignored and laser induced dynamics and dissociation can be restricted to cationic states above 16 eV and a few probe photons.

The signal of each ionic fragment in the mass spectrum is analysed as function of the scanned delay between pump and probe pulse, τ_{IR}. Figure 5.17 shows the characteristic evolution that can be expected [45, 111]. If a short-lived transient state is probed, its population (green curve) should decrease exponentially with the probe delay:

$$E(\tau_{IR}) = \begin{cases} h \exp(-(\tau_{IR} - \tau_0)k) & \text{if} \quad \tau_{IR} > \tau_0 \\ 0 & \text{if} \quad \tau_{IR} < \tau_0 \end{cases}, \tag{5.6}$$

where h is the height of the step function (XUV-prepared population) at time offset τ_0 and k is the decay rate. The lifetime of the transient state is $1/k$. The final state of the decay (blue curve) could alternatively be probed [46]. The time offset, or isomerization time, τ_0 is positive if an interval of nuclear motion is required after ionization to reach the decaying state [69]. For signals coming from non-transient states, or having lifetimes much longer than the scan range, the fitted decay rate will be $k \approx 0$.

To fit the experimental signal, the combined (XUV and IR) pulse duration should be accounted for. The signal (dashed red in Fig. 5.17) is obtained as the convolution

[111] between equation (5.6) (green curve) and a Gaussian of 32 fs full-width at half max (FWHM). While molecular dynamics dressed by the infrared field could be required to explain a signal localized at $|\tau_{\mathrm{IR}}| < 32$ fs, signals outside this range can be explained with separate steps for the XUV and IR interaction and are therefore of primary interest. A variation in the signal at negative or positive τ_{IR} delay means that the IR-pulse induces dynamics in the neutral or probes dynamics in the ionic molecule, respectively.

The zero of the time scale for τ_{IR} is calibrated to give $\tau_0 = 0$ for a high-energy shoulder in the kinetic energy spectrum of H^+ ions, presented later (Fig. 5.19). This was typically within 10 fs from the XUV–IR overlap determined by electron interferometry (RABBIT) on argon before the acetylene scan.

Dynamics for the three first dissociation limits

Figure 5.18 shows the delay-dependence for the acetylene cation and the fragments resulting from dissociation to the three lowest limits (Group 1 in Fig. 5.15). The acetylene cation signal is reduced, as a negative step function, when the IR is sent later than the XUV. The lower part of the figure shows positive steps in all fragment yields. The cause of this must be that the XUV pump populates some states in $C_2H_2^+$ that do not normally dissociate but can be promoted to dissociative states by the probe. 46 % of the reduction in $C_2H_2^+$ yield is accounted for by dissociation to C_2H^+, which has the lowest appearance energy. Including the positive step heights for the other fragments shown, C_2^+ and H^+, means that 99 % of the acetylene signal's negative step is accounted for – a near perfect agreement. The delay-dependence of each fragment was analysed with the model described above. All of them are found to have decay life times $(1/k)$ greater than a picosecond, meaning practically no decay within the scan range. The H^+ fragment behaviour is slightly more complex: the analysis shows that the dynamics of the proton depend on the kinetic energy. This will be discussed in the next section. All steps occur at the same time (τ_0 within 2 fs), except C_2H^+ which is delayed by 18 ± 7 fs.

The absence of decay within the scan range for fitted step functions means that long-lived states are populated by the XUV pump. As motivated in the previous section, probing of the X state is unlikely and only the excited states will be considered here. According to the calculation in Ref. [211], the population of the $A\ ^2\Sigma_g^+$ state, as well as the $B\ ^2\Sigma_u^+$ state [201], in linear geometry are completely depleted after 250 fs. The population of A is transferred by proton-migration to vinylidene or by a conical intersection to the X-state in bent geometries ($1\ ^2\mathrm{A}'$ and $1\ ^2\mathrm{A}''$). Efficient internal vibrational energy redistribution (IVR) to the C–C stretching mode cools down the isomerization coordinate(s) [211]. In the case of the B-state [201], the fraction of the population transferred to A will undergo further relaxation while the fraction reaching the X-state should be stable. The total internal energy (electronic, vibrational and rotational) should be preserved since molecules in the gas phase can not dissipate heat to the surroundings. The final states reached are thus "hot" and likely to dissociate to the lowest dissociation limits, $C_2H^+ + H$, $C_2^+ + H_2$, and $H^+ + C_2H$, after absorption of one or two probe photons, also after long probe delays. This explains

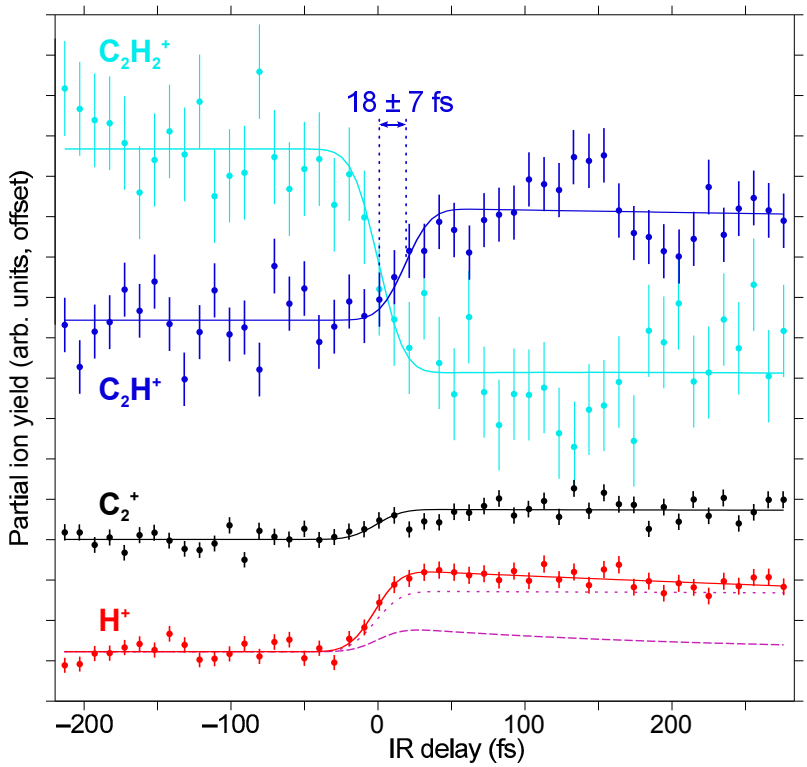

Figure 5.18: **Pump–probe study of $C_2H_2^+$: the three lowest dissociation limits**. The change in partial ion yield is shown as function of the delay, τIR, between the XUV pump and the IR probe, for acetylene and the ionic fragments for the dissociation limits in Group 1 (Fig. 5.15). To highlight the delay-dependence, signals are offset vertically by an arbitrary amount and ordered by mass. When the IR pulse is sent later than the XUV, the acetylene yield decreases by an amount that is perfectly compensated by the increases in the shown fragments. The step functions for all of these fragments were found to not decay within the scan range (fitted lifetime beyond a picosecond). Within the H^+ fragment yield at the bottom, two fitted components are shown filtered by kinetic energy. The low-energy component (dotted) has no decay but a femtosecond lifetime is found for the high-energy component (dashed).

the observed step functions in the yield of these fragments.

The height of the step in the C_2^+ yield is only about a third of the other steps in Fig. 5.18. A sequential dissociation via $H + C_2H^+$ into $H + C_2^+ + H$, where an additional bond is broken, would require almost 23 eV [214] and could not be accessed by the absorption of a single IR photon. The C_2^+ fragment is in general most likely to be created together with H_2 (appearance energy 18.4 eV [204, 214]) from the vinylidene geometry or after substantial cis-bending. Assuming the hot states lie below 17 eV, a probe transition reaching the $C_2^+ + H_2$ limit requires at least two IR photons.

Finally, in the C_2H^+ and $C_2H_2^+$ yields one can observe modulations with a period of ∼130 fs, appearing as deviations from the step-function curves. With increased probe intensity the modulations are seen also in other fragments, in-phase and out-phase with respect to the mother ion. An oscillating signal can be interpreted as quantum beat between two vibrational states [216] or more general nuclear wave packet dynamics on a potential energy surface. A longer scan range would be necessary for a Fourier analysis or assessment of coherence time. With the scan range limited to +280 fs, a tentative interpretation can be given from other considerations: Due to the initial excitation of many vibrational modes, the presence of fast internal energy redistribution and the complex topology of the potential-energy surfaces of the cationic states, it is more likely that the experiment probes nuclear dynamics.

One could speculate that it originates from the time for the proton to travel back and forth between the acetylene and vinylidene isomers. The period for this motion is expected to be 60 ± 10 fs [46, 212, 217] which seems in line with our observation. Other processes ought to be considered to explain the delayed onset for C_2H^+ of 18 ± 7 fs, such as the travelling time for the wave packet in the *A*-state [217] or the *B*-state [201] to reach the *X*-state through a conical intersection.

Ultra-fast deprotonation

The H^+ signal exhibits, both slow (>1 ps) and fast dynamics. The origin of this behaviour will be investigated here. Figure 5.19(a) compares the kinetic energy distribution of H^+, when the probe is sent well before/after the XUV pulse (dotted) or nearly overlapping (solid lines). Data from the present scan (magenta) is also compared with the scan having a higher probe intensity (green). While the spectra are essentially identical below 2 eV, an increased fraction of high-energy protons is seen at the overlap. With increased IR intensity, the high-energy signal is increased. We interpret the fact that the change occurs for energies above 2 eV and is intensity-dependent as indicative of a two-photon transition to a dissociating state.

The high-energy component of the H^+ yield exhibits a rather short transient-state lifetime, 212 ± 34 fs as shown in Fig. 5.19(b). (173 ± 26 fs in the scan with a stronger IR probe.) Assuming that the $H^+ + C_2H$ have no internal energy, a kinetic energy release of 3 eV means that the dissociative state would lie at about 22 eV. This is reachable by a two-photon transition from the Franck–Condon region in *B*. The reported lifetime of 14 fs for *B* [201] is however not consistent with our observation.

The appearance of a 3 eV-proton feature has been reported for ionization by electron impact and found to originate from the *C*-state at 23.5 eV, via predissociation

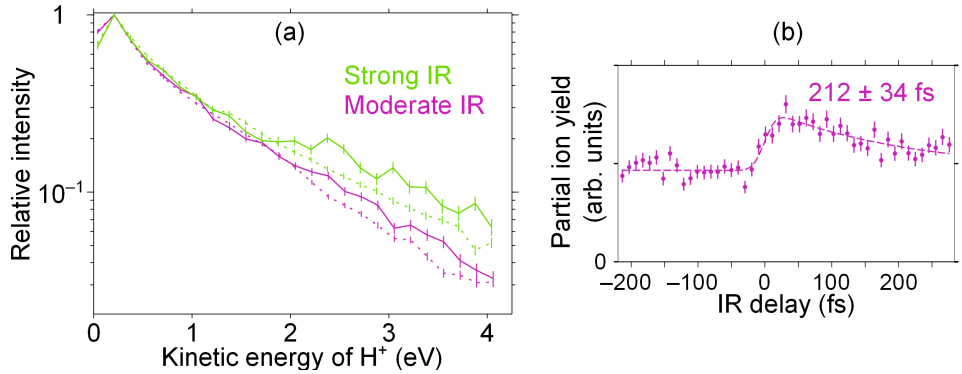

Figure 5.19: **Energy-resolved protons**. (a) Kinetic energy of the H^+ fragment from C_2H_2. The solid curves are obtained by integrating the range where the IR pulse is overlapping or at a small delay from the XUV ($0 \lesssim \tau_{IR} < 100$ fs). The dotted curves are integrated outside this range, and show a kinetic energy spectrum concentrated below 1 eV. At overlap the signal above 2 eV is significantly increased, more so if the IR intensity is increased (green, high harmonics generated in Ar) beyond the moderate intensity used in the main scan (magenta, Kr). (b) Delay-dependence and fitted lifetime for the H^+ signal above 2 eV.

to H^+ with C_2H in its first *excited* state ($^2\Pi$) at 19.6 eV [213]. A two-photon transition from the state at 21 eV to *C*, with subsequent dissociation, could explain the observation and provide an estimate of the lifetime for this state. The narrow vibrational peaks around 21 eV in Fig. 5.15(a) are consistent with lifetimes longer than in *B*. Although the 21 eV state is weakly populated by 40 eV photons it has been used in [217] and found responsible for the first appearance energy of the CH^+ fragment [202]. For the high-energy component to be small when the IR pulse is absent or sent earlier, the transient state should without IR absorption mainly evolve towards other fragments than H^+. The CH^+ limit at 20.8 eV would yield a very small kinetic energy release and could be compatible a substantial lifetime in the 21 eV state.

The low-energy H^+ component would in the XUV-only signal (at negative IR delay) most likely originate from the Franck–Condon region in *B*, while the non-depleted step was explained in the previous section to as probing from hot *A* and *X* states in bent geometries.

Dynamics for dissociations breaking the C–C bond

Figure 5.20 shows the pump–probe delay dependence of the remaining fragments, belonging to Group 2 in Fig. 5.15(c) where the C–C bond is broken. The fitted step functions all have onsets at the same time ($|\tau_0| < 7$ fs).

The $C + CH_2^+$ and $C^+ + CH_2$ dissociation channels have both protons on the same fragment and must be related to the vinylidene isomer. These channels are found to have the largest transient-state lifetimes, above 400 fs and equal within the

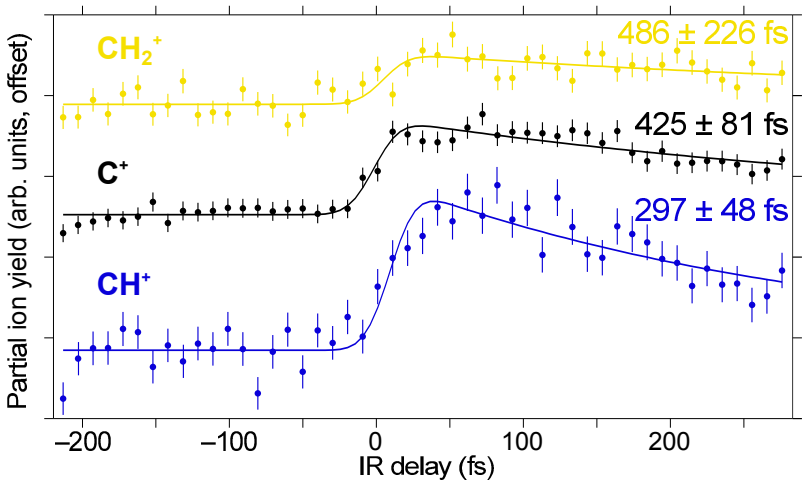

Figure 5.20: **Pump–probe study of $C_2H_2^+$: the C–C breaking dissociations**. The change in partial ion yield is shown for ionic fragments where a transient state lifetime shorter than a picosecond is found (printed on the right side). The unit for changes in the partial ion yield is the same as in Fig. 5.18 and Fig. 5.19(b) (0.1 % of the total ion yield).

fit uncertainty. The weighted average is 432 ± 76 fs. This time scale is on the order of the IVR driven process identified by Madjet [211] for the return of the acetylene cation from vinylidene conformations to a linear geometry in less than 500 fs.

The CH^+ yield, which is accessible by C–C bond breaking from the linear geometry, has the highest dissociation limit, the largest IR-induced step and the shortest transient-state lifetime, 297 ± 48 fs among the analysed fragments. Only the high-energy proton component had a somewhat shorter lifetime.

Summary

The origins of the C–C bond breaking channels have not been established yet. Nevertheless, transient state dynamics could be identified for the C–H breaking dissociation channels of acetylene. Several tentative assignments of mechanisms were given, and combining the high-resolution photoelectron spectrum of Ref. [199] with the literature and our data it appears we can affirm the experimental relevance of the elusive ∼21 eV state and obtain new information about its lifetime. Hints of IR intensity dependence have been mentioned but were not the focus in this presentation.

After these measurements were made, the spectrometer was upgraded with a molecular beam to minimize the source volume. This was demonstrated to greatly improve the mass and momentum resolution in Paper **VI**, to the level where it might be possible to study kinetic-energy dependence and angular distribution for other fragments than H^+.

5.3 Outlooks

The experiments presented in this thesis have been able to gain access to electronic and molecular dynamics, using different combinations of advanced light sources and charged-particle spectrometry. It is interesting to note that the light sources have complementary characteristics: a spectral width of 10 eV for the attosecond pulses and less than 0.1 eV for the synchrotron radiation.

So far, photoelectron group delays have been studied by attosecond pump–probe methods and by the angular distribution, for different systems. Since the current understanding of direct double ionization rests on the study of the two-electron angular distribution from helium (triply differential cross section) [16, 132] a combination of attosecond methods and electron momentum imaging in 3D is a very exciting outlook, combining both themes of this thesis. Although some 3D momentum experiments were made for electrons (in single ionization) during my doctoral studies the 3D-results presented here have focused on ions.

- To detect multiple electron momentum vectors in coincidence is becoming possible with the latest hardware, while the longer flight times of ions have allowed coincident studies of them for decades.
- To doubly ionize helium requires a high photon energy, which is possible to reach by high harmonics but seldom with kilohertz repetition rate.
- The particle-counting nature of coincidence experiments means that repetition rate is more of a concern than the average photon flux. The development of laser systems that can generate attosecond pulses with multi-kilohertz, or even megahertz, repetition rate is progressing at the moment, with coincidence applications as a driving force.

Sequential two-photon double ionization was assessed in section 5.1.1 mainly to avoid it and focus on regions where direct double ionization was probed in the continuum (nonsequential). The distinction between sequential and nonsequential ionization has been a long-standing topic with intense light sources, where both photons may be absorbed from the same pulse, from bound-electron lasers [27, 130, 218] to free-electron lasers [219]. In the present work, one photon came from an attosecond pulse train (in the XUV range) and the other from a femtosecond pulse. It has been predicted that the distinction between sequential and nonsequential processes breaks down if both photons come from attosecond pulses [220]. Very few XUV+XUV experiments have been made with attosecond pulses [71, 221] and studies of the correlated electrons in such cases remain to be made.

With broadband light sources, the possibly coherent evolution of states in a wide energy range (a wave packet) is important to consider and explore. Coherence between the two free electrons in autoionization of a cation (indirect double ionization) might be possible to examine by electron interferometry at femtosecond probe-delays, for instance in a molecule where nuclear motion “chirps” the energy levels over time. Coherence in the wave packet describing nuclear motion can be seen as oscillation in pump–probe signals (section 5.2.2). Decoherence is a major limitation for quantum computers and it appears that coherence properties are better utilized

for efficiency in some steps of biological photosynthesis than in artificial solar cells [222, 223]. Combined studies making the best of the complementary light sources and comparing semiclassical and quantum mechanical models can hopefully advance the understanding of some coherence phenomena.

In conclusion, the coincident detection of multiple particles enables studies of fundamental processes in systems of increasing complexity: polyatomic molecules and nanometre-sized clusters of atoms or molecules. Coincidence experiments recording momenta, or at least kinetic energy, for both electrons and ions will be important to aid the analysis of molecular dynamics by identifying both between which states the ionizing transition(s) occur and how the nuclei move [40, 41, 196, 202]. Momentum vectors were mostly analysed for the positive ions in this work but the capability of electron 3D-momentum in coincidence with ion mass is demonstrated in Paper **VI**. While attosecond pulses are good for studying the ionization process, their bandwidth would make a photoelectron spectrum from molecules with more than two atoms difficult to interpret. The analysis of a very dense atomic spectrum was performed in section 5.1.1 but for the time scale of nuclear dynamics, the narrower spectrum from one harmonic in the XVU range may be advantageous [224–226].

Acknowledgements

Thank you ...

Mathieu Gisselbrecht for infinite amounts of support, confidence in me and, probably, wisdom. Though your actions were puzzling at times it turned out there was usually a pedagogical intent. If you haven't succeeded in teaching me everything about the scientific life, it is not for lack of trying.

Stacey Ristinmaa Sorensen for steady guidance and seemingly keeping track of everything that was ever published. It was always reassuring to learn that you were watching the perimeters, through engagements in the scientific community and by finding resources for the group.

Anne L'Huillier for building a great team and for not giving up. Your and Marcus Dahlström's teaching gave me the first glimpses of attosecond physics, a feeling excellently conveyed in Marcus' thesis prologue [68]. Without our discussions I would perhaps never have understood Feynman diagrams. Thanks also to Johan Mauritsson for support during my master's project and for promoting science to the public.

Diego Guénot, Cord Arnold and David Kroon for long nights and early mornings in the attolab, and for general helpfulness. Without you there would have been no potato, zombie movie or science.

Joakim Laksman, Shabnam Oghbaie, Anna Sankari, Noelle Walsh, Bart Oostenrijk and Christian Stråhlman for all the beamtimes together with me. And perhaps even more for the beamtimes where I could not contribute, while writing the thesis.

Franck Lépine, Anatoli Kheifets and Eva Lindroth for contributing with expertise at the forefronts of large molecules and heavy atoms, experimentally or theoretically.

MAX-lab/MAX IV staff, particularly Maxim Tchaplyguine for advice and equipment during beamtimes and Rami Sankari for a critical review of the thesis, even spending time to find better references.

Patrik Wirgin, Anneli Nilsson-Ahlm, Achim Schnadt and Stacey for smooth running of the Division of Synchrotron Radiation Research.

Natalia Martin, Elin Grånäs, Olesia Snezhkova and Olof Persson for being the best office mates, and Natalia for being one step ahead with the thesis [227].

The numerous doctoral and master's students from distant places, including Sweden north of Skåne, for ensuring there was always something to discuss over lunch.

Martin Hjort [228], Erik Mårsell and Elin for developing word puns into a form of art – literally (by photography) as well as figuratively (verbally).

Finally, a big thanks to my parents and brothers – Anne, Tony, Robert and Anton – for a pleasant upbringing.

Bibliography

[1] H. Hertz. Ueber einen einfluss des ultravioletten lichtes auf die electrische entladung. *Annalen der Physik* **267**, 983–1000 (1887).

[2] A. Einstein. Über einen die Erzeugung und Verwandlung des Lichtes betreffenden heuristischen Gesichtspunkt. *Annalen der Physik* **17**, 132–148 (1905). Translated by D. ter Haar: On a Heuristic Point of View about the Creation and Conversion of Light. In *The Old Quantum Theory*, 91–107 (Pergamon Press, 1967).

[3] H. P. Bonzel & C. Kleint. On the history of photoemission. *Progress in Surface Science* **49**, 107–153 (1995).

[4] M. Drescher & F. Krausz. Attosecond physics: facing the wave–particle duality. *J. Phys. B: At., Mol. Opt. Phys.* **38**, S727 (2005).

[5] P. Auger. Sur l'effet photoélectrique composé. *J. Phys. Radium* **6**, 205–208 (1925).

[6] L. O. Werme, T. Bergmark & K. Siegbahn. The high resolution $L_{2,3}MM$ and $M_{4,5}NN$ auger spectra from krypton and $M_{4,5}NN$ and $N_{4,5}OO$ Auger spectra from xenon. *Physica Scripta* **6**, 141 (1972).

[7] C. Miron & P. Morin. High-resolution inner-shell photoionization, photoelectron and coincidence spectroscopy. In M. Quack & F. Merkt (eds.) *Handbook of High-resolution Spectroscopy* (John Wiley & Sons, Ltd, 2011).

[8] U. Becker. Photoelectron spectroscopy of atoms. *J. Electron Spectrosc. Relat. Phenom.* **75**, 23 – 34 (1995).

[9] T. Schneider, P. L. Chocian & J.-M. Rost. Separation and identification of dominant mechanisms in double photoionization. *Phys. Rev. Lett.* **89**, 073002 (2002).

[10] M. Drescher *et al.* Time-resolved atomic inner-shell spectroscopy. *Nature* **419**, 803–807 (2002).

[11] U. Hergenhahn. Interatomic and intermolecular coulombic decay: The early years. *J. Electron Spectrosc. Relat. Phenom.* **184**, 78–90 (2011).

[12] J. Schnadt *et al.* Experimental evidence for sub-3-fs charge transfer from an aromatic adsorbate to a semiconductor. *Nature* **418**, 620–623 (2002).

[13] A. Föhlisch *et al.* Direct observation of electron dynamics in the attosecond domain. *Nature* **436**, 373–376 (2005).

[14] J. H. D. Eland *et al.* Complete two-electron spectra in double photoionization: The rare gases Ar, Kr, and Xe. *Phys. Rev. Lett.* **90**, 053003 (2003).

[15] O. Guyétand *et al.* Complete momentum analysis of multi-photon photo-double ionization of xenon by XUV and infrared photons. *J. Phys. B: At., Mol. Opt. Phys.* **41**, 065601 (2008).

[16] L. Avaldi & A. Huetz. Photodouble ionization and the dynamics of electron pairs in the continuum. *J. Phys. B: At., Mol. Opt. Phys.* **38**, S861–S891 (2005).

[17] O. Björneholm *et al.* Femtosecond dissociation of core-excited hcl monitored by frequency detuning. *Phys. Rev. Lett.* **79**, 3150–3153 (1997).

[18] I. Hjelte *et al.* Evidence for ultra-fast dissociation of molecular water from resonant Auger spectroscopy. *Chemical Physics Letters* **334**, 151–158 (2001).

[19] M. Ferray *et al.* Multiple-harmonic conversion of 1064 nm radiation in rare gases. *J. Phys. B: At., Mol. Opt. Phys.* **21**, L31 (1988).

[20] P. B. Corkum. Plasma perspective on strong field multiphoton ionization. *Phys. Rev. Lett.* **71**, 1994–1997 (1993).

[21] P. M. Paul *et al.* Observation of a train of attosecond pulses from high harmonic generation. *Science* **292**, 1689–1692 (2001).

[22] L. Gallmann, C. Cirelli & U. Keller. Attosecond science: Recent highlights and future trends. *Annual Review of Physical Chemistry* **63**, 447–469 (2012).

[23] F. Krausz & M. Ivanov. Attosecond physics. *Rev. Mod. Phys.* **81**, 163–234 (2009).

[24] F. Lépine, G. Sansone & M. J. Vrakking. Molecular applications of attosecond laser pulses. *Chemical Physics Letters* **578**, 1–14 (2013).

[25] S. R. Leone *et al.* What will it take to observe processes in 'real time'? *Nature Photonics* **8**, 162–166 (2014).

[26] T. Weber *et al.* Correlated electron emission in multiphoton double ionization. *Nature* **405**, 658–661 (2000).

[27] B. Bergues *et al.* Attosecond tracing of correlated electron-emission in non-sequential double ionization. *Nature Communications* **3**, 813 (2012).

[28] N. Berrah *et al.* Non-linear processes in the interaction of atoms and molecules with intense EUV and x-ray fields from SASE free electron lasers (FELs). *Journal of Modern Optics* **57**, 1015–1040 (2010).

[29] A. Rouzée *et al.* Towards imaging of ultrafast molecular dynamics using FELs. *J. Phys. B: At., Mol. Opt. Phys.* **46**, 164029 (2013).

[30] M. Schultze *et al.* Delay in photoemission. *Science* **328**, 1658 (2010).

[31] K. Klünder *et al.* Probing single-photon ionization on the attosecond time scale. *Phys. Rev. Lett.* **106**, 143002 (2011).

[32] D. Guénot *et al.* Photoemission-time-delay measurements and calculations close to the 3*s*-ionization-cross-section minimum in Ar. *Phys. Rev. A* **85**, 053424 (2012).

[33] V. Schmidt. *Electron Spectrometry of Atoms using Synchrotron Radiation* (Cambridge University Press, 1997).

[34] C. J. Foot. *Atomic Physics* (Oxford University Press, 2005).

[35] P. Atkins & J. de Paula. *Atkins' Physical Chemistry* (Oxford University Press, 2010), ninth edn.

[36] A. Kikas *et al.* High-resolution study of the correlation satellites in photoelectron spectra of the rare gases. *J. Electron Spectrosc. Relat. Phenom.* **77**, 241–266 (1996).

[37] V. Schmidt. Photoionization of atoms using synchrotron radiation. *Rep. Prog. Phys.* **55**, 1483–1659 (1992).

[38] U. Fano. Effects of configuration interaction on intensities and phase shifts. *Phys. Rev.* **124**, 1866–1878 (1961).

[39] P. Lablanquie *et al.* Post collision interaction probed by multi-electron coincidences: Application to the Ar 2s inner-shell photoionization. *J. Electron Spectrosc. Relat. Phenom.* **185**, 198–203 (2012).

[40] J. Ullrich *et al.* Recoil-ion and electron momentum spectroscopy: reaction-microscopes. *Reports on Progress in Physics* **66**, 1463 (2003).

[41] M. Yamazaki *et al.* 3D mapping of photoemission from a single oriented H_2O molecule. *J. Phys. B: At., Mol. Opt. Phys.* **42**, 051001 (2009).

[42] S. K. Semenov *et al.* Auger decay of $1\sigma_g$ and $1\sigma_u$ hole states of the N_2 molecule: Disentangling decay routes from coincidence measurements. *Phys. Rev. A* **81**, 043426 (2010).

[43] M. Hochlaf, F. R. Bennett, G. Chambaud & P. Rosmus. Theoretical study of the electronic states of CO_2. *J. Phys. B: At., Mol. Opt. Phys.* **31**, 2163 (1998).

[44] L. S. Cederbaum. The exact molecular wavefunction as a product of an electronic and a nuclear wavefunction. *J. Chem. Phys.* **138**, 224110 (2013).

[45] J. van Tilborg *et al.* Femtosecond isomerization dynamics in the ethylene cation measured in an EUV-pump NIR-probe configuration. *J. Phys. B: At., Mol. Opt. Phys.* **42**, 081002 (2009).

[46] Y. H. Jiang *et al.* Ultrafast extreme ultraviolet induced isomerization of acetylene cations. *Phys. Rev. Lett.* **105**, 263002 (2010).

[47] J. Muga & C. Leavens. Arrival time in quantum mechanics. *Physics Report* **338**, 353–438 (2000).

[48] J. Hilgevoord. Time in quantum mechanics. *American Journal of Physics* **70**, 301–306 (2002).

[49] J. Hilgevoord. Time in quantum mechanics: a story of confusion. *Studies in History and Philosophy of Modern Physics* **36**, 29–60 (2005).

[50] B. E. A. Saleh & M. C. Teich. *Fundamentals of Photonics* (John Wiley & Sons, Inc., Hoboken, New Jersey, 2007), second edn.

[51] R. N. Zare. Photoejection dynamics. *Mol. Photochem.* **4**, 1–37 (1972). `http://www.stanford.edu/group/Zarelab/publinks/zarepub60.pdf`.

[52] S.-c. Yang & R. Bersohn. Theory of the angular distribution of molecular photofragments. *J. Chem. Phys.* **61**, 4400–4407 (1974).

[53] G. Wu, P. Hockett & A. Stolow. Time-resolved photoelectron spectroscopy: from wavepackets to observables. *Phys. Chem. Chem. Phys.* **13**, 18447–18467 (2011).

[54] C. N. Yang. On the angular distribution in nuclear reactions and coincidence measurements. *Phys. Rev.* **74**, 764–772 (1948).

[55] L. H. Haber, B. Doughty & S. R. Leone. Continuum phase shifts and partial cross sections for photoionization from excited states of atomic helium measured by high-order harmonic optical pump-probe velocity map imaging. *Phys. Rev. A* **79**, 031401 (2009).

[56] S. Fritzsche, A. N. Grum-Grzhimailo, E. V. Gryzlova & N. M. Kabachnik. Sequential two-photon double ionization of the 4d shell in xenon. *J. Phys. B: At., Mol. Opt. Phys.* **44**, 175602 (2011).

[57] G. Herzberg. *Molecular Spectra and Molecular Structure: Vol. I – Spectra of diatomic molecules* (Krieger Publishing Company, Malabar, Florida, 1950 & 1989), 2nd edn.

[58] W. C. Stolte *et al.* 100% site-selective fragmentation in core-hole-photoexcited methanol by anion-yield spectroscopy. *J. Phys. B: At., Mol. Opt. Phys.* **35**, L253 (2002).

[59] Z. D. Pešić, D. Rolles, R. C. Bilodeau, I. Dimitriu & N. Berrah. Three-body fragmentation of CO_2^{2+} upon K-shell photoionization. *Phys. Rev. A* **78**, 051401 (2008).

[60] J. Laksman. *Nuclear motion in molecular ions studied with synchrotron radiation and multicoincidence momentum imaging spectrometry.* Ph.D. thesis, Lund University (2012).

[61] J. Cooper & R. N. Zare. Erratum: Angular distribution of photoelectrons. *J. Chem. Phys.* **49**, 4252–4252 (1968).

[62] M. G. White *et al.* Angular distribution of Xe 5s $\rightarrow$ ϵp photoelectrons near the cooper minimum. *Phys. Rev. Lett.* **43**, 1661–1664 (1979).

[63] J. Dahlström *et al.* Theory of attosecond delays in laser-assisted photoionization. *Chemical Physics* **414**, 53–64 (2013).

[64] J. M. Dahlström, A. L'Huillier & A. Maquet. Introduction to attosecond delays in photoionization. *J. Phys. B: At., Mol. Opt. Phys.* **45**, 183001 (2012).

[65] J. J. Sakurai. *Modern Quantum Mechanics* (Addison Wesley Longman, 1993), revised edition edn.

[66] E. P. Wigner. Lower limit for the energy derivative of the scattering phase shift. *Phys. Rev.* **98**, 145–147 (1955).

[67] C. Hoffmann. Representing difference: Ernst Mach and Peter Salcher's ballistic-photographic experiments. *Endeavour* **33**, 18–23 (2009).

[68] J. M. Dahlström. *Light-matter interaction on the attosecond timescale*. Ph.D. thesis, Lund University, LRAP-438 (2011).

[69] M. Dantus, M. J. Rosker & A. H. Zewail. Femtosecond real-time probing of reactions. II. the dissociation reaction of ICN. *J. Chem. Phys.* **89**, 6128 (1988).

[70] A. H. Zewail. Femtochemistry: Atomic-scale dynamics of the chemical bond. *J. Phys. Chem. A* **104**, 5660–5694 (2000).

[71] P. Tzallas, E. Skantzakis, L. A. A. Nikolopoulos, G. D. Tsakiris & D. Charalambidis. Extreme-ultraviolet pump–probe studies of one-femtosecond-scale electron dynamics. *Nature Physics* **7**, 781–784 (2011).

[72] K. Varjú *et al.* Angularly resolved electron wave packet interferences. *J. Phys. B: At., Mol. Opt. Phys.* **39**, 3983 (2006).

[73] T. Remetter *et al.* Attosecond electron wave packet interferometry. *Nature Physics* **2**, 323–326 (2006).

[74] H. G. Muller. Reconstruction of attosecond harmonic beating by interference of two-photon transitions. *Applied Physics B* **74**, s17–s21 (2002).

[75] R. López-Martens *et al.* Amplitude and phase control of attosecond light pulses. *Phys. Rev. Lett.* **94**, 033001 (2005).

[76] A. A. Michelson & E. Morley. On the relative motion of the earth and the luminiferous ether. *American Journal of Science* **34**, 333–345 (1887). `http://www.aip.org/history/gap/PDF/michelson.pdf`.

[77] J. Mauritsson *et al.* Attosecond electron spectroscopy using a novel interferometric pump-probe technique. *Phys. Rev. Lett.* **105**, 053001 (2010).

[78] K. Klünder. *Electron Wave Packet Dynamics on the Attosecond Time Scale*. Ph.D. thesis, Lund University, LRAP-457 (2012).

[79] MAX IV Laboratory. Max-lab web site. `https://www.maxlab.lu.se/`. Retrieved 2014-Jan-03.

[80] M. Sjöström, E. Wallén, M. Eriksson & L.-J. Lindgren. The MAX III storage ring. *Nucl. Instr. Meth. Phys. Res., Sect. A* **601**, 229–244 (2009).

[81] C. Stråhlman *et al.* Angle-resolved time-of-flight spectroscopy applied to multi-bunch operation at max-lab: a design study. *Journal of Physics: Conference Series* **425**, 092011 (2013).

[82] S. Werin. *Accelerator technique* (MAX-lab, Lund, 2006), 2.5th edn.

[83] D. Brandt (ed.). *CERN Accelerator School: Course on Synchrotron Radiation and Free-Electron Lasers* (2003). DOI: 10.5170/CERN-2005-012.

[84] Lightsources.org. *History.* `http://www.lightsources.org/cms/?pid=1001274`. Retrieved 2013-Jan-11.

[85] D. I. Svergun & M. H. J. Koch. Small-angle scattering studies of biological macromolecules in solution. *Reports on Progress in Physics* **66**, 1735–1782 (2003).

[86] R. Wehlitz. Ch. 1: Simultaneous emission of multiple electrons from atoms and molecules using synchrotron radiation. In E. A. Paul Berman & C. Lin (eds.) *Advances In Atomic, Molecular, and Optical Physics*, vol. 58, 1–76 (Academic Press, 2010).

[87] Å. Andersson, M. Eriksson, L.-J. L. andP. Röjsel & S. Werin. The new 1.5 GeV storage ring for synchrotron radiation: MAX II. *Rev. Sci. Instrum.* **66**, 1850–1853 (1995).

[88] M. Bässler *et al.* Beam line I411 at MAX-II – performance and first results. *Nucl. Instr. Meth. Phys. Res., Sect. A* **469**, 382–393 (2001).

[89] E. S. Reich. Ultimate upgrade for US synchrotron. *Nature News* **501**, 148–149 (2013).

[90] M. Swoboda. *Attosecond Wave Packet Metrology.* Ph.D. thesis, Lund University, LRAP-414 (2010).

[91] P. Mulller. Glossary of terms used in physical organic chemistry: Iupac recommendations 1994. *Pure and Applied Chemistry* **66**, 1077–1184 (1994).

[92] S. G. Lias & J. E. Bartmess. *Gas-phase ion thermochemistry.* `http://webbook.nist.gov/chemistry/ion/`. Retrieved 2014-Jan-25.

[93] E. Gustafsson *et al.* Broadband attosecond pulse shaping. *Opt. Lett.* **32**, 1353–1355 (2007).

[94] M. Chini, K. Zhao & Z. Chang. The generation, characterization and applications of broadband isolated attosecond pulses. *Nature Photonics* **8**, 178–186 (2014).

[95] E. P. Månsson. *Temporal gating of attosecond pulse trains.* Master's dissertation, Lund University, LRAP-403 (2009).

[96] C. Koen. Significance testing of periodogram ordinates. *Astrophysical Journal* **348**, 700–702 (1990).

[97] National Institute of Standards and Technology (NIST). Atomic spectra database, v. 5 (2013). `http://physics.nist.gov/asd`.

[98] E. Andersson *et al.* Multielectron coincidence study of the double Auger decay of 3d-ionized krypton. *Phys. Rev. A* **82**, 043418 (2010).

[99] Y. Hikosaka *et al.* Double photoionization into double core-hole states in Xe. *Phys. Rev. Lett.* **98**, 183002 (2007).

[100] K. P. Burnham & D. R. Anderson. *Model selection and multimodel inference: a practical information-theoretic approach* (Springer, New York, 2002), 2nd edn.

[101] L. J. Frasinski, K. Codling & P. A. Hatherly. Covariance mapping: A correlation method applied to multiphoton multiple ionization. *Science* **246**, 1029–1031 (1989). `http://www.jstor.org/stable/1704942`.

[102] R. Trainham & J. Tinsley. Covariance analysis of gamma ray spectra. *Rev. Sci. Instrum.* **84**, 013502 (2013).

[103] O. Kornilov *et al.* Coulomb explosion of diatomic molecules in intense xuv fields mapped by partial covariance. *J. Phys. B: At., Mol. Opt. Phys.* **46**, 164028 (2013).

[104] RoentDek Handels GmbH. Manuals (2010). `http://www.roentdek.de/manuals/`.

[105] Cronologic GmbH & Co. KG. High speed digitizers. `http://www.cronologic.de/products/digitizer/`. Retrieved 2014-Jan-28.

[106] V. Ulrich *et al.* Photoelectron–auger electron coincidence spectroscopy of free molecules: New experiments. *J. Electron Spectrosc. Relat. Phenom.* **183**, 70 – 79 (2011).

[107] G. Öhrwall *et al.* A new energy and angle resolving electron spectrometer – first results. *J. Electron Spectrosc. Relat. Phenom.* **183**, 125 – 131 (2011).

[108] P. Kruit & F. H. Read. Magnetic field paralleliser for 2π electron-spectrometer and electron-image magnifier. *J. Phys. E: Sci. Instrum.* **16**, 313–324 (1983).

[109] M. Mucke *et al.* Performance of a short "magnetic bottle" electron spectrometer. *Rev. Sci. Instrum.* **83**, 063106 (2012).

[110] K. Rademann, T. Rech, B. Kaiser, U. Even & F. Hensel. A new coincidence technique for vacuum ultraviolet photoelectron spectroscopy of neutral clusters in a molecular beam. *Rev. Sci. Instrum.* **62**, 1932–1941 (1991).

[111] J. Lacoursière, M. Meyer, L. Nahon, P. Morin & M. Larzillière. Time-resolved pump-probe photoelectron spectroscopy of helium using a mode-locked laser synchronized with synchrotron radiation pulses. *Nucl. Instr. Meth. Phys. Res., Sect. A* **351**, 545–553 (1994).

[112] The MathWorks, Inc. MATLAB documentation – "least-squares fitting", `lsqnonlin`, `fitoptions` and `nlparci` (2011). `http://www.mathworks.com/help/optim/ug/lsqnonlin.html`.

[113] W. C. Wiley & I. H. McLaren. Time-of-flight mass spectrometer with improved resolution. *Rev. Sci. Instrum.* **26**, 1150–1157 (1955).

[114] D. P. Seccombe & T. J. Reddish. Theoretical study of space focusing in linear time-of-flight mass spectrometers. *Rev. Sci. Instrum.* **72**, 1330–1338 (2001).

[115] A. Lindgren. *Studies of Molecular and Cluster Fragmentation Using Synchrotron Radiation: Measurements and Models*. Ph.D. thesis, Lund University (2006).

[116] J. Laksman, D. Céolin, E. P. Månsson, S. L. Sorensen & M. Gisselbrecht. Development and characterization of a multiple-coincidence ion-momentum imaging spectrometer. *Rev. Sci. Instrum.* **84**, 123113 (2013).

[117] M. Lebech, J. C. Houver & D. Dowek. Ion-electron velocity vector correlations in dissociative photoionization of simple molecules using electrostatic lenses. *Rev. Sci. Instrum.* **73**, 1866–1874 (2002).

[118] G. A. Garcia, L. Nahon, C. J. Harding, E. A. Mikajlo & I. Powis. A refocusing modified velocity map imaging electron/ion spectrometer adapted to synchrotron radiation studies. *Rev. Sci. Instrum.* **76**, 053302 (2005).

[119] A. Vredenborg, W. G. Roeterdink & M. H. M. Janssen. A photoelectron-photoion coincidence imaging apparatus for femtosecond time-resolved molecular dynamics with electron time-of-flight resolution of $\sigma = 18$ ps and energy resolution $\delta e/e = 3.5\%$. *Rev. Sci. Instrum.* **79**, 063108 (2008).

[120] R. Dörner *et al.* Cold target recoil ion momentum spectroscopy: a 'momentum microscope' to view atomic collision dynamics. *Physics Reports* **330**, 95–192 (2000).

[121] A. Adams & F. H. Read. Electrostatic cylinder lenses III: three element asymmetric voltage lenses. *J. Phys. E: Sci. Instrum.* **5**, 156 (1972).

[122] R. Campargue. Progress in overexpanded supersonic jets and skimmed molecular beams in free-jet zones of silence. *The Journal of Physical Chemistry* **88**, 4466–4474 (1984).

[123] A. T. J. B. Eppink & D. H. Parker. Velocity map imaging of ions and electrons using electrostatic lenses: Application in photoelectron and photofragment ion imaging of molecular oxygen. *Rev. Sci. Instrum.* **68**, 3477–3484 (1997).

[124] G. A. Garcia, H. Soldi-Lose & L. Nahon. A versatile electron-ion coincidence spectrometer for photoelectron momentum imaging and threshold spectroscopy on mass selected ions using synchrotron radiation. *Rev. Sci. Instrum.* **80**, 023102 (2009).

[125] M. J. J. Vrakking. An iterative procedure for the inversion of two-dimensional ion/photoelectron imaging experiments. *Rev. Sci. Instrum.* **72**, 4084–4089 (2001).

[126] G. A. Garcia, L. Nahon & I. Powis. Two-dimensional charged particle image inversion using a polar basis function expansion. *Rev. Sci. Instrum.* **75**, 4989–4996 (2004).

[127] R. Dörner *et al.* Double ionization by one and many photons. *Radiation Physics and Chemistry* **70**, 191–206 (2004).

[128] C. F. de Morisson Faria & X. Liu. Electron-electron correlation in strong laser fields. *J. Mod. Opt.* **58**, 1076–1131 (2011).

[129] G. Sansone, T. Pfeifer, K. Simeonidis & A. I. Kuleff. Electron correlation in real time. *ChemPhysChem* **13**, 661–680 (2012).

[130] A. N. Pfeiffer, C. Cirelli, M. Smolarski, R. Doerner & U. Keller. Timing the release in sequential double ionization. *Nature Physics* **7**, 428 (2011).

[131] A. N. Pfeiffer, C. Cirelli, M. Smolarski & U. Keller. Recent attoclock measurements of strong field ionization. *Chemical Physics* **414**, 84–91 (2013).

[132] J. S. Briggs & V. Schmidt. Differential cross sections for photo-double-ionization of the helium atom. *J. Phys. B: At., Mol. Opt. Phys.* **33**, R1 (2000).

[133] F. L. Yip, T. N. Rescigno, C. W. McCurdy & F. Martín. Fully differential single-photon double ionization of neon and argon. *Phys. Rev. Lett.* **110**, 173001 (2013).

[134] U. Becker & B. Langer. Correlation and coherence phenomena studied by photoelectron spectroscopy. *Nucl. Instr. Meth. Phys. Res., Sect. A* **601**, 78–87 (2009).

[135] I. Martinson & L. Curtis. Janne Rydberg – his life and work. *Nucl. Instr. Meth. Phys. Res., Sect. B* **235**, 17–22 (2005).

[136] R. D. Cowan. *The theory of atomic structure and spectra* (University of California Press, 1981).

[137] J. E. Hansen & W. Persson. Revised analysis of singly ionized xenon, Xe II. *Physica Scripta* **36**, 602 (1987).

[138] S. Alitalo *et al.* The valence photoelectron satellite spectra of Kr and Xe. *J. Electron Spectrosc. Relat. Phenom.* **114-116**, 141–146 (2001).

[139] H. Yoshii, T. Aoto, Y. Morioka & T. Hayaishi. Satellite structures of Kr and Xe studied by high-resolution threshold photoelectron spectroscopy. *J. Phys. B: At., Mol. Opt. Phys.* **40**, 2765 (2007).

[140] W. Persson *et al.* Spectrum of doubly ionized xenon (Xe III). *Physica Scripta* **38**, 347 (1988).

[141] J. Söderström *et al.* Angle-resolved electron spectroscopy of the resonant Auger decay in xenon with meV energy resolution. *New Journal of Physics* **13**, 073014 (2011).

[142] J. H. D. Eland. Dynamics of double photoionization in molecules and atoms. In S. A. Rice (ed.) *Advances in Chemical Physics*, vol. 141, 103–152 (John Wiley & Sons, Inc., 2009).

[143] J. Berkowitz, J. L. Dehmer, Y.-K. Kim & J. P. Desclaux. Valence shell excitation accompanying photoionization in mercury. *J. Chem. Phys.* **61**, 2556–2559 (1974).

[144] S. Svensson, B. Eriksson, N. Mårtensson, G. Wendin & U. Gelius. Electron shake-up and correlation satellites and continuum shake-off distributions in x-ray photoelectron spectra of the rare gas atoms. *J. Electron Spectrosc. Relat. Phenom.* **47**, 327–384 (1988).

[145] F. H. Read. A modified rydberg formula. *J. Phys. B: At., Mol. Phys.* **10**, 449 (1977).

[146] I. Martin *et al.* Quantum defect orbital study of electronic transitions in rydberg molecules: ammonium and fluoronium radicals. *Chemical Physics* **202**, 307–320 (1996).

[147] N. Zheng & T. Wang. Radiative lifetimes and atomic transition probabilities for atomic carbon and oxygen. *The Astrophysical Journal Supplement Series* **143**, 231 (2002).

[148] H. Kossmann, V. Schmidt & T. Andersen. Test of Wannier threshold laws: Double-photoionization cross section in helium. *Phys. Rev. Lett.* **60**, 1266–1269 (1988).

[149] J.-E. Rubensson *et al.* Influence of the radiative decay on the cross section for double excitations in helium. *Phys. Rev. Lett.* **83**, 947–950 (1999).

[150] J. Berkowitz. *Atomic and Molecular Photoabsorption: Absolute Total Cross Sections* (Academic Press, 2001). Pp. 95–96.

[151] J. Dubau & M. J. Seaton. Quantum defect theory. XIII. radiative transitions. *J. Phys. B: At., Mol. Opt. Phys.* **17**, 381 (1984).

[152] P. Bolognesi *et al.* A study of the doubly charged states of Xe and their satellites by threshold photoelectron-threshold photoelectron coincidence (TPEsCO) spectroscopy. *J. Phys. B: At., Mol. Opt. Phys.* **33**, 4723–4734 (2000).

[153] O. Smirnova, V. S. Yakovlev & A. Scrinzi. Quantum coherence in the time-resolved auger measurement. *Phys. Rev. Lett.* **91**, 253001 (2003).

[154] A. S. Kheifets. Time delay in valence-shell photoionization of noble-gas atoms. *Phys. Rev. A* **87**, 063404 (2013).

[155] C. Neidel *et al.* Probing time-dependent molecular dipoles on the attosecond time scale. *Phys. Rev. Lett.* **111**, 033001 (2013).

[156] C. Ott *et al.* Lorentz meets Fano in spectral line shapes: A universal phase and its laser control. *Science* **340**, 716–720 (2013).

[157] R. Ma *et al.* Photoelectron angular distributions for the two-photon ionization of helium by ultrashort extreme ultraviolet free-electron laser pulses. *J. Phys. B: At., Mol. Opt. Phys.* **46**, 164018 (2013).

[158] R. D. Mattuck. *A guide to Feynman diagrams in the many-body problem* (McGraw-Hill, Inc., New York, 1976), second edn.

[159] H. W. Kroto, A. W. Allaf & S. P. Balm. C60: Buckminsterfullerene. *Chemical Reviews* **91**, 1213–1235 (1991).

[160] S. W. Bishnoi *et al.* All-optical nanoscale pH meter. *Nano Letters* **6**, 1687–1692 (2006).

[161] A. M. Schwartzberg & J. Z. Zhang. Novel optical properties and emerging applications of metal nanostructures. *The Journal of Physical Chemistry C* **112**, 10323–10337 (2008).

[162] E. Ozbay. Plasmonics: Merging photonics and electronics at nanoscale dimensions. *Science* **311**, 189–193 (2006).

[163] S. A. Maier *et al.* Plasmonics—a route to nanoscale optical devices. *Advanced Materials* **13**, 1501–1505 (2001).

[164] B. v. Issendorff & O. Cheshnovsky. Metal to insulator transitions in clusters. *Annu. Rev. Phys. Chem.* **56**, 549–580 (2005).

[165] E. Mårsell *et al.* Secondary electron imaging of nanostructures using extreme ultra-violet attosecond pulse trains and infra-red femtosecond pulses. *Annalen der Physik* **525**, 162–170 (2013).

[166] A. D. J. Haymet. Footballene: a theoretical prediction for the stable, truncated icosahedral molecule C_{60}. *J. Am. Chem. Soc.* **108**, 319–321 (1986).

[167] M. E. Madjet, H. S. Chakraborty, J. M. Rost & S. T. Manson. Photoionization of C_{60}: a model study. *J. Phys. B: At., Mol. Opt. Phys.* **41**, 105101 (2008).

[168] E. Maurat, P.-A. Hervieux & F. Lépine. Surface plasmon resonance in C_{60} revealed by photoelectron imaging spectroscopy. *J. Phys. B: At., Mol. Opt. Phys.* **42**, 165105 (2009).

[169] A. V. Verkhovtsev, A. V. Korol & A. V. Solov'yov. Plasmon excitations in photo- and electron impact ionization of fullerenes. *Journal of Physics: Conference Series* **438**, 012011 (2013).

[170] W. Ekardt. Size-dependent photoabsorption and photoemission of small metal particles. *Phys. Rev. B* **31**, 6360–6370 (1985).

[171] G. F. Bertsch, A. Bulgac, D. Tománek & Y. Wang. Collective plasmon excitations in C_{60} clusters. *Phys. Rev. Lett.* **67**, 2690–2693 (1991).

[172] C. N. Banwell & E. M. McCash. *Fundamentals of molecular spectroscopy* (McGraw-Hill, 1994), fourth edn.

[173] G. Kristensson. *Elektromagnetisk vågutbredning* [Electromagnetic wave propagation] (Studentlitteratur, Lund, 1999).

[174] J. Andersen & E. Bonderup. Local field corrections for light absorption by fullerenes. *Eur. Phys. J. D* **11**, 435–448 (2000).

[175] I. V. Hertel *et al.* Giant plasmon excitation in free C_{60} and C_{70} molecules studied by photoionization. *Phys. Rev. Lett.* **68**, 784–787 (1992).

[176] S. W. J. Scully *et al.* Photoexcitation of a volume plasmon in c_{60} ions. *Phys. Rev. Lett.* **94**, 065503 (2005).

[177] M. Shapiro & P. Brumer. Quantum control of bound and continuum state dynamics. *Physics Reports* **425**, 195–264 (2006).

[178] E. Wells *et al.* Adaptive strong-field control of chemical dynamics guided by three-dimensional momentum imaging. *Nature Communications* **4**, 2895 (2013).

[179] V. V. Lozovoy *et al.* Control of molecular fragmentation using shaped femtosecond pulses. *The Journal of Physical Chemistry A* **112**, 3789–3812 (2008).

[180] P. Ranitovic *et al.* Attosecond vacuum uv coherent control of molecular dynamics. *Proceedings of the National Academy of Sciences* **111**, 912–917 (2014).

[181] R. H. Dalitz. Decay of τ mesons of known charge. *Phys. Rev.* **94**, 1046–1051 (1954).

[182] K. Ueda & J. H. D. Eland. Molecular photodissociation studied by vuv and soft x-ray radiation. *J. Phys. B: At., Mol. Opt. Phys.* **38**, S839 (2005).

[183] M. Schulz, D. Fischer, T. Ferger, R. Moshammer & J. Ullrich. Four-particle Dalitz plots to visualize atomic break-up processes. *J. Phys. B: At., Mol. Opt. Phys.* **40**, 3091 (2007).

[184] K. C. Prince, L. Avaldi, M. Coreno, R. Camilloni & M. de Simone. Vibrational structure of core to Rydberg state excitations of carbon dioxide and dinitrogen oxide. *J. Phys. B: At., Mol. Opt. Phys.* **32**, 2551 (1999).

[185] G. Wight & C. Brion. K-shell energy loss spectra of 2.5 keV electrons in CO_2 and N_2O. *J. Electron Spectrosc. Relat. Phenom.* **3**, 191–205 (1974).

[186] A. D. McLean. LCAO-MO-SCF ground state calculations on C_2H_2 and CO_2. *J. Chem. Phys.* **32**, 1595–1597 (1960).

[187] K. Nobusada. A theoretical simulation of symmetry-resolved spectra for excitation to the C $1s^{-1}$ $2\pi_u$ Renner-Teller states in CO_2. *J. Phys. B: At., Mol. Opt. Phys.* **35**, 3055 (2002).

[188] R. Renner. Zur Theorie der Wechselwirkung zwischen Elektronen- und Kernbewegung bei dreiatomigen, stabförmigen Molekülen. *Zeitschrift für Physik* **92**, 172–193 (1934).

[189] J. Pople & H. Longuet-Higgins. Theory of the Renner effect in the NH_2 radical. *Molecular Physics* **1**, 372–383 (1958).

[190] H. A. Jahn & E. Teller. Stability of polyatomic molecules in degenerate electronic states. I. Orbital degeneracy. *Proc. R. Soc. London Ser. A* **161**, 220–235 (1937).

[191] E. Kukk, J. D. Bozek & N. Berrah. Photoexcitation and Auger decay of the Renner-Teller split C $1s^{-1}$ π_u^* state in CO_2. *Phys. Rev. A* **62**, 032708 (2000).

[192] N. Saito *et al.* Deformation, nuclear motion and fragmentation of core-excited CO_2 probed by multiple-ion coincidence momentum imaging. *J. Electron Spectrosc. Relat. Phenom.* **141**, 183–193 (2004).

[193] J. Laksman, D. Céolin, M. Gisselbrecht, S. E. Canton & S. L. Sorensen. Dynamics of proton migration and dissociation in core-excited ethyne probed by multiple ion momentum imaging. *J. Chem. Phys.* **131**, 244305 (2009).

[194] J. Laksman, D. Céolin, M. Gisselbrecht & S. L. Sorensen. Nuclear motion in carbonyl sulfide induced by resonant core electron excitation. *J. Chem. Phys.* **133**, 144314 (2010).

[195] M. Eroms, M. Jungen & H.-D. Meyer. Vibronic coupling effects in resonant Auger spectra of H_2O. *The Journal of Physical Chemistry A* **116**, 11140–11150 (2012).

[196] S. Zamith *et al.* The predissociation of highly excited states in acetylene by time-resolved photoelectron spectroscopy. *J. Chem. Phys.* **119**, 3763–3773 (2003).

[197] Y. Jiang *et al.* Watching the acetylene vinylidene intramolecular reaction in real time. *Preprint* (2014). `http://arxiv.org/abs/1402.4874`.

[198] L. Avaldi *et al.* Photoionization of acetylene near the threshold. *J. Electron Spectrosc. Relat. Phenom.* **71**, 93–105 (1995).

[199] S. Canton. 40 eV photoelectron spectrum of C_2H_2. Private communication (2014).

[200] M. Carlsson Göthe *et al.* Vibrationally resolved study of the fourth photoelectron band of acetylene at 23.5 eV. *Chemical Physics Letters* **174**, 109–112 (1990).

[201] J. E. Reutt *et al.* Photoelectron spectroscopy and inferred femtosecond intramolecular dynamics of $C_2H_2^+$ and $C_2D_2^+$. *J. Chem. Phys.* **84**, 3022–3031 (1986).

[202] M. Davister & R. Locht. The dissociative ionization of C_2H_2 and C_2D_2. the $[CH(CD)]^+$ dissociation channel. the H(D)C≡C(D)H binding energy. *Chemical Physics* **191**, 333–346 (1995).

[203] C. Servais & R. Locht. The appearance energy of C_2H^+ from C_2H_2 revisited. A photoion–photoelectron coincidence spectroscopic determination. *Chemical Physics Letters* **236**, 96–102 (1995).

[204] R. Locht & M. Davister. The dissociative ionization of C_2H_2. The C^+, C_2^+ and CH_2^+ dissociation channels. The vinylidene ion as a transient? *Chemical Physics* **195**, 443–456 (1995).

[205] S. Boyé-Péronne, D. Gauyacq & J. Liévin. Vinylidene-acetylene cation isomerization investigated by large scale ab initio calculations. *J. Chem. Phys.* **124**, 214305 (2006).

[206] G. Chambaud, R. V. den Boom & P. Rosmus. On the mechanism of the energy redistribution in the $\tilde{A}\ ^2A_g(^2\Sigma_g^+)$ state of the $HCCH^+$ ion. *Chem. Phys. Lett.* **247**, 79–84 (1995).

[207] P. Rosmus, P. Botchwina & J. Maier. On the ionic states of vinylidene and acetylene. *Chemical Physics Letters* **84**, 71–76 (1981).

[208] S.-K. Shih, S. D. Peyerimhoff & R. J. Buenker. Calculated potential surfaces for the description of the emission spectrum of the C_2H radical. *Journal of Molecular Spectroscopy* **74**, 124–135 (1979).

[209] W. Koch & G. Frenking. The low-lying electronic states of protonated C_2, CCH^+. *J. Chem. Phys.* **93**, 8021–8028 (1990).

[210] R. C. Gillen, B. Ostojic & W. Domcke. Theoretical investigation of $\tilde{A}\ ^2\Sigma_g^+$–$\tilde{X}\ ^2\Pi_u$ vibronic-coupling and ultrafast internal-conversion dynamics in the acetylene cation. *Chemical Physics* **272**, 1–14 (2001).

[211] M. E.-A. Madjet, O. Vendrell & R. Santra. Ultrafast dynamics of photoionized acetylene. *Phys. Rev. Lett.* **107**, 263002 (2011).

[212] M. E.-A. Madjet, Z. Li & O. Vendrell. Ultrafast hydrogen migration in acetylene cation driven by non-adiabatic effects. *J. Chem. Phys.* **138**, 094311 (2013).

[213] M. Davister & R. Locht. The dissociative electroionization of C_2H_2, C_2D_2 and C_2HD: Investigation of the $[C_2H(D)]^+$ and $[H(D)]^+$ dissociation channels.the (D)H–C_2:H(D) binding energy. *Chemical Physics* **189**, 805–824 (1994).

[214] R. Mackie *et al.* A photoionization mass spectrometric study of acetylene and ethylene in the VUV spectral region. *Int. J. Mass Spectrom.* **223–224**, 67–79 (2003).

[215] D. Holland, M. MacDonald, M. Hayes, L. Karlsson & B. Wannberg. A photoelectron spectroscopy study of the valence shell photoionization dynamics of acetylene. *J. Electron Spectrosc. Relat. Phenom.* **104**, 245–255 (1999).

[216] S. Banerjee & G. Gangopadhyay. Quantum beat in the pump–probe signal of a molecular system. *J. Phys. B: At., Mol. Opt. Phys.* **36**, 2967 (2003).

[217] H. Ibrahim *et al.* Tabletop imaging of structural evolutions in chemical reactions. *Preprint* (2014). `http://arxiv.org/abs/1402.1419`.

[218] B. Walker *et al.* Precision measurement of strong field double ionization of helium. *Phys. Rev. Lett.* **73**, 1227–1230 (1994).

[219] M. Kurka *et al.* Two-photon double ionization of Ne by free-electron laser radiation: a kinematically complete experiment. *J. Phys. B: At., Mol. Opt. Phys.* **42**, 141002 (2009).

[220] J. Feist *et al.* Electron correlation in two-photon double ionization of helium from attosecond to XFEL pulses. *J. Phys. B: At., Mol. Opt. Phys.* **42**, 134014 (2009).

[221] E. J. Takahashi, P. Lan, O. D. Mücke, Y. Nabekawa & K. Midorikawa. Attosecond nonlinear optics using gigawatt-scale isolated attosecond pulses. *Nature Communications* **4**, 2691 (2013).

[222] J. M. Anna, G. D. Scholes & R. van Grondelle. A little coherence in photosynthetic light harvesting. *BioScience* **64**, 14–25 (2014).

[223] R. E. Blankenship *et al.* Comparing photosynthetic and photovoltaic efficiencies and recognizing the potential for improvement. *Science* **332**, 805–809 (2011).

[224] I. Thomann *et al.* Temporal characterization of attosecond wave forms in the sub-optical-cycle regime. *Phys. Rev. A* **78**, 011806 (2008).

[225] W. Cao *et al.* Dynamic modification of the fragmentation of autoionizing states of O_2^+. *Phys. Rev. A* **84**, 053406 (2011).

[226] X. Zhou *et al.* Probing and controlling non-Born–Oppenheimer dynamics in highly excited molecular ions. *Nature Physics* **8**, 232–237 (2012).

[227] N. M. Martin. *Surface Studies of Model Systems relevant for Pd and Ag Catalysts.* Ph.D. thesis, Lund University (2014).

[228] M. Hjort. *III–V Nanowire Surfaces.* Ph.D. thesis, Lund University (2014).